Sede Amministrativa: Università degli Studi di Padova
Dipartimento di Fisica e Astronomia "G. Galilei"

Corso di Dottorato di Ricerca in Astronomia
Ciclo XXX

New models of pulsating red giant stars: application to Long-Period Variables in the Large Magellanic Cloud

Coordinatore: Ch.mo Prof. Giampaolo Piotto
Supervisore: Prof.ssa Paola Marigo
Co-Supervisore: Dr.ssa Josefina Montalbán
Co-Supervisore: Dr. Léo Girardi

Dottorando: Michele Trabucchi

Abstract

Stars of low and intermediate mass ($0.9 \lesssim M/\mathrm{M}_{\odot} \lesssim 8$) develop an electron-degenerate CO core after the core He-burning phase, and experience the thermally pulsing asymptotic giant branch phase (TP-AGB) as they approach the end of their evolution.

Although very short lived, TP-AGB stars are of paramount importance in the study of stellar populations and galaxy evolution. In fact, being intrinsically very bright, they provide a significant contribution to the total luminosity of single stellar populations, and galaxies in general. Most of their radiation is emitted at infrared wavelengths, a spectral range where extinction by dust is small. They are thus very useful as tracers of intermediate age stars, and are often used to characterise stellar populations in external galaxies.

The characteristic spectral signatures of TP-AGB stars have been observed even at high redshift, and they are in general visible even at large distances. Additionally, variable TP-AGB stars follow a well defined period-luminosity relation in the near infrared, which makes them a promising distance indicator.

TP-AGB stars play a prominent role in the chemical enrichment of galaxies. Repeated third dredge-up events are efficient in bringing nucleosynthesis products (He, C, N, *s*-process elements) to the stellar surface, which low temperature favours the formation of molecular species. Stellar pulsations induce shock waves that compress the atmosphere and allow for the condensation of dust grains. Being highly opaque, dust is pushed outwards in the interstellar medium by radiation pressure, dragging the enriched gas with itself.

The chain of events just described represents a clear example of the various physical processes, poorly understood and heavily entangled, involved in TP-AGB evolution.

As a result, in spite of its crucial role across astrophysics, the TP-AGB is one of the least understood phases of stellar evolution. Its modelling is affected by large uncertainties that propagate in the field of extragalactic astronomy, degrading the predicting power of current population synthesis models of galaxies.

The present PhD thesis is the result of three years of work within the ERC project STARKEY, which major goal is exactly to provide a physically-sound calibration of the TP-AGB phase as a function of age and metallicity.

This is pursued by requiring models to simultaneously reproduce different observables of resolved TP-AGB stellar populations in star clusters and nearby galaxies. The project adopts an all-round theoretical approach that takes into account several, strongly interconnected, key physical processes (convective mixing, stellar winds, dust formation, and stellar pulsation).

These calibrated models are used to generate new well-tested grids of stellar tracks, isochrones, chemical yelds of gas and dust, stellar spectra, pulsation models, all made available to the scientific community.

The specific subject of the present work is the study of stellar pulsations on the TP-AGB, and was performed by computing a large grid of new pulsation models.

Updated models of luminous red giant variables have long been missing from the scientific literature, and a set of models systematically accounting for the variety of properties of TP-AGB stars has never been published.

A critical shortcoming of previous models, with the relevant exception of a few selected studies, is that they do not account for surface chemical enrichment. Carbon stars, produced by the dredge-up of carbon, have characteristic spectral features that are dramatically different than those of their O-rich counterpart. This is a consequence of altered molecular equilibria, and the corresponding drastic change in the main sources of molecular opacity.

Atmospheric opacities determine stellar radii, thus affecting the pulsation period. It is therefore clear that they need to be consistent with the detailed chemical mixture predicted by evolutionary models. Part of this work was devoted to the inclusion of updated opacities in the modelling of pulsation, a significant improvement with respect to past studies, which generally employed opacity data computed for standard scaled-solar mixtures.

As already mentioned, pulsation on the TP-AGB is essential to the enrichment of the interstellar medium. More generally, it is crucial for mass-loss, dust formation, and ultimately evolution. But of course, pulsating red giant stars are important for a number of other reasons.

The most luminous ones, the large-amplitude Mira variables, have long been known to follow a period-luminosity (PL) relation that is very clear in the near-infrared bands, and represents a very promising distance indicator (see, *e.g.*, Whitelock, 2013; Huang et al., 2018), especially in view of the forthcoming missions such as JWST.

The discovery, during the last two decades, of multiple PL relations in the long-period variables (LPVs) of the Large Magellanic Cloud (Wood et al., 1999) re-ignited the interest for such stars. The different PL relations, or sequences, are assumed to be due to different pulsation modes, which are characterised by distinct period and excitation properties depending on the stellar properties and evolutionary stages.

Therefore, observed periods provide an additional constraint, together with other observables, to be matched by theoretical models, allowing us to refine our knowledge of stellar structure and evolution. Observed periods represent also a powerful tool to estimate global parameters such as stellar masses and radii.

However, to fully exploit the potential of LPVs, a knowledge of the exact pulsation modes corresponding to each sequence is required. This aim has been pursued by numerous studies in the past decades, with the unfortunate result that two interpretations emerged, both based on valid arguments, but providing mode assignments in contrast with each other.

Again, this disagreement is largely due to the use of pulsation models unable to represent the variety of the AGB population of the Magellanic Clouds.

In the present work, we present a new, large grid of linear, radial, non-adiabatic pulsation models, with updated opacity data for CNO-varied metal mixtures.

The grid covers a wide range of the space of stellar parameters characterising the TP-AGB phase, in terms of total mass, core mass, luminosity, effective temperature, and chemical composition. Models include periods and amplitude growth rates for five radial pulsation modes, from the fundamental to the fourth overtone.

Growth rates allow us to predict to a reasonably good accuracy the excitation/stability

degree of individual modes, and provide information on their expected observability.

The structure of the grid in terms of its defining parameters is based on detailed TP-AGB evolutionary tracks, but the computation of pulsation models is decoupled from evolutionary models. This way, pulsation models are compatible with virtually any output from evolutionary and population synthesis codes, and are going to be made publicly available, filling a long-existing gap.

The grid of pulsation models has been implemented in the STARKEY framework to be tested against observations. Our approach involves the simulation of the pulsation properties of a synthetic population of luminous red giant stars.

Such a simulation was computed to reproduce the observed photometric and variability properties of AGB stars in the Large Magellanic Cloud (Trabucchi et al., 2017).

The results have shown a good degree of agreement between models and observations, and allowed us to provide a new interpretation of the observed PL sequences, essentially solving the past tensions and bringing the previous interpretations into alignment.

Our result provides additional information about the open topic of long secondary periods in red giant variables. Moreover, it supports the idea of a connection between faint LPVs and solar-like oscillations in less evolved red giants (see, *e.g.*, Mosser et al., 2013, and references therein), the implications of which would open new frontiers in the study of stellar oscillations.

The comparison with observations confirmed that the new models are able to predict pulsation periods of all observed modes with good accuracy. Remarkably, theoretical growth rates are able to account for the observed distribution of overtone modes amplitudes, in spite of the uncertainties in the treatment of the interaction between convection and pulsation.

On the other hand, growth rates of the fundamental mode are still affected by large uncertainties, as they are not able to reproduce the observed instability strip.

Further studies are required to address in more detail the excitation of pulsation in luminous red giants, with special attention for the fundamental mode.

Additional future developments include the use of non-linear models to: (1) constrain models by reproducing observed variability amplitudes, (2) investigate the conditions under which linear models are not appropriate to describe pulsation periods, and (3) provide, for those cases, suitable period corrections as a function of global stellar parameters.

Contents

Chapter 1

Introduction

Stars of low and intermediate mass ($0.9 \lesssim M/\mathrm{M}_{\odot} \lesssim 8$) develop an electron-degenerate CO core after the core He-burning phase, and experience the thermally pulsing asymptotic giant branch phase (TP-AGB) as they approach the end of their evolution.

Although very short lived, TP-AGB stars are of paramount importance in the study of stellar populations and galaxy evolution. In fact, being intrinsically very bright, they provide a significant contribution to the total luminosity of single stellar populations, and galaxies in general. Most of their radiation is emitted at infrared wavelengths, a spectral range where extinction by dust is small. They are thus very useful as tracers of intermediate age stars, and are often used to characterise stellar populations in external galaxies.

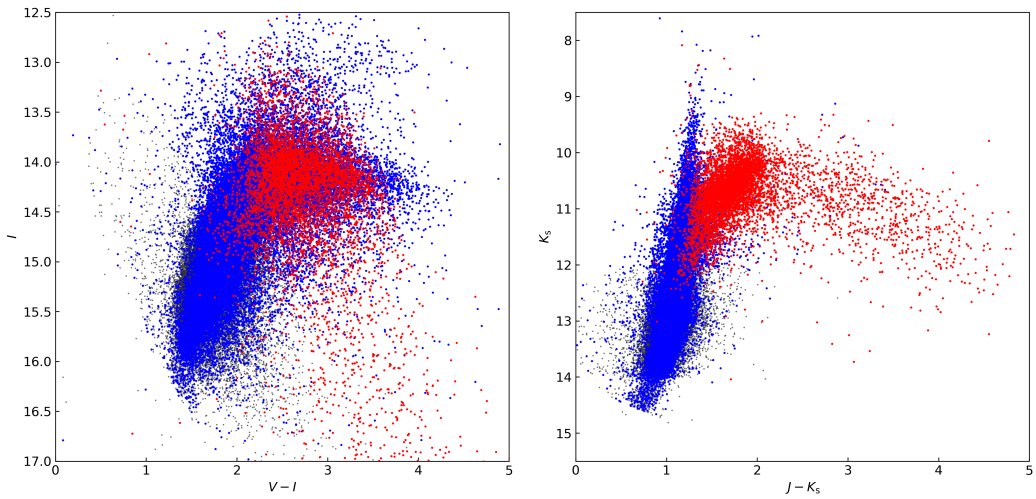

Figure 1.1: Color-magnitude diagrams of variable red giants in the LMC. Blue and red symbols represent O-rich and C-rich AGBs, respectively. Data are taken from the OGLE-III Collection of variables stars (Soszyński et al., 2009) and from the 2MASS Point Source Catalogue (Skrutskie et al., 2006).

The characteristic spectral signatures of TP-AGB stars have been observed even at high redshift, and they are in general visible even at large distances. Additionally, variable TP-AGB stars follow a well defined period-luminosity relation in the near infrared, which makes them a promising distance indicator.

TP-AGB stars play a prominent role in the chemical enrichment of galaxies. Re-

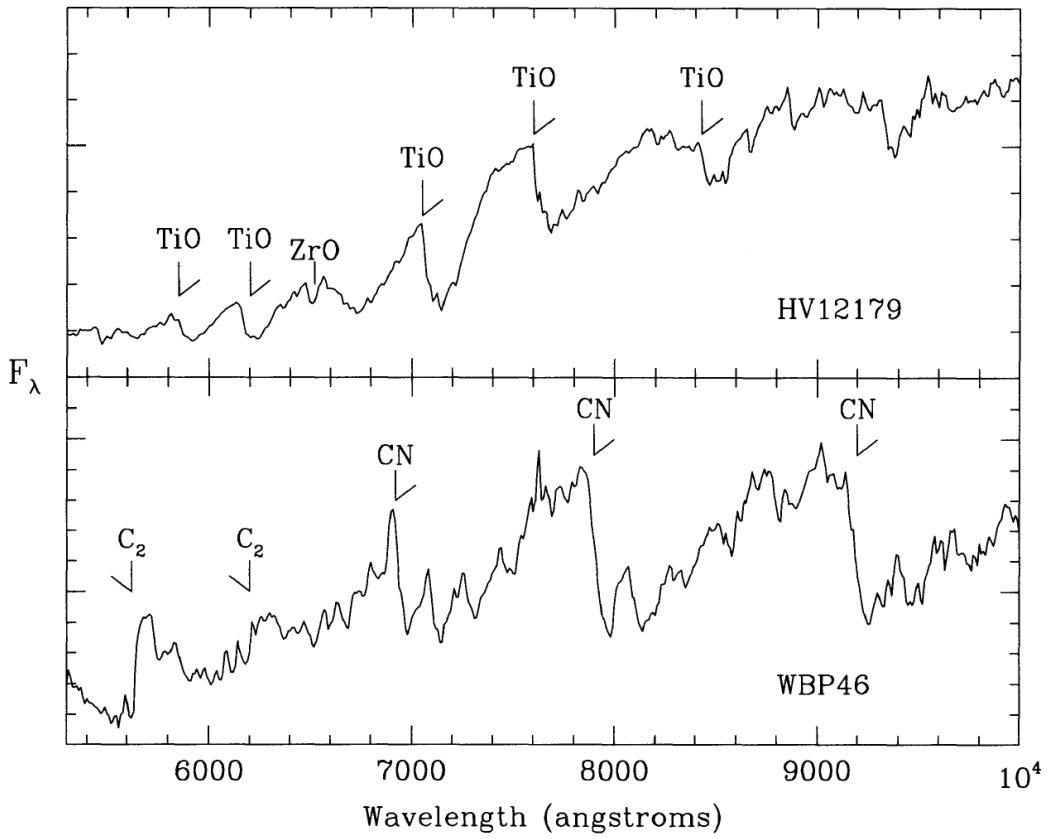

Figure 1.2: Example spectra of an MS-type star (top panel) and a C-star (bottom panel), with some of the strongest molecular bands identified. TiO molecules, and VO in cool stars, dominate the spectra of O-rich M- and MS-type stars. The spectra of C-rich stars are dominated by C_2 and CN molecules (reproduced from Habing and Olofsson (2004)).

peated third dredge-up events are efficient in bringing nucleosynthesis products (He, C, N, *s*-process elements) to the stellar surface, which low temperature favours the formation of molecular species. Stellar pulsations induce shock waves that compress the atmosphere and allow for the condensation of dust grains. Being highly opaque, dust is pushed outwards in the interstellar medium by radiation pressure, dragging the enriched gas with itself.

The chain of events just described represents a clear example of the various physical processes, poorly understood and heavily entangled, involved in TP-AGB evolution.

As a result, in spite of its crucial role across astrophysics, the TP-AGB is one of the least understood phases of stellar evolution. Its modelling is affected by large uncertainties that propagate in the field of extragalactic astronomy, degrading the predicting power of current population synthesis models of galaxies.

The present PhD thesis is the result of three years of work within the ERC project STARKEY, which major goal is exactly to provide a physically-sound calibration of the TP-AGB phase as a function of age and metallicity.

This is pursued by requiring models to simultaneously reproduce different observables of resolved TP-AGB stellar populations in star clusters and nearby galaxies. The project adopts an all-round theoretical approach that takes into account several,

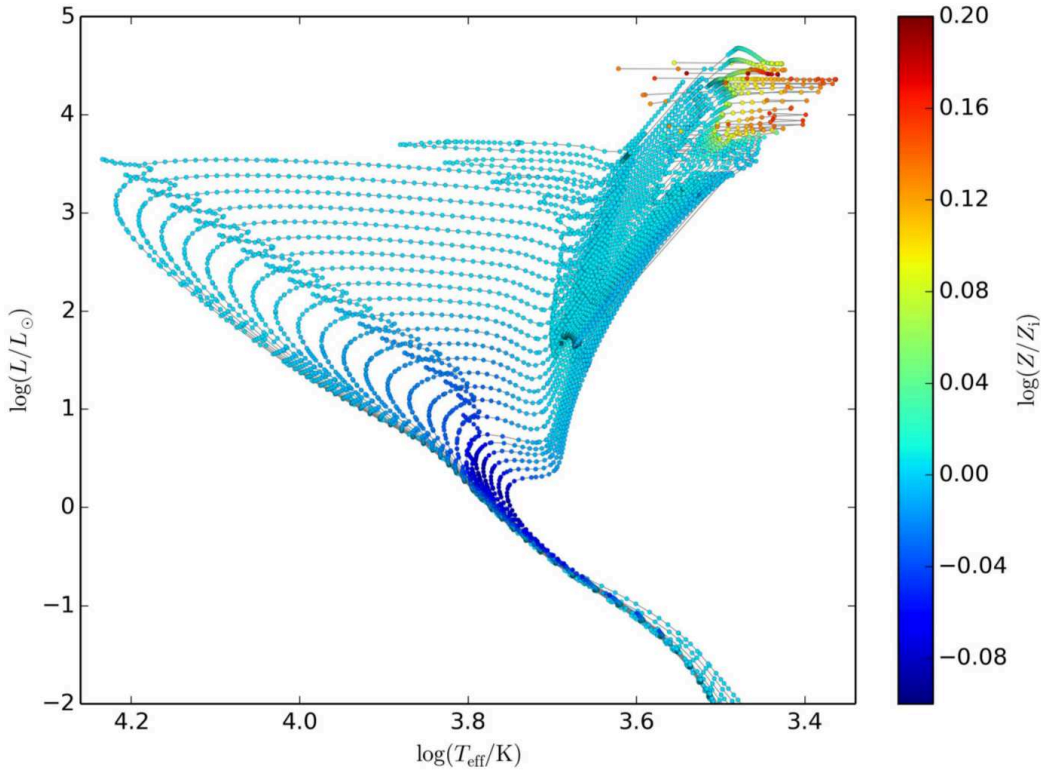

Figure 1.3: Example of calibrated isochrones produced in the framework of the STARKEY project. The initial metallicity is $Z_i \simeq 0.015$, ages vary from $\log(t/\mathrm{yr}) = 7.8$ to 10.1. Symbols are colour coded according to the ratio between current surface metallicity and the initial one, and clearly show the large changes undergone during the TP-AGB (at $\log(L/\mathrm{L}_\odot) \gtrsim 4$). (Reproduced from Marigo et al. (2017))

strongly interconnected, key physical processes (convective mixing, stellar winds, dust formation, and stellar pulsation).

These calibrated models are used to generate new well-tested grids of stellar tracks, isochrones, chemical yelds of gas and dust, stellar spectra, pulsation models, all made available to the scientific community.

The specific subject of the present work is the study of stellar pulsations on the TP-AGB, and was performed by computing a large grid of new pulsation models.

Updated models of luminous red giant variables have long been missing from the scientific literature, and a set of models systematically accounting for the variety of properties of TP-AGB stars has never been published.

A critical shortcoming of previous models, with the relevant exception of a few selected studies, is that they do not account for surface chemical enrichment. Carbon stars, produced by the dredge-up of carbon, have characteristic spectral features that are dramatically different than those of their O-rich counterpart. This is a consequence of altered molecular equilibria, and the corresponding drastic change in the main sources of molecular opacity.

Atmospheric opacities determine stellar radii, thus affecting the pulsation period. It is therefore clear that they need to be consistent with the detailed chemical mixture predicted by evolutionary models. Part of this work was devoted to the inclusion of updated opacities in the modelling of pulsation, a significant improvement with respect

to past studies, which generally employed opacity data computed for standard scaled-solar mixtures.

As already mentioned, pulsation on the TP-AGB is essential to the enrichment of the interstellar medium. More generally, it is crucial for mass-loss, dust formation, and ultimately evolution. But of course, pulsating red giant stars are important for a number of other reasons.

The most luminous ones, the large-amplitude Mira variables, have long been known to follow a period-luminosity (PL) relation that is very clear in the near-infrared bands, and represents a very promising distance indicator (see, *e.g.*, Whitelock, 2013; Huang et al., 2018), especially in view of the forthcoming missions such as JWST.

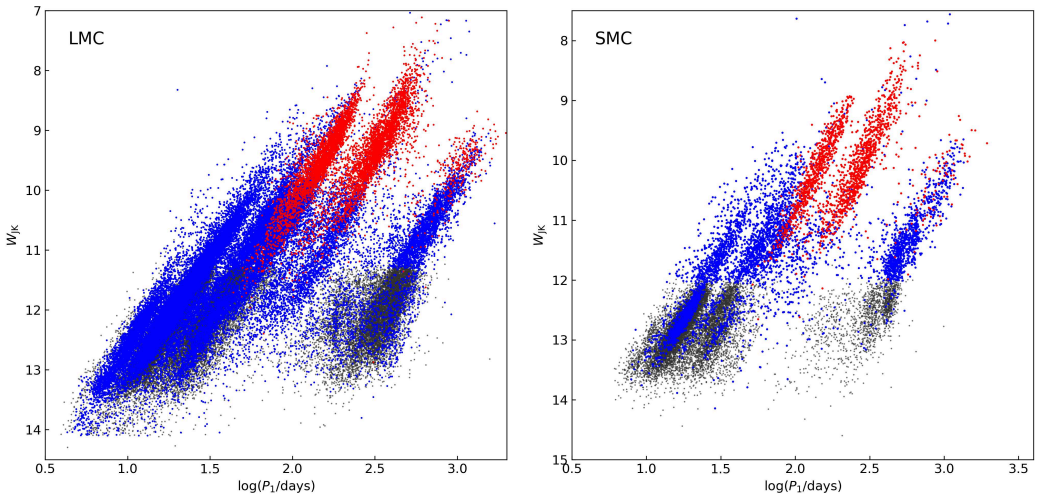

Figure 1.4: Period-luminosity diagrams of the LPVs in the Magellanic Clouds. Blue and red symbols represent O-rich and C-rich AGBs, respectively. Data are taken from the OGLE-III Collection of variables stars (Soszyński et al., 2009) and from the 2MASS Point Source Catalogue (Skrutskie et al., 2006).

The discovery, during the last two decades, of multiple PL relations in the long-period variables (LPVs) of the Large Magellanic Cloud (Wood et al., 1999) re-ignited the interest for such stars. The different PL relations, or sequences, are assumed to be due to different pulsation modes, which are characterised by distinct period and excitation properties depending on the stellar properties and evolutionary stages.

Therefore, observed periods provide an additional constraint, together with other observables, to be matched by theoretical models, allowing us to refine our knowledge of stellar structure and evolution. Observed periods represent also a powerful tool to estimate global parameters such as stellar masses and radii.

However, to fully exploit the potential of LPVs, a knowledge of the exact pulsation modes corresponding to each sequence is required. This aim has been pursued by numerous studies in the past decades, with the unfortunate result that two interpretations emerged, both based on valid arguments, but providing mode assignments in contrast with each other.

Again, this disagreement is largely due to the use of pulsation models unable to represent the variety of the AGB population of the Magellanic Clouds.

In the present work, we present a new, large grid of linear, radial, non-adiabatic pulsation models, with updated opacity data for CNO-varied metal mixtures.

The grid covers a wide range of the space of stellar parameters characterising the TP-AGB phase, in terms of total mass, core mass, luminosity, effective temperature, and chemical composition. Models include periods and amplitude growth rates for five radial pulsation modes, from the fundamental to the fourth overtone.

Growth rates allow to predict to a reasonably good accuracy the excitation/stability degree of individual modes, and provide information on their expected observability.

The structure of the grid in terms of its defining parameters is based on detailed TP-AGB evolutionary tracks, but the computation of pulsation models is decoupled from evolutionary models. This way, pulsation models are compatible with virtually any output from evolutionary and population synthesis codes, and are going to be made publicly available, filling a long-existing gap.

The grid of pulsation models has been implemented in the STARKEY framework to be tested against observations. Our approach involves the simulation of the pulsation properties of a synthetic population of luminous red giant stars.

Such a simulation was computed to reproduce the observed photometric and variability properties of AGB stars in the Large Magellanic Cloud (Trabucchi et al., 2017).

The results have shown a good degree of agreement between models and observations, and allowed to provide a new interpretation of the observed PL sequences, essentially solving the past tensions and bringing the previous interpretations into alignment.

Our result provides additional information about the open topic of long secondary periods in red giant variables. Moreover, it supports the idea of a connection between faint LPVs and solar-like oscillations in less evolved red giants (see, *e.g.*, Mosser et al., 2013, and references therein), the implications of which would open new frontiers in the study of stellar oscillations.

The comparison with observations confirmed that the new models are able to predict pulsation periods of all observed modes with good accuracy. Remarkably, theoretical growth rates are able to account for the observed distribution of overtone modes amplitudes, in spite of the uncertainties in the treatment of the interaction between convection and pulsation.

On the other hand, growth rates of the fundamental mode are still affected by large uncertainties, as they are not able to reproduce the observed instability strip.

Further studies are required to address in more detail the excitation of pulsation in luminous red giants, with special attention for the fundamental mode.

Additional future developments include the use of non-linear models to: (1) constrain models by reproducing observed variability amplitudes, (2) investigate the conditions under which linear models are not appropriate to describe pulsation periods, and (3) provide, for those cases, suitable period corrections as a function of global stellar parameters.

1.1 Outline of the Work

In Chapter 2, we introduce the general background of the present work. First, we summarise the main properties of TP-AGB stars, recalling stellar evolution of stars of low and intermediate mass before and during the asymptotic giant branch. The main physical processes related to the TP-AGB phase are briefly described. In the second part of Chapter 2, we summarise the properties of pulsating red giant stars, including their classification, with some attention on Mira variables and their PL relation. This connects with the following section, where the discovery of additional PL rela-

tions of LPVs is described from a somewhat chronological point of view. The current interpretation of the PL sequences of LPVs in the Magellanic Cloud is then discussed.

In Chapter 3, we provide the physical and mathematical background of the theory of stellar oscillations, focusing on radial, adiabatic and non-adiabatic pulsations.

Chapter 4 represents the core of this thesis. There, we describe the codes we used and the new tools we developed, as well as the procedure with which we combined them in order to produce a new grid of updated pulsation models. Then, we describe the grid and discuss how it was implemented with a population synthesis code to include variability data in the simulation of stellar populations.

An application of the grid to simulate populations of pulsating giants is presented in Chapter 5. We employed this method to reproduce the observed PL sequences of the LPVs in the Large Magellanic Cloud. We present the results of this study, and the new interpretation it brought to.

Finally, some conclusion remarks and future perspectives are presented in Chapter 6.

Chapter 2

General Background

2.1 Asymptotic Giant Branch Stars

The Asymptotic Giant Branch (AGB) is a late evolutionary phase of low- to intermediate-mass stars, that develop an electron-degenerate CO core after the phase of core helium burning. Initial masses of stars that experience the AGB are in the range $0.8 \lesssim M/\mathrm{M}_{\odot} \lesssim 8.0$, the precise boundaries depending on the other stellar properties and on the model details.

In the following sections we briefly recall the relevant features of evolution prior to and during the AGB. A more detailed explanation can be found in dedicated textbooks on stellar evolution (Kippenhahn et al., 2012; Hansen et al., 2004) or specifically on the AGB phase, such as the one by Habing and Olofsson (2004) or the review by Herwig (2005).

2.1.1 Evolution Prior to the AGB

Stars form as a consequence of the collapse and fragmentation of large clouds of interstellar matter. The gravitational contraction of the resulting proto-stars cause their central temperature to increase until nuclear reactions become possible.

A star is born as stable hydrogen burning develops in its core, the energy released by which is able to balance self-gravitation, keeping the system in hydrostatic equilibrium. This phase is called Main Sequence (MS), and is the first and longest-lived in the evolution of a star.

Hydrogen is converted into helium via two main series of nuclear reactions: the proton-proton (pp) chain, and the CNO cycle. Hydrogen is gradually depleted in the centre of the star, eventually leaving only the products of nuclear reactions, *i.e.*, an inert He core.

The energy source thus moves outwards from the core, to regions where hydrogen is still available: the star enters the Red Giant Branch (RGB) phase, and is powered by a H-burning shell on top the He core.

The shell is surrounded by an extended envelope through which energy is mainly carried by convective motions.

As the star climbs the RGB, the shell becomes increasingly thin and burns H into He that is dumped onto the core, which grows in mass and while slowly contracting. In presence of a shell energy source, stellar layers move in a symmetric fashion, in the sense that a contraction of layers below the shell is accompanied by an expansion of

the layers above the shell, and vice versa. In other words, the shell acts as a mirror for stellar mass motions, a fact commonly known as "mirror principle".

The mirror principle is well known based on empirical observation and supported by numerical simulations, and is essentially a consequence of the conservation of gravitational potential energy and thermal energy (see, *e.g.*, Kippenhahn et al., 2012).

Meanwhile, the outer envelope expands and cools down, becoming increasingly unstable to convection, that penetrates deeper and deeper inwards. As it reaches the layers enriched in products of nuclear reactions, they are mixed into the envelope and brought to the surface, altering its chemical composition.

This kind of process is called "dredge-up", and may occur multiple times during the life of a star, the one occurring during the RGB being known as first dredge-up (1DU). By mixing products of the CNO cycle into the stellar envelope, it causes a decrease of the abundance of carbon and oxygen, while it increases that of nitrogen. Isotopic ratios are also affected, such as in the case of C^{12}/C^{13} that exhibit a decrease. Additionally, surface He abundance is slightly increased (see Habing and Olofsson, 2004, and references therein for a more detailed description).

As a consequence of contraction, the core heats up, eventually to the point that helium can be burnt into carbon via the 3-α reaction. The star thus enters the core He-burning phase.

The transition is however not the same for all stars. Indeed, by the end of the RGB, stars less massive than about $1.8\,M_\odot$ have developed an electron-degenerate He core.

Degenerate matter is not able to react to an increase in temperature by expanding, therefore the energy released from He-burning reactions quickly leads to a thermal runaway known as the Helium Flash.

In contrast, massive enough stars move to the core He-burning phase in a non-violent way.

In both cases, the star ends up in a stable configuration where helium is burnt in a convective core, while hydrogen is burnt in a surrounding shell, which still provides for a relevant fraction of the stellar luminosity.

When enough ^{12}C is produced by the 3-α reaction, carbon burning becomes efficient in producing ^{16}O, so that the He core is gradually transformed in to a CO core.

2.1.2 Evolution During the AGB

The AGB phase, divided into early-AGB (E-AGB) and the thermally pulsing AGB (TP-AGB), follows the to exhaustion of He in the stellar core.

We will give here a summary of AGB evolution, followed by a few paragraph describing some characteristic processes and features of this evolutionary phase. Pulsation on the AGB is discussed in detail in section 2.2.

At the beginning of AGB, he star undergoes a brief transition, during which He-burning moves into a shell surrounding the contracting CO core, while the H-shell is still active. Due to the mirror effect of shell-burning sources, the outer envelope also contract, while the He-rich region undergoes an expansion and its temperature decreases.

As a consequence, the H-burning shell is extinguished, and the envelopes stars expanding, and convection penetrates inwards The star is now powered by the He-burning shell alone, and is experiencing the E-AGB phase. Helium reactions add mass to the growing CO core, which density increases to the point that it becomes electron-degenerate.

In massive enough stars ($M \gtrsim 4\,M_\odot$), convection can reach the region that had been processed by H-burning reactions, and another dredge-up episode (the second dredge-up, 2DU) can occur.

As helium produced by the H-burning shell gets depleted, the He-burning shell becomes weaker, causing the layers above to contract and heat up.

As a consequence, H-burning is re-ignited, and the star is now powered by two shells. This marks the end of the E-AGB and the beginning of the TP-AGB.

This phase is characterised by a repeated pattern (Fig. 2.1), called a thermal pulse cycle (TPC), during which the two shells are alternately active.

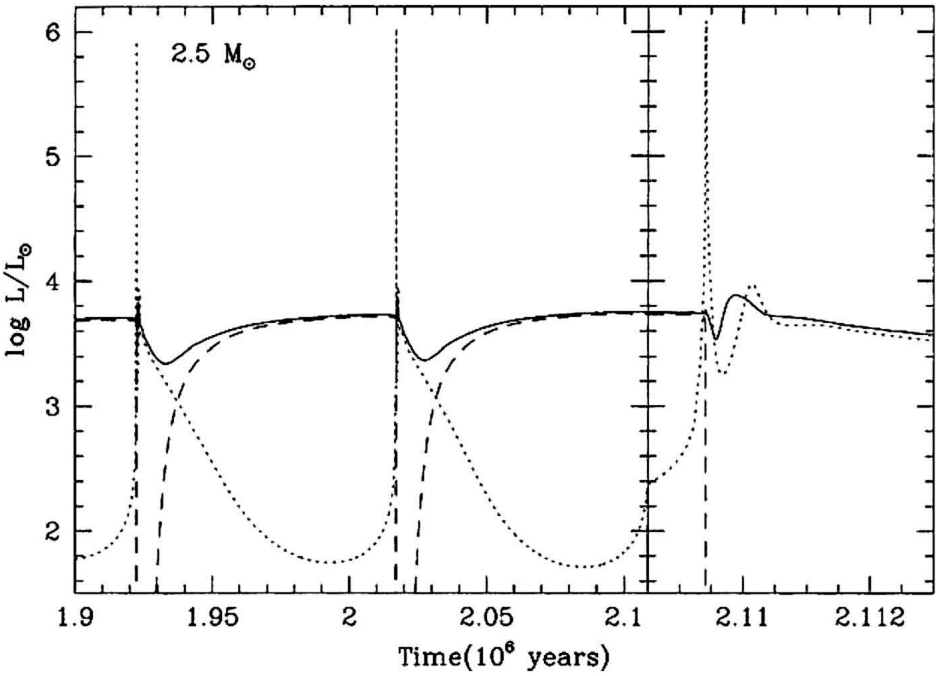

Figure 2.1: Surface luminosity (solid line), H-burning luminosity (dashed line) and He-burning luminosity (dotted line) as a function of time for three thermal pulses in a $2.5\,M_\odot$ TP-AGB model. The third pulse is shown against an expanded time axis on the right panel (adapted from Habing and Olofsson (2004), models by Vassiliadis and Wood (1993)).

For most of the cycle, the He-burning shell is dormant (this is often referred to as "quiescent" evolution), and energy is provided by the H-burning shell, which products pile up on top of the core, increasing temperature and pressure below the shell.

Eventually, this leads to a re-ignition of the He-burning shell, a process occurs violently, similarly to the helium flash.

This is due essentially to two reasons. First, the 3α reaction has a strong dependence upon temperature, so that a positive temperature perturbation, though small, leads to a large increase in energy generation.

Second, the surplus heat is added at constant pressure in the shell, so that it leads to further increase in temperature, causing a thermonuclear runaway. The constant pressure in the shell can be explained by the fact that it is essentially due to the weight of the layers above. Since the shell is very thin with respect to the envelope radius, its expansion due to the temperature perturbation is not able to lift the above layers

enough to change the pressure they exert upon it.

This event, called helium shell flash or thermal pulse, releases a huge amount of energy ($\sim 10^8\,L_\odot$) in a very brief period of time. That much energy cannot be transported by radiation alone, so that a convective region develops between the locations of the two shells (intershell convection zone - ICZ - or pulse-driven convection zone - PDCZ; see Fig. 2.2). Convection mixes ^{12}C from the 3α reaction throughout the intershell region.

The shell flash causes an expansion of the intershell region, that break the thermal runaway leaving a stable He-burning shell, while the hydrogen shell is shut down.

Fuel consumed by the He-burning shell is thus not refilled, causing it to become gradually weaker, and the intershell convection zone to disappear.

During this stage convection from the envelope can penetrate down to the layer below the position of the now extinct H-burning shell, and can mix products of nuclear reactions to the surface (a third dredge-up event, see below).

In the meanwhile, the H-burning shell recovers strength, and the star enters again a quiescent phase, entering the next cycle.

The large infrared excess in the spectra of AGB stars is an evidence that they have strong stellar winds (see also the sections below), which lead to mass-loss from the surface of the star.

The phenomenon is connected with stellar pulsation, and the associated mass-loss becomes particularly efficient towards as the star approaches the very end of its evolution.

Strong mass-loss is in fact the cause of the termination of the TP-AGB evolution: during this so-called "super-wind" phase, the H-rich envelope is rapidly expelled, and the star begins to shrink.

It then evolves towards higher effective temperatures at essentially constant luminosity, moving to the post-AGB domain. Later, it will become the central star of a planetary nebula, and eventually a white dwarf.

The Third Dredge-Up and Carbon Stars

In some cases, while the H-burning shell is inactive, envelope convection can penetrate down to the intershell region, and bring the products of nuclear reactions to the surface. This process, called a third dredge-up (3DU) episode,

The repeated occurrence of 3DU events causes the surface layers to be enriched in *s*-process elements, He, and the products of He burning, in particular ^{12}C.

Depending on the efficiency of the process, the surface abundance of carbon by number can exceed that of oxygen (C/O > 1), leading to the formation of carbon stars.

3DU events can only happen in massive enough stars, and only for "well developed" thermal pulses, *i.e.*, several thermal pulses after the first one (in fact, the maximum luminosity of the shell flash, which facilitates the occurrence of a dredge-up, tends to increase at each pulse).

However, the precise conditions for which a 3DU event can take place are largely uncertain, as well as its efficiency in mixing material into the envelope.

The dredge-up efficiency is usually described in terms of a the parameter defined as:

$$\lambda = \frac{\Delta M_{\rm dup}}{\Delta M_{\rm c,tpc}}\,, \tag{2.1}$$

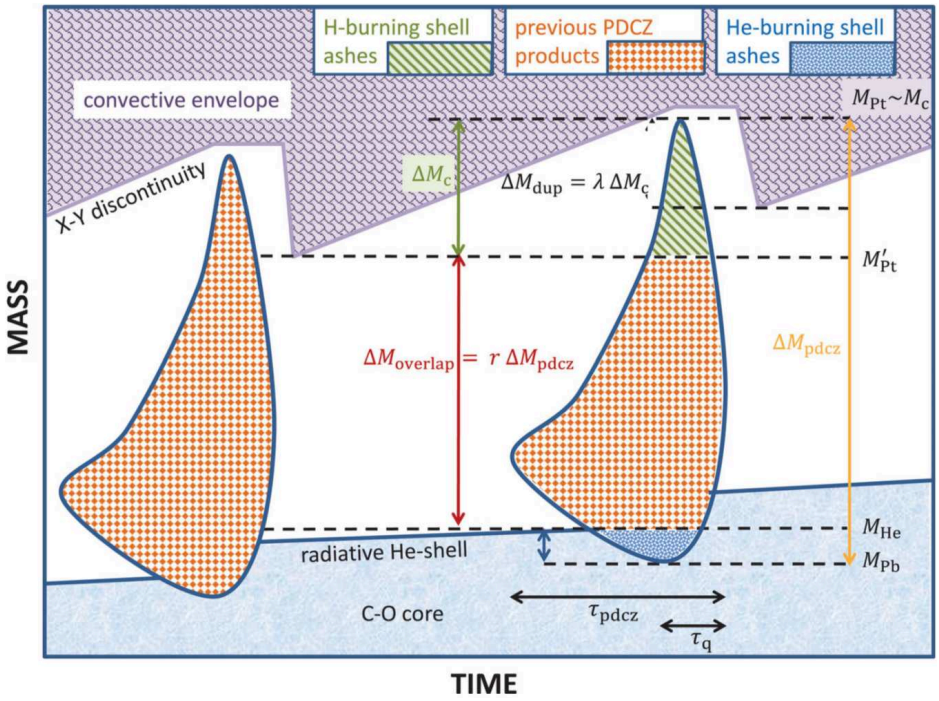

Figure 2.2: Schematic view of the evolution of the inner layer of a TP-AGB star during and between two consecutive thermal pulses (mass and time coordinates are not in real scale, reproduced from Marigo et al. (2013)).

representing the ratio between the amount of mass dredged-up during a thermal pulse and the amount of mass by which the core has grown during the previous interpulse period (see also the schematic depiction in Fig. 2.2).

The uncertainty by which this quantity is affected is well represented by the large differences between the predictions of different authors, as shown in Fig. 2.3.

Mass-Loss

Processes involved in mass-loss, regardless of the evolutionary phase, are highly uncertain and poorly understood.

In general, mass-loss is treated by means fitting relations derived either from observational evidences (color excess, expansion velocities) or based on theoretical models.

A prominent parameter involved in such relations is the luminosity, the increase of which leads to higher mass-loss rates, with a steep growth.

In TP-AGB stars, mass-loss observed mass-loss rates ar strongly correlated with observed pulsation periods (see Fig. 2.4).

The mechanism responsible for mass-loss is thought to be a combination of large-amplitude pulsation (probably in the fundamental radial mode), dust formation and radiation pressure acting on dust grains over a broad spectral range. This process is called pulsation-assisted dust-driven wind.

The key agents allowing for dust formation are (1) the third dredge-up, that enriches the surface of CNO products, (2) the low temperature conditions in the atmospheres of such extented red giants, and (3) large-amplitude pulsations, who induces shock waves through the atmosphere, allowing the gas to reach high enough densities for dust to

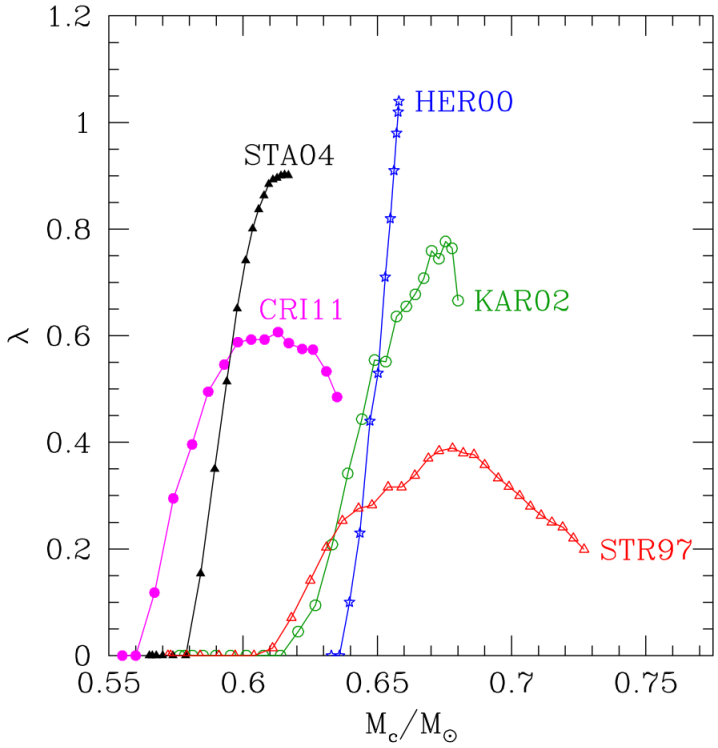

Figure 2.3: Efficiency λ of the third dredge-up as a function of the current core mass $M_{\rm c}$ during the TP-AGB evolution of a stellar model with initial mass $M_i = 3.0\,{\rm M}_\odot$ and initial metallicity $Z_i = 0.02$. Predictions from full AGB calculations of various authors are compared, showing large differences from each other. Labels are: CRI11 (Cristallo et al., 2011), WEI09 (Weiss and Ferguson, 2009), STA05 (Stancliffe et al., 2005), STA04 (Stancliffe et al., 2004), KAR02 (Karakas et al., 2002), HER00 (Herwig, 2000) and SRT97 (Straniero et al., 1997) (adapted from Marigo et al. (2013)).

condense.

Mass-loss rates in TP-AGB stars can become as high as $10^{-4}\,{\rm M}_\odot$/yr, so that stellar winds play a crucial role in the termination of AGB evolution by ultimately causing the expulsion of most of the stellar envelope.

An important consequence of such strong stellar winds is that the star becomes gradually obscured by a thick circumstellar envelope. This effect is evident both in CMDs and in period-luminosity diagrams, where stars with the largest intrinsic luminosities appear faint even at near-infrated wavelength.

An workaround to this problem, commonly used in the study of long-period variables, involves the use of so-called Wesenheit indices, linear combinations of colours and magnitudes able to partially remove the reddening from circumstellar dust (see section 2.2.2).

Nucleosynthesis and Hot-Bottom Burning

Nucleosynthesis during the AGB involves mostly the burning of H and He, and the production of *s*-elements via slow neutron captures.

The mixing induced by repeated third dredge-up episodes plays an important role not only in taking processed material towards the surface, but also in leading it to

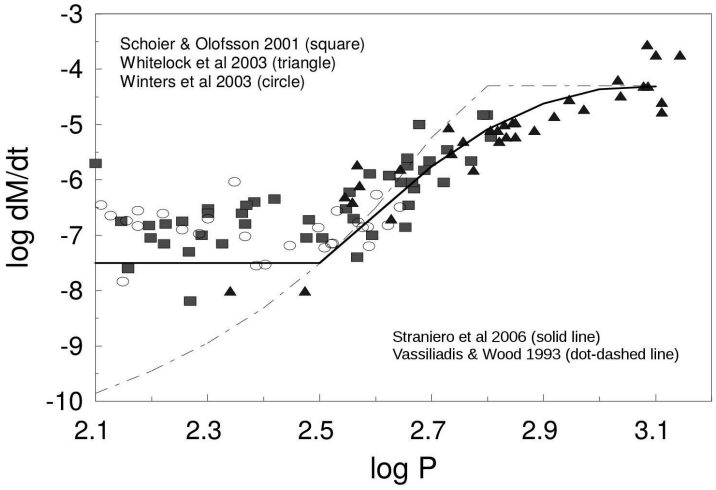

Figure 2.4: Observed mass-loss rates and periods (from Schöier and Olofsson (2001), Whitelock et al. (2003) and Winters et al. (2003)), compared with analytic prescriptions for the mass-loss rate commonly employed in evolutionary calculations (from Straniero et al. (2006) and Vassiliadis and Wood (1993)). Adapted from Straniero et al. (2006).

subsequent passages through the H-shell region. This results in a combination of H and He processed material.

The main products of AGB nucleosynthesis are ^{4}He, ^{12}C, ^{14}N and, in smaller amounts, ^{16}O, ^{19}F, ^{22}Ne, ^{23}Na, ^{25}Mg, ^{26}Mg, ^{26}Al, and ^{27}Al.

Additional species can be produced in case of Hot-Bottom Burning (HBB). This process takes place in stars more massive than $\sim 4\,M_{\odot}$ (depending on metallicity and models details), where the innermost region of the convective envelope can reach temperatures high enough for nuclear reactions to occur at efficient rates.

The time scales of convective turnover in such stars are shorter than the time interval between two consecutive thermal pulses, and comparable with the nuclear burning time scale of some species. Thus, the modelling of HBB requires an appropriate prescription to describe convective mixing (usually, it is described as a diffusive process).

Nuclear reactions involved are those active in the H-burning shell, *i.e.*, the pp chain and the CNO cycle, as well as other processes, such as the Ne-Na and Mg-Al cycles (thanks to the conditions favorable for proton capture reactions), and the production of ^{7}Li, involved in the pp-2 and pp-3 branches of the pp chain.

Lithium-7 is produced via the so-called Cameron-Fowler beryllium transport mechanism. ^{7}Be is produced by reactions of ^{3}He and ^{4}He at the bottom of the convective envelope. If exposed to high temperatures, the ^{7}Be can capture a proton to complete the pp-3 chain.

However, if it is brought to cooler regions by convective motions, it can alternatively capture an electron and produce ^{7}Li, which would thus be subject to proton captures and close the pp-2 chain.

Moreover, HBB is responsible for the destruction of ^{12}C and ^{18}O, via reactions of the CNO cycle that lead to the production of ^{13}C. This can sensibly alter the surface composition and inhibit the formation of carbon stars.

The Core Mass–Luminosity Relation

It was first shown by Paczyński (1970), based on evolutionary calculations, that TP-AGB stars follow a core mass-luminosity relation.

The basic reasons for the existence of this kind of relation are that (1) since the core is electron-degenerate, its structure is independent of its thermal properties, and depends only on its mass, (2) the envelope is so extended that it exerts very little weight on the core, and thus the structure of the whole star depends only on the core properties (*i.e.*, its mass), and (3) the whole energy (during quiescent phases) is produced by the H-burning shell at a rate that depends essentially upon the properties of the core.

It is immediately clear that such a relation does not hold during the luminosity dip associated to a thermal pulse. More generally, the relation breaks down in a number of cases, such as TPC in which the thermal pulses are not yet well developed or in stars undergoing HBB. Fig. 2.5 shows an example of models in which the relation does not hold.

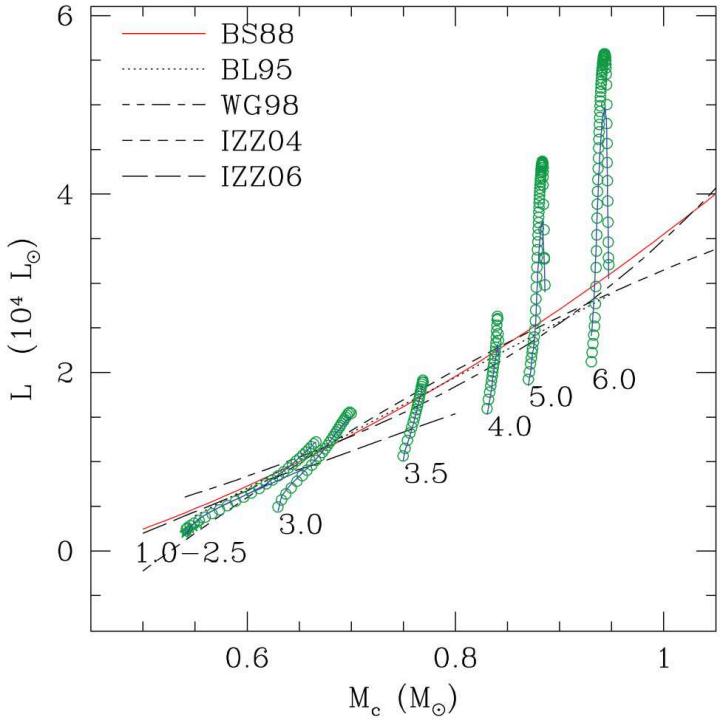

Figure 2.5: Stellar luminosity as a function of the core mass at the quiescent pre-flash stage preceding each thermal pulse, for TP-AGB models from Marigo et al. (2013) (green empty circles), with initial metallicity $Z_i = 0.008$ and initial masses indicated by labels. Blue lines superimposed to circles are full[a] TP-AGB models by Karakas et al. (2002) for the same Z_i, M_i and evolutionary stages. A few core mass-luminosity relations from various authors are plotted: BS88 (Boothroyd and Sackmann, 1988), BL95 (Bloecker, 1995), WG98 (Wagenhuber and Groenewegen, 1998) IZZ04 (Izzard et al., 2004), IZZ06 (Izzard et al., 2006) (adapted from Marigo et al. (2013)).

[a] See section 4.2 for more details on "full" and "synthetic" TP-AGB models.

2.2 Variable Red Giant Stars

Variability is a very common phenomenon in red giant stars. It is has been argued that all red giants are variable to some degree, although this is still an open question (see, *e.g.*, Catelan and Smith, 2015, their chapter 8, and references therein).

Among the different causes of variability, we are only interested here in stellar oscillations, therefore extrisinc variables (such as binaries) or non-periodic ones (such as irregular variables) are not in generally discussed here. In the following sections, we will spend some words on how variable red giants are classified and describe the general features of the types of stars we are mainly interested in, the Miras and Semi-Regular variables, collectively known as long-period variables (LPVs).

A significant development of our understanding of LPVs came with observations of the Galactic Bulge and the Magellanic Clouds from microlensing surveys, in particular MACHO (Alcock et al., 1992, 1993) and OGLE (Optical Gravitational Lensing Experiment, Udalski et al., 1992, 2008). We thus briefly describe the OGLE classification of variable red giants, that is also the one used in the present work. A more detailed description is postponed to chapter 5, where the observations of LPVs in the Large Magellanic Cloud (LMC) are described.

Less evolved red giants are known to exhibit solar-like oscillations. We include a brief description of such stars, although they are not among the subjects of our work. They are however relevant on the light of some recent attempts to find a connection between solar-like oscillations on the RGB and large-amplitude AGB pulsators (Soszyński et al., 2007; Mosser et al., 2013; Stello et al., 2014), and possibly a common excitation mechanism (Christensen-Dalsgaard et al., 2001; Xiong and Deng, 2013), for which a final paragraph is reserved in this chapter.

2.2.1 Classification of Variable Red Giants

Stellar variability, in general, displays many different features, so that variable stars have long been categorised in distinct classes (or types), based on purely observational criteria. Given to the different instrumentation the observations were carried on with, and to the specific requirements of different studies, a number of classification schemes have been used over the years. We will briefly discuss here the ones relevant in the study of variable red giants.

Due to its large amplitude of pulsation, the red giant star *o*-Ceti (better known as Mira) was the first (periodic) variable to be discovered. Stars with a smaller amplitude of variability were only discovered when observational techniques improved enough. It is not surprising, thus, that the variability amplitude has long been a prominent criterion in the classification of variable stars. Eggen (1977), for instance, introduced a classification scheme based on V-band amplitudes, in which stars with amplitude larger than 2.0 magnitudes are classified as Large-Amplitude Red Variables (LARVs), those with amplitude between 0.5 and 2.0 magnitudes are classified as Medium-Amplitude Red Variables (SARVs), and the remaining ones, with amplitudes smaller than 0.5 magnitudes, are called Small-Amplitude Red Variables (SARVs).

A more common classification scheme is the one employed in the General Catalogue of Variable Stars (GCVS, Samus' et al., 2017), also based (among other things) on variability amplitude. Stars with a V-band amplitude larger than 2.5 magnitudes are classified as Mira-like variables, or simply Miras. Red variables with smaller amplitudes, on the other hand, are classified as Semi-Regular variables (SR). The name stems

from the shape of their light curve, which may display poor regularity when compared to those of Miras, although this is not always the case. The first to introduce the distinction between Miras and SRs was probably Gaposchkin (1954). Miras and SRs are discussed in more detail in sections 2.2.2 and 2.2.3

The Mira and Semi-Regular variability types are also employed in the OGLE classification, although with slightly different definitions. Also, OGLE Semi-Regular Variables are generally abbreviated as SRVs. An additional type was introduced for OGLE variables by Wray et al. (2004), the OGLE Small Amplitude Red Giants (OSARGs). In contrast with most other classifications, they are not defined from some individual feature (such as amplitude, period, or the shape of the light curve), but rather in relation to the bulk properties of the population of LPVs they belong to, as explained in more detail in section 2.2.4.

2.2.2 Mira Variables

Miras are among the most luminous LPVs, and the most easily detectable due to their large amplitude. Therefore, they have been historically the most studied. The prototype star star for this class, *o*-Ceti, was first recorded as variable in 1596 by D. Fabricius, and is actually the first known observed variable star.

Mira variables are evolved stars believed to be reaching the end of the TP-AGB phase. The typical mass usually assumed for a Mira star is roughly $1\,M_\odot$. This is based on kinematic studies of galactic Miras showing properties characteristic of old disc stars. The oldest Miras in globular clusters have masses around $0.6\,M_\odot$, while younger ones, with ages of a few 10^8 yr, evolved from main-sequence progenitors as massive as $\sim 6\,M_\odot$.

Miras are giants of spectral types M or later, with low effective temperatures ($\sim 3000\,K$) and very large radii. As discussed in section 2.1, dredge-up events associated to thermal pulses are able to significantly alter the abundances of CNO elements in the envelope, generally described in terms of the number ratio C/O of carbon with respect to oxygen. C-type stars, having $C/O > 1$, are characterised by different spectral features than M-type stars, and have lower effective temperatures and larger radii, which would be expected to reflect in their pulsation periods.

Being such expanded stars, both M- and C-type Miras have long periods, in the range 80-1000 days. They also exhibit light curves with regular shapes and amplitudes between 2.5 and 11 magnitude in the visual. Such large values of visual amplitude do not reflect the actual change in luminosity during the pulsation cycle. Bolometric amplitudes, indeed, are generally around 1 magnitude, as first shown by Pettit and Nicholson (1933). More generally, the variability amplitude decreases towards longer wavelengths, as clearly shown in (Habing and Olofsson, 2004, Fig. 2.44), which collect observations of the oxygen-rich Mira variable RR Scorpii by Eggen (1975a) and by Catchpole et al. (1979)).

The reason for this behaviour is two-fold. First, it is due to a temperature effect. Miras are cold stars, so they emit most of their light in the infrared. Emission at visual wavelengths comes from the Wien tail of the spectral energy distribution, which exhibit a relative variation much larger than the Rayleigh-Jeans portion as a consequence of the fluctuations of effective temperature during the variability cycle.

The main cause for the large visual amplitude, however, is connected with molecular opacity, as first shown by Smak (1964) (see also the more recent discussion by Reid and Goldston (2002)). When the star is at maximum brightness it is smaller and

hotter, while it expands and cools down towards maximum brightness. This latter phase favours the formation of metallic oxides molecules (such as TiO in O-rich stars) that cause a significant increase of opacity at visual wavelengths, so that the observer can only see to a shallower in the atmosphere. A these wavelengths, the photosphere can become twice as large during the cycle, and as cold as $\sim 1400\,\mathrm{K}$. Therefore, only a small amount of visible light emerges the star at minimum brightness with respect to the maximum brightness phase. In contrast, the effect is smaller in the infrared as such wavelengths are less affected by molecular opacities.

This effect is more commonly seen in O-rich Miras than in the C-rich ones, the latter being intrinsically dimmer in visual bands. In the case of C-stars, a similar effect is likely caused by different sources of molecular opacity, such as C_2 or CN (Reid and Goldston, 2002).

Miras are single-mode radial oscillators, but the actual mode they pulsate in has been a matter of debate for a rather long time. In principle, that information can be obtained via the period-mean density relation, provided one has a reasonable knowledge of the pulsations from theory as well as good enough estimates of the stellar mass and radius. Periods depend more strongly upon radius than mass, and the physical radius of a star, especially such an evolved star, is not easy to determine. Indeed, much of the debate was due to uncertainties in the knowledge of stellar radii, and in particular the existence of an extended, cool atmosphere, unaccounted for, led Tuthill et al. (1994) to overestimate the diameter of the Mira variable R Leonis, supporting the idea of Miras as first-overtone pulsators. More accurate measurements of Mira radii from later interferometric studies shift the balance in favour of the fundamental mode being excited in Miras, also confirmed by results from linear and non-linear pulsation models (Wood and Sebo, 1996; Ireland et al., 2008). Very strong evidence from the MACHO microlensing survey provided a definitive answer (see section 2.2.4), and there is now general agreement that Miras are fundamental radial mode oscillators.

Period-Luminosity Relation

Miras, as many other classes of variable stars, follow a Period-Luminosity (PL) relation[1]. It has been the subject of many studies during the last century, as summarised, *e.g.*, in Feast et al. (1989) or in the recent work by Yuan et al. (2017).

The first to draw attention towards this subject was Gerasimovic (1928), who attempted a derivation of the relation for a sample of nearby LPVs for which proper motions were available. Relations derived in visual passbands (Gyllenberg, 1929, 1930; Wilson and Merrill, 1942; Clayton and Feast, 1969) were affected by significant scatter.

Relevant improvements were achieved by extending the relations to bolometric (Eggen, 1975b) as well as near-infrared magnitudes (Robertson and Feast, 1981), and by extending the study to variables in the LMC (Glass and Evans, 1981; Glass and Feast, 1982b) so to overcome the issue of the uncertain distances of local variables. Indeed, the infrared and bolometric PL relations of Miras in the LMC turned out to be rather precise (with a dispersion of ~ 0.25 magnitudes), and were further refined by Feast (1984) and later by Glass et al. (1987), who reduced the scatter to less than 0.15 magnitudes.

Feast et al. (1989) investigated in detail the PL relation, as well as the Period-

[1]The expressions "PL relation" and "PL sequence", although not equivalent, will often be used interchangeably here.

Luminosity-Colour (PLC) relation, of Miras in the LMC by obtaining near-infrared observations with appropriate phase coverage of the variability cycle. They found similar PL relations in the K-band for C-rich and O-rich Miras, and showed that a sample of several O-rich Miras with periods longer than 420 days were overluminous with respect to the extrapolated PL relation. This was explained by Whitelock et al. (2003) as an effect due to excess luminosity coming from Hot Bottom Burning (HBB).

Observations from the MACHO and OGLE microlensing surveys confirmed and substantially extended previous results, as discussed in detail in section 2.2.4. In a recent work, Yuan et al. (2017) used OGLE-III data for the LMC (Soszyński et al., 2009) combined with $JHK_{\rm s}$ observations from the LMC Near-infrared Synoptic Survey (LMCNISS Macri et al., 2015) to further refine the near-infrared PL relation of Miras, following an approach based on the derivation of light-curve templates.

The PL relation of Miras in globular clusters was first found by Menzies and Whitelock (1985), and further explored by Feast et al. (2002) who confirmed it to be consistent with that of the LMC. The PL relation of LPVs in the globular cluster 47 Tuc was studied by Lebzelter and Wood (2005) using non-adiabatic pulsation models. They found the relations to be mass dependent, supporting the idea that luminous red giants undergo significant mass loss.

Miras in the Galactic Bulge have been studied, *e.g.*, by Glass and Feast (1982a); Feast (1986); Feast et al. (2002). Recently, Matsunaga et al. (2017) confirmed the detection of C-Miras in the Bulge, consistent with the PL relation of the LMC.

Note that a major issue in the characterisation of the PL relation of C-rich Miras is connected with the fact that the most luminous of them develop thick circumstellar dust shells, that cause them to appear much fainter even in near-infrared bands. As a consequence, they lie off the PL relation. A common (but rather simplistic) workaround to this issue involves the use of so-called Wesenheit indices, *i.e.*, linear combinations of magnitudes and colours, such as:

$$W_{\rm I} = I - 1.55\,(V - I)\ , \tag{2.2}$$

$$W_{\rm JK} = K_{\rm s} - 0.686\,(J - K_{\rm s})\ . \tag{2.3}$$

$$\tag{2.4}$$

They constitute a measure of luminosity that is approximately reddening-free. The use of Wesenheit indices allows one to bring even the heavily reddened stars back to the corresponding PL relation. Soszynski et al. (2005) showed that the $W_{\rm I}$ index can be used to separate O-rich from C-rich stars. A discussion on the use of Wesenheit indices applied to OGLE data can be found in Soszyński et al. (2009).

An alternative is that of studying the PL relation ad mid-infrared wavelenghts, as done, *e.g.*, by Riebel et al. (2015) using *Spizter* observations combined with OGLE data for the Magellanic Clouds.

A renewed interest in the PL relation of Miras as a promising distance indicator grew in the last years. Part of the interest is connected with the discrepancy in the determination of the Hubble constant from different methods, namely Cepheids in host galaxies of recent type Ia Supernovae (Riess et al., 2016) or inferred through cosmological measurements (Planck Collaboration et al., 2016). The main advantages of Miras as distance indicators, with respect for instance to Cepheids, are: (1) their smaller masses, implying their presence in all types of galaxies, regardless of their current star-forming activity, (2) their brightness and the tightness of their PL relation at infrared wavelength, making them suitable for the exploration of this spectral domain, of great

interest in modern astrophysics. A thorough discussion of the role of Miras as distance indicators can be found in Whitelock (2013) and Whitelock and Feast (2014).

2.2.3 Semi-Regular Variables

Semi-Regular Variables (SR) are defined as variable stars with pulsation amplitudes smaller than 2.5 magnitudes in the V-band. This class is further divided into four sub-groups, SRa to SRd, not all of which consist of giant branch stars. Indeed, SRc variables are red supergiants of spectral types M and later, while the SRd group consist of yellow/orange supergiants of spectral types F, G and K. They belong to different evolutionary phases than the RGB or AGB, and thus will not be further discussed here.

SRa variables show persistent periodicity. Stars of the SRb group, on the other hand, have smaller amplitudes and poor periodicity with respect to SRa variables. In other words, they really are "semi-regular", while the term is often considered to be misleading for SRa stars. This is discussed, *i.e.*, in Aerts et al. (2010), their section 2.5.4, and references therein, as well as in Lebzelter et al. (2002).

Variables of the SR class have on the average shorter periods than Miras. However, SR with the longest periods do have periods similar to those of Miras.

The less defined regularity in the light curve of SR variables is at least in part due to the fact that, in contrast with Miras, they are multi-periodic variables, as discussed below. The determinations of the oscillation modes of SR and Miras are connected. Given their shorter periods, SR have often been assumed to pulsate in higher overtones than Miras. Support for this came with observations by Wood and Sebo (1996), who found a second PL relation of LPVs in the LMC, with periods approximately 2 times shorter than those of the Mira PL relation. Bedding and Zijlstra (1998) found the second sequence to be populated only by SR variables, but that SR are present also in the Mira PL sequence. They also found several SR variables exhibiting double periods in agreement with both relations.

2.2.4 The PL Sequences of Luminous Red Giant Variables

It has already been discussed in sections 2.2.2 and 2.2.3 how the identification of the pulsation modes of LPVs is a complicate task. It has also been mentioned that observation of variable stars by microlensing surveys had a huge impact on this topic, allowing astronomers to grasp the larger picture of populations of variable stars as a whole. Given the connection and parallel development of the two fields, it is appropriate to describe in the current section how the interpretation of LPVs evolved by exploiting microlensing observations from the early 2000s to the present (see also Wood, 2015).

The most important results came from observations of the Large Magellanic Cloud. In fact, the LMC is an ideal laboratory for the ensemble study of variable stars, as they can be assumed to lie at approximately the same (known) distance from the observer, and are affected by small interstellar reddening.

As mentioned in the previous section, observations of LPVs in the LMC have been employed to study the PL relation of Miras and brought to the discovery of a second PL relation at shorter periods populated by Semi-Regular variables. A major breakthrough came with the advent of microlensing surveys such as MACHO and OGLE, that produced a large amount of collateral stellar variability data.

Using data from the MACHO database, Wood et al. (1999) reported the discovery of additional PL relations (or sequences) for a total of five (Fig. 2.6).

The implications of such a discovery, and their importance, are clearly explained by Wood (2000), who combined the MACHO observations with near infrared photometry in the J- and K-band.

Of the five sequences, labelled[2] with letters A to D, sequence C was found to match the PL relations of Miras described by Feast et al. (1989) and Hughes and Wood (1990). This, together with the fact that the largest amplitude variables of the sample were actually found on sequence C, strongly suggested that stars on that sequences are indeed Miras.

The shorter-period sequence labelled B was found to correspond to the one described by Wood and Sebo (1996). It hosts lower amplitude SR variables, that are also found in sequence C together with large amplitude Miras. Sequence A, with the shortest periods, was found to consist of very low amplitude variables (< 0.2 mag in V), that would later be known as OSARGs.

While sequences A, B, and C could be explained in term of stellar pulsation, the remaining sequences D and E proved more difficult to interpret. A few stars on sequence E were found to have light curves very similar to those of close eclipsing binaries or contact binaries. The binary explanation is now accepted for sequence E. Sequence D, on the other hand, is located at periods longer than those of sequence C. The variability responsible for sequence D, called Long Secondary Periods (LSP) is currently unexplained. Note that, according to the theory of adiabatic stellar oscillations, there is no mode with a period longer than the fundamental mode. Therefore, if sequence C, populated by Miras, does correspond to the fundamental mode, sequence D cannot be explained in terms of radial pulsation.

It is rather immediate to explain the existence of different sequences by pulsation in a several distinct modes. Various efforts had previously been done to match the observed sequences with pulsation models to constrain the corresponding pulsation mode. The problem is, one can reproduce a certain sequences with more than one mode just by changing the radius assumed for the models, *i.e.*, the effective temperature. The fact that the latter is poorly constrained makes so that a definitive answer could not be provided by the theory.

The key feature of the MACHO observations is the detection of several double- or triple-mode variables for which the periods could be measured. The observed period ratios provided a new, powerful constraint to be matched by theoretical model, making up for the poor knowledge of stellar radii. In fact, period ratios are much less dependent upon the radius than are the periods.

Note that, in absence of observations of multi-periodic variables, Wood and Sebo (1996) used the average separation between the PL relation of Miras and the second relation they discovered as a proxy for period ratios, assuming the two sequences corresponded to two distinct and adjacent pulsation modes. Comparison of observations with pulsation models provided strong evidence in favour of Miras being fundamental mode pulsators, and stars on the other sequences being either first or second overtone pulsators.

Wood et al. (1999) and Wood (2000) have used MACHO observations to confirm that result, showing that the PL sequences and the period ratios can be simultaneously reproduced by models only if sequence C is due to pulsation in the fundamental radial

[2]The nomenclature introduced by Wood et al. (1999) and extended by other authors is also the one generally used in this work. The correspondence between different nomenclatures is shown in table 2.1 (see also Soszyński et al., 2007).

mode. This allowed them to identify unambiguously Miras as fundamental mode pulsators. Models also showed sequences A and B to be consistent with pulsation in the 1st, 2nd and 3rd overtone modes. Semi-Regular variables are found in all sequences, including sequence C, so they can pulsate in all those modes and the fundamental mode.

The picture presented by Wood et al. (1999) was the starting point for a number of studies, which contribution was to increase the number of known variables in the LMC, as well as the number of sequences in its PLD.

In contrast with the original assumption by Wood et al. (1999) that all LPVs found by MACHO are AGB stars, the PL sequences are formed by both AGB and RGB stars. This was first shown by Ita et al. (2002), who identified the tip of the RGB in the K-band luminosity function, as well as the CMD, of variable stars in the LMC. This was confirmed by Kiss and Bedding (2003), who also showed that RGB variables form sequences slightly offset in period with respect to AGBs, which can be explained in terms by the fact that the two evolutionary phases have different temperatures at the same luminosity.

Using OGLE data combined with extensive near-infrared photometry, Ita et al. (2004b) found in the Small Magellanic Cloud (SMC) the same sequences as the ones described by Wood et al. (1999) in the LMC. They also investigate the structure of the sequences, confirming the discontinuities in sequences A and B at the luminosity of the tip of the RGB. Most importantly, they discovered that Wood's sequence B is in fact two sequences, labelled B and C$'$. It is likely that the "second sequences" observed by Wood and Sebo (1996) consisted of stars on both sequences B and C$'$.

The OGLE survey (in its different phases) provided a mean to explore stellar pulsation down to amplitude as small as a few 10^{-3} magnitudes in the I-band. This brought to the discovery of a large number of small-amplitude variables. Wray et al. (2004) studied such stars in the Galactic Bulge, and proposed the name OSARG (OGLE Small Amplitude Red Giants). They are now often considered an additional class alongside with Miras and Semi-Regular Variables (that are abbreviated SRV in the OGLE Collection of Variable Stars - OGLE-CVS). As noted by Soszyński et al. (2009), OSARG constitute the most numerous class of LPVs, and would be categorised as SR variables in the traditional classification scheme. In fact, the OSARG and SRV groups in overlap in any diagram that can be plotted using ogle data. Therefore, while Miras are easily classified as variables with an amplitude larger than 0.8 magnitudes in the I-band, an appropriate algorithm was devised by the OGLE group to classify OSARG (see Soszyński et al., 2007). In very simple words, the method can be summarised by saying that non-Mira variables are classified as SRVs if they have periods on sequences C and/or C$'$, but not on any of the shorter period sequences. Otherwise, they are classified as OSARGs.

Soszyński et al. (2004) discovered a faint sequence at the short periods side of sequence A, and named it a_4 (the label A$'$ will be usually employed here). They studied LPVs in the Magellanic Clouds, analysing separately OSARGs above and below the tip of the RGB ($K_{\rm s,tRGB} = 12.05$ or $W_{\rm JK,tRGB} \sim 11.3$ in the LMC). They found the bright ones to follow four distinct PL relations, a_1 to a_4, while stars in the other group appeared to follow only three sequences, b_1 to b_3. In their notation, smaller number in the subscript correspond to sequences with longer periods, while the letter "a" and "b" stand for "above" and "below" the tip of the RGB (although the a sequences also extend at fainter magnitudes). Note that, with the exception of the newly discovered sequence a_4 (A$'$), sequences a_3 (b_3), a_2 (b_2) and a_1 (b_1) are often identified with sequences A, B

and C′, respectively, being their direct continuation at low luminosity.

The PL relations of the two groups are slightly offset in periods, a confirmation of the findings of Ita et al. (2002) and Kiss and Bedding (2003), with the exception of sequence a_4 (*i.e.*, A′) for which a b counterpart was not observed. Soszyński et al. (2004) suggested that sequence A′ consist of AGB stars only. They use this feature to separate AGB stars from RGB ones below the tip of the RGB, identifying all variables with at least one period on sequence A′ as AGBs, and the remaining ones as RGBs (with possibly as small contamination by AGB stars).

Moreover, Soszyński et al. (2004) examined OSARGs in the period versus period ratios plane, the so-called Petersen diagram, and found that that sequence A consist of three closely spaced parallel ridges. Such ridges are too close to be due to distinct radial modes of low order, and thus constitute evidence that non-radial modes are also involved in the variability of luminous red giants. A similar fine structure was claimed by Soszyński et al. (2007) to be present in sequences A′ and B as well.

The distribution of observed periods between sequences C′ and C suggest the presence of a probable faint sequence, first noticed by Soszynski et al. (2005) and later investigated by Soszyński and Wood (2013) who identified it with the label F.

It is important to point out that most of the sequences described above are well defined only when a single period per star is shown (as in the bottom panel of Fig. 2.6 and the top panel of Fig. 2.7), rather than all three periods (as in the bottom panel of Fig. 2.7).

The period that is usually chosen in each star to be plotted is the so-called primary period. The other two periods are known as secondary and tertiary periods. This classification is based on the procedure employed in the analysis of the light curves. In the case of OGLE data (the ones used in the present work), the light curve is processed by means of Fourier analysis. The most significant periodicity, associated to the highest peak in the power spectrum, is labelled as primary period. In general, the primary period of a star is the one with the largest variability amplitude. A more detailed description of the process can be found in Soszyński et al. (2009) and references therein.

Interpretation of the PL Sequences as Different Pulsation Modes

Fig. 2.8, reproduced from Soszyński et al. (2007), gives a global idea of the complexity of the PL sequences of LPVs. It is important to note that

As already discussed, distinct sequences are attributed to different modes of pulsation. Concerning the evolution of LPVs, a picture have emerged for which there is general agreement. LPVs are low- to intermediate-mass stars evolving along the RGB or the AGB. At low luminosities, a few overtone modes of low radial order are unstable in such stars. The most unstable one, or dominant mode, is identified with the primary period in the observations. As a star evolves and expands, becoming brighter and cooler, the mode of order immediately lower than the dominant one becomes increasingly unstable, until it becomes the dominant mode itself.

Therefore, the evolution of a star along the AGB is accompanied by a series of shifts in the order of the dominant mode towards lower overtones, until eventually the fundamental mode becomes dominant. The star becomes a single-mode Mira variable, which variability amplitude grows to large values until eventually most of the stellar envelope is ejected due to strong mass loss, the star ceases to be observed as a variable and evolves towards the post-AGB phase.

While this picture is generally accepted, there is currently no agreement on what pulsation modes are involved in the evolution, and more precisely on the assignment of pulsation modes to different PL sequences. In the following, we list some of the main attempts to identify the oscillation modes associated to each sequence. A summary of this can also be found in Wood (2015).

Soszyński and Wood (2013) updated the work by Wood and Sebo (1996) by comparing OGLE observations with linear, non-adiabatic models of radial pulsation. They confirmed that the period ratios of variables in sequences C$'$ and C can be explained by assigning the fundamental mode to sequence C variables and the first overtone mode to those on sequence C$'$. They also found that theoretical growth rates qualitatively predict the existence of regions of instability of the 1O and fundamental modes that are consistent with sequences C$'$ and C, respectively. Note that they considered only SRV stars in their analysis, *i.e.*, rather bright stars.

An entirely similar study conducted by Takayama et al. (2013), but using a different pulsation code combined with evolutionary models, and focusing on RGB stars on sequences A, B and C$'$ (*i.e.*, sequences b_3, b_2 and b_1 of Soszyński et al. (2004)). They found them to be compatible with pulsation in the first, second and third radial overtone modes, respectively, as well as with some non-radial modes of angular degree $\ell = 1$ and 2, *i.e.*, dipole and quadrupole modes.

More recently, Wood (2015) performed a thorough examination of the PL sequences in the LMC, both from a purely empirical point of view and with a comparison of theoretical models with observation. He came to the conclusion that sequences A$'$, A, B, C$'$ and C are due to the fourth, third, second, first and fundamental modes, respectively.

Wood (2015) drew the attention to the fact that period ratios in individual stars do not agree with the ratios of the periods of the PL sequences, a fact that he attributes to differences in the average mass of stars in different sequences, *i.e.*, sequences with shorter periods host more massive stars. More precisely, he showed that for primary periods belonging to a given sequence, the secondary periods in the same stars are closer to the primary modes than are the adjacent sequences to the sequence under consideration. However, sequences B and C$'$ are an exception to this pattern, a fact that is closely connected to their being unusually close to each other.

He explained this by suggesting that, while sequences C$'$ and C are mainly associated with radial pulsation, variables on sequences A$'$, A and B are primarily dipole mode oscillators. Note that this is in agreement with the results of Stello et al. (2014), who investigated the evolution of adiabatic oscillations models up to the luminosity of the RGB tip, and compared the results with observations some of the most luminous red giants observed by *Kepler*. He found that modes of angular degrees $\ell = 0$, 2 and 1 (in increasing order of period) are excited in those stars for a given radial order, and that the dipole mode ($\ell = 1$) for the second and higher overtone modes, suggesting that indeed OGLE sequences A$'$, A and B may be dominated by dipole modes.

Studies mentioned above are essentially in agreement in terms of modal assignment. However, a number of other works came to conclusion in contrast with the above results.

Soszyński et al. (2007) studied the sequences of RGB variables, and compared them to pulsation models combined with isochrones broadly representative of the range of ages and metallicities of the LMC. They found reasonable agreement for the three RGB sequences with radial pulsation in the second and first overtone modes and the fundamental mode. They thus suggest that the four sequences of OSARGs are due to

the first four radial oscillation modes.

Their analysis is limited to RGB luminosities. They only speculate on the modes responsible for sequences C′ and C. However, they seem to stick to the idea that sequence C′ is due to the first overtone mode, and therefore that it does not form a continuous distribution with their sequences a_1 and b_1 of OSARGs (compare with Fig. 2.8). In fact, they support the idea that OSARG variables represent an intrinsically distinct population than that corresponding to SRVs and Miras, the ones found on sequence C′ and C. Note that, were sequences a_1 and b_1 a direct extension of C′ at fainter magnitudes, their modal assignment would identify the latter as well as pulsation in the fundamental mode, leaving no explanation for sequence C in terms of radial pulsation.

Dziembowski and Soszyński (2010) focused on stars having periods on both sequences A and B (*i.e.*, a_2 and a_3 or b_2 and b_3), and were able to reproduce them with models pulsating in the first and second overtone modes, in agreement with the results by Soszyński et al. (2007).

Their studies were also confirmed by Mosser et al. (2013) estimated global seismic parameters for RGB OSARGs in sequences A and B in order to compare them with solar-like oscillations in less evolved red giants observed with *Kepler*. They found a close match between sequences A and B and the first and second overtone modes, respectively.

Therefore, two different interpretations have developed, that are summarised in the following and in table 2.1. In the first one (we will refer to it as "interpretation *a*"), sequence C, containing the Mira variables, corresponds to pulsation in the radial fundamental mode, so that sequences C′, B, A, A′ correspond to the radial first, second, third and fourth overtone modes (Wood and Sebo, 1996; Wood et al., 1999; Wood, 2000; Soszyński and Wood, 2013; Takayama et al., 2013; Wood, 2015). In contrast, according to the other interpretation ("interpretation *b*"), sequences B and A correspond to the first and second overtone modes, sequence C′ is due to the fundamental mode, but no explanation is provided for sequence C (Soszyński et al., 2007; Dziembowski and Soszyński, 2010; Mosser et al., 2013). Note that both interpretations assume that the observed sequences correspond to distinct and adjacent radial orders of pulsation, and that there is a one sequence offset between the two sets of mode assignments.

2.2.5 Solar-like Oscillations in Red Giants

Stars evolving along the red giant branch exhibit small-amplitude, radial and non radial oscillations stochastically excited by convective motions. These kind of variability is called solar-like oscillations, and, although not part of the present work, it deserves at least some comments.

A clear description of solar-like oscillations can be found in the review by Chaplin and Miglio (2013).

Solar-like oscillations are associated to either *p*-modes, *i.e.*, standing acoustic waves, or *g*-modes, also called internal gravity waves, where buoyancy acts as a restoring force. Under suitable conditions, the two types of modes can couple into so-called mixed modes.

Oscillations of this kind are intrinsically stable, and driven by turbulent motions associated to sub-photospheric convection. Indeed, they have been observed in a variety of stars having an outer convective region, such as solar-type main-sequence stars, subgiants, red giants and, of course, the Sun.

Table 2.1: Pulsation modes assigned to the OGLE PL sequences by different authors. "Fund." stands for fundamental mode, while 1O, 2O, 3O and 4O stand for first, second, third and fourth overtone modes, respectively. The nomenclature used by each author to indicate observed sequences is also shown ("n.o." stands for "not observed").

Labels used here	A′	A	B	C′	C
Interpretation *a*					
Wood and Sebo (1996)	n.o.		2O or 1O		Fund.
Wood et al. (1999) and Wood (2000)	n.o.	A	B		C
		3O, 2O or 1O			Fund.
Soszyński and Wood (2013)	A′	A	B	C′	C
				1O	Fund.
Takayama et al. (2013)		b_3	b_2	b_1	
		3O	2O	1O	
Wood (2015)	A′	A	B	C′	C
	4O	3O	2O	1O	Fund.
Interpretation *b*					
Soszyński et al. (2007)	a_4	a_3,b_3	a_2,b_2	a_1,b_1	
	3O	2O	1O		
Dziembowski and Soszyński (2010)		b_3	b_2		
		2O	1O		
Mosser et al. (2013)		b_3	b_2		
		2O	1O		

Solar-like oscillations feature a characteristic pattern in their power spectrum, exhibiting numerous modes of different radial order and angular degree. Due to the effect of geometrical cancellation, however, only modes with the lowest angular degrees have observable amplitude (those with $\ell = 0$, 1, 2, and possibly 3).

Modes of consecutive radial order and the same angular degree are approximately equally spaced in frequency, by a quantity $\Delta\nu$ called large frequency separation, so that the power spectru is characterised by a comb-like pattern.

This large separation is proportional to the inverse of the sound travel time across a stellar diameter. Therefore, it carries information about the stellar interior.

The power spectrum shows a Gaussian-like modulation in frequency, centered at a frequency $\nu_{\max}$. The frequency of maximum power $\nu_{\max}$ is related to the surface properties of the star, and is connected to the acoustic cut-off frequency of the atmosphere.

Main sequence stars exhibit solar-like oscillations in modes of high radial order. As the star evolves and expands, $\nu_{\max}$ decreases, and high order modes get damped while lower orders become excited. Meanwhile, the Gaussian envelope of the spectrum shrinks, so that the number of excited modes decreases.

2.2.6 Excitation Mechanism

The excitation mechanism responsible for pulsation in long-period variables is poorly understood and affected by large uncertainties.

It is clear that a major role is played by convection, that is able to efficiently input energy in pulsation motions. Convective transport itself, unfortunately, is one of

the least understood physical processes, and is commonly treated by means of rough simplifications.

Most importantly, we lack a solid understanding of the coupling between convection and pulsation. A complete discussion of this subject is beyond the scope of this work, and we refer the reader to the review by Houdek and Dupret (2015).

A first attempt to a realistic description of this process was made by Gough (1967), who included in his linear treatment the perturbations to both the enthalpy flux and the momentum flux, concluding that the latter can stabilise of drive oscillations depending on the length of pulsation periods with respect to the characteristic time scale of convection.

Balmforth et al. (1990) found that the inclusion of turbulent pressure produces a driving effect on pulsation.

Xiong et al. (1998) identified the main stabilising agent in linear models of Mira variables to be the perturbation to the momentum flux, together with the turbulent eddy viscosity. On the other hand, Munteanu et al. (2005) and Olivier and Wood (2005) found it to act as a driving mechanism in non-linear models.

Following the rise of interest towards solar-like oscillations in red giants, many different authors investigated the possibilty of a connection between long-periods variables and less evolved red giants in terms of the excitation mechanism.

It has been often proposed (*e.g.*, Kiss and Bedding, 2003; Soszyński et al., 2007; Christensen-Dalsgaard et al., 2009; Dziembowski and Soszyński, 2010; Mosser et al., 2013; Bányai et al., 2013; Xiong and Deng, 2013) that small-amplitude LPVs (*i.e.*, OSARG variables) are actually excited by the same mechanism responsible for solar-like oscillations, the stochastic driving associated to vigorous surface convection.

In particular, Mosser et al. (2013) were able to extend asteroseismic relations valid for the brightest M giants in a sample of *Kepler* observations to luminosity characteristic of OGLE variables, and found a good agreement, strongly pointing towards a connection between the two kind of variable stars.

From the theoretical point of view, the work of Xiong and Deng (2013) is relevant. They computed non-adiabatic pulsation models for evolutionary models of mass between 0.6 and 3.0 $\mathrm{M}_{\odot}$, from the main sequence to the AGB up to $\log(L/\mathrm{L}_{\odot}) \sim 3.5$.

By including a non-local, time-dependent treatment of convection, they were able to analyse in some detail the interaction of convection and oscillations and its effect on pulsational stability.

Their result suggest that the importance of different terms in the perturbed equation of energy transport changes with luminosity. For instance, they found that turbulent convection can act both as a damping and as a driving mechanism, and that models behave as solar-like oscillators at low luminosity, but as Mira-like variables towards high luminosities.

Therefore, a complete, realistic description of the driving of oscillation in presence of extended convective regions is still missing.

To achieve that goal, appropriate descriptions of non-local, time-dependent convection, and of the convection-pulsation interaction are required.

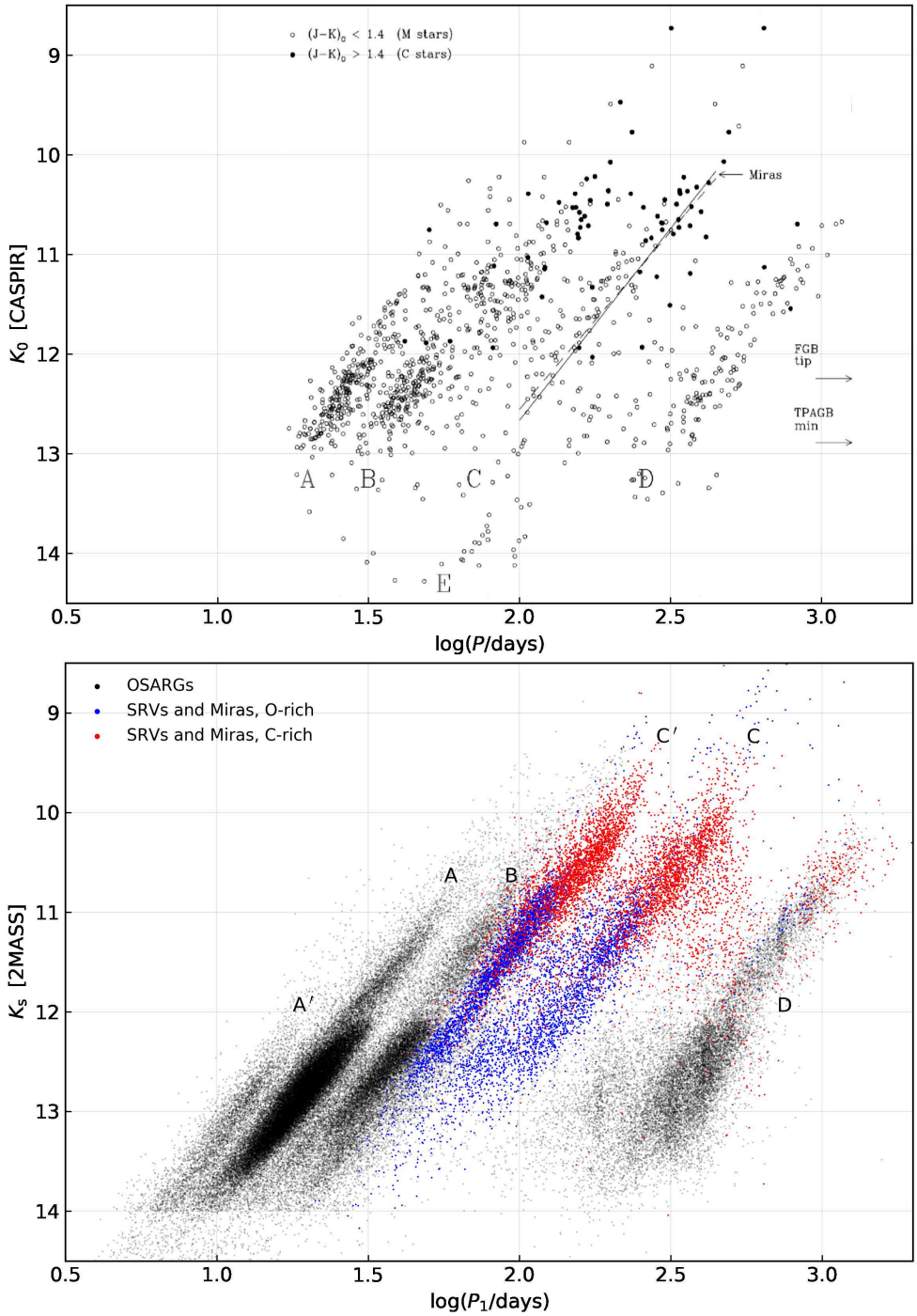

Figure 2.6: Top panel: the PL sequences found in the LMC as seen by MACHO (adapted from Wood et al. (1999)). M-stars ($J-K_0 < 1.4$) and C-stars ($J-K_0 > 1.4$) are shown as open and solid circles, respectively. Bottom panel: the PL sequences of the LMC from OGLE observations (Soszyński et al., 2009) with 2MASS photometry (Skrutskie et al., 2006). The additional sequences A′ and C′ are evident. Sequence E, not due to stellar pulsation, is not shown. Miras and SRVs are shown as blue or red dots depending on whether they are M- or C-type stars, respectively (based on a photometric classification).

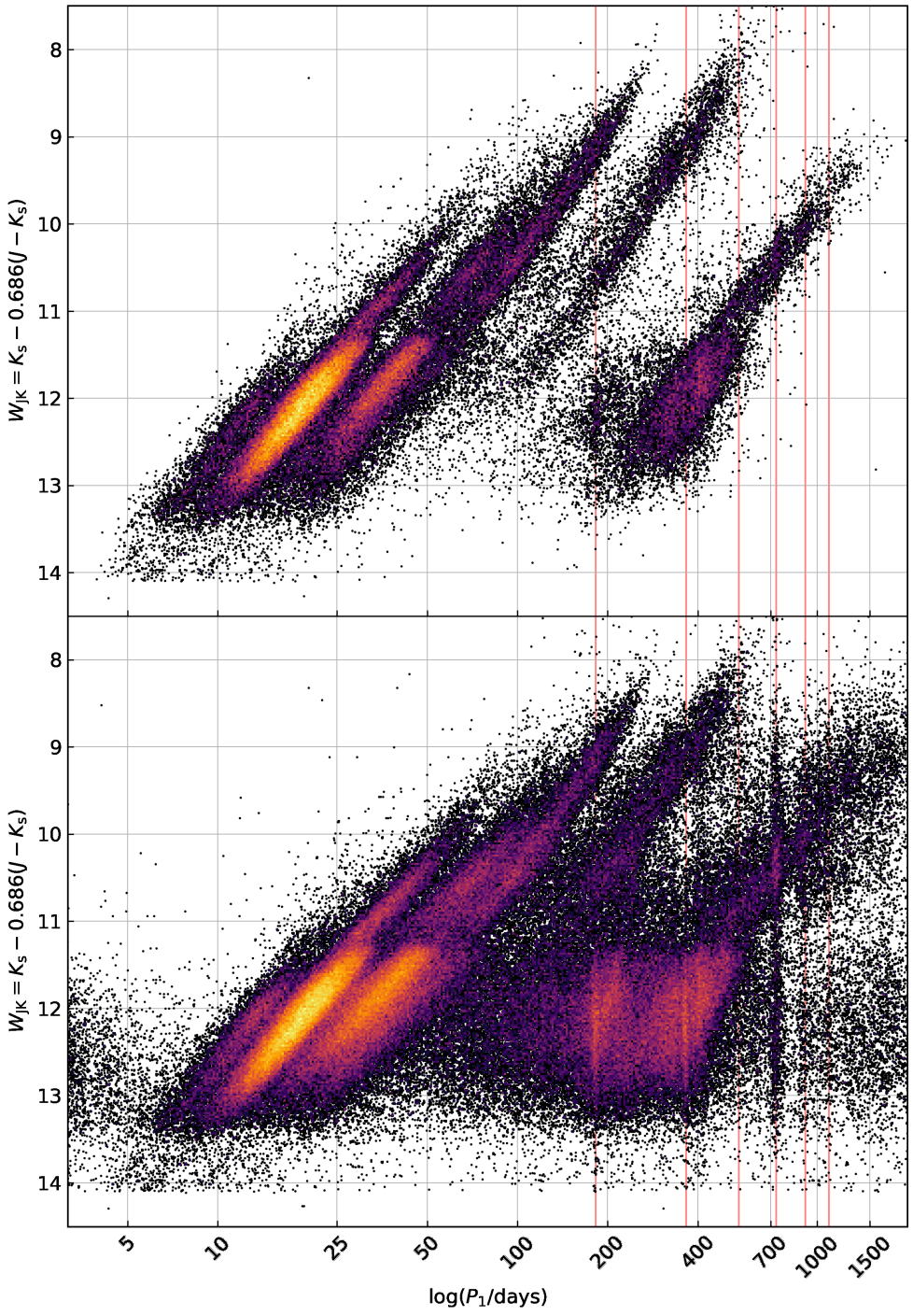

Figure 2.7: Period versus $W_{\rm JK}$ Wesenheit index of LPVs in the LMC plotted with data from the OGLE-III CVS. Primary periods only are shown in the top panel, while all three periods of each star are displayed in the bottom panel.

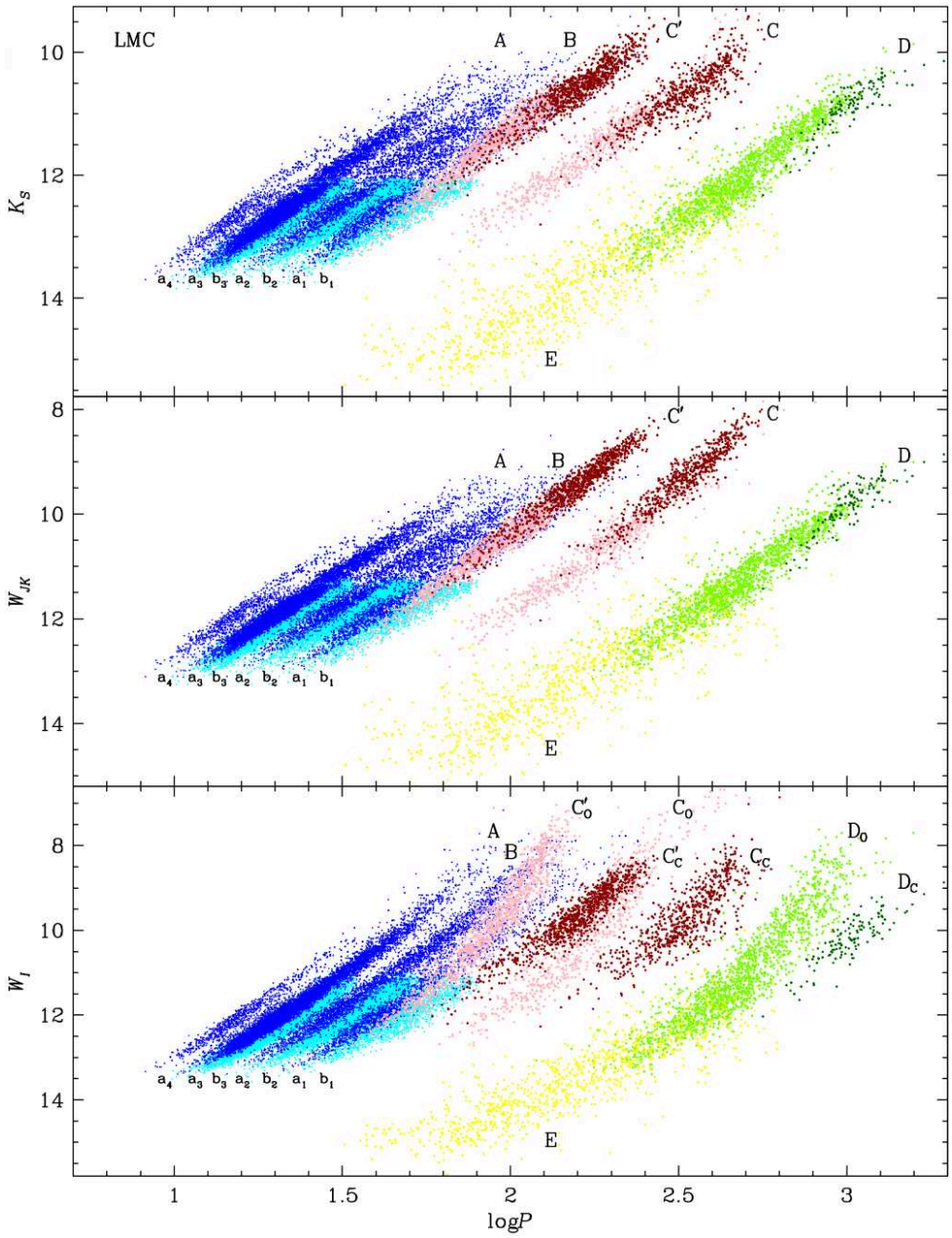

Figure 2.8: Period-Luminosity diagrams of LPVs in the LMC (reproduced from Soszyński et al. (2007)). Colours represent: OSARGs on the AGB or RGB (cyan and blue, respectively); O-rich (pink) or C-rich (red) Miras/SRVs; O-rich (light green) or C-rich (dark green) LSPs; and ellipsoidal red giants (yellow).

Chapter 3

Theory of Stellar Pulsation

In the present chapter we summarise the most important aspects of the theory of stellar pulsations. After recalling some fundamental aspects and equations of hydrodynamics in section 3.1, we discuss linear perturbation theory and its application to the description of oscillations in stars (section 3.2), both in the adiabatic and non-adiabatic cases.

The next sections are largely based on the discussions found in dedicated textbooks about stellar structure and stellar pulsations: Cox and Giuli (1968), Cox (1980), Aerts et al. (2010), and Catelan and Smith (2015). The discussion is aimed to provide a brief, general overview of the concepts and methods used throughout the next chapters. Therefore, most derivations are omitted, as well most aspects of the subject not directly linked with the topic of the present work. We refer the interested reader to the aforementioned textbooks for a more complete and detailed discussion.

3.1 Essential Hydrodynamics

Hydrodynamics represents the starting point for the theory of stellar structure and evolution as well as stellar oscillations. Before discussing the basic equations of hydrodynamics and their form in the case of stellar structure, it is important to recall the concepts of Eulerian and Lagrangian descriptions of a gas flow.

In the Eulerian description, physical properties of the gas (or, in general, of a fluid) are regarded as field quantities, being functions of time t and of a spatial position $\vec{r}$ with respect to a fixed frame of reference. Such a position is not associated with any particular fluid element (as in the Lagrangian formalism), but is rather a point of observation in space.

On the other hand, the Lagrangian description is employed when one is interested in following the motion of a particular fluid element, and studying how its properties vary as it moves about. From a mathematical point of view, such "changes of properties" along the motion are described by means of the so-called *Stokes derivative*[1]:

$$\frac{\mathrm{d}}{\mathrm{d}t} = \frac{\partial}{\partial t} + \vec{v} \cdot \nabla \,, \tag{3.1}$$

where ∇ is the usual gradient operator, the fluid velocity is defined as

$$\vec{v}(\vec{r}, t) = \frac{\mathrm{d}\vec{r}}{\mathrm{d}t} = \dot{\vec{r}}, \tag{3.2}$$

[1] Also called: material derivative, advective derivative, convective derivative, Lagrangian derivative, substantial derivative, total derivative, or simply derivative along the motion.

and $\partial/\partial t$ is the derivative taken at a fixed position in space, *i.e.*, the Eulerian derivative. Note that in the equations above $\vec{r}$ is not the Eulerian position (the "point of observation"), but rather the instantaneous position of the fluid element being followed. The main difference is that, as a Lagrangian variable, $\vec{r}$ is no longer and independent variable, but it is rather a function of time t, and of an additional parameter univocally identifying the fluid element. Usually, the additional parameter a is the position of the element itself at some time t_0, although a different identifying property can be used when convenient. For instance, in the case of stellar structure, the mass m_r contained within a radius r is often used as Lagrangian variable.

To summarise, in the Eulerian description t and $\vec{r}$ are both independent variables, while $\vec{r}$ is not an independent variable in the Lagrangian description. In that case, the independent variables are t and the parameter a. The Lagrangian description is especially useful in 1D problems, as it provides a more straightforward physical interpretation of the equations involved.

In the next sections we recall (without derivation) the basic equations of hydrodynamics, *i.e.*, the equations of conservation of mass, momentum and energy. We have already implicitly assumed that the gas can be treated as a continuum, so that its properties can be specified as functions of position $\vec{r}$ and time t. Moreover, it is assumed that the space is Euclidean, and that relativistic effects can be ignored (material velocities are always much smaller than the speed of light), so that mass is conserved and Newtonian gravitation can be employed.

3.1.1 Equations of Hydrodynamics

The first equation of hydrodynamics, the continuity equation, describes mass conservation. In the Eulerian description it is given by:

$$\frac{\partial \rho}{\partial t} + \nabla \cdot (\rho \vec{v}) = 0\,, \tag{3.3}$$

where ρ is mass density. The Lagrangian form can be obtained by applying the operator relation 3.1 to Eq. 3.3:

$$\frac{1}{\rho}\frac{\mathrm{d}\rho}{\mathrm{d}t} = -\nabla \cdot \vec{v}\,. \tag{3.4}$$

From the latter form, one can see that the meaning of the equation is that the fractional rate of variation of density (or specific volume, ρ) of a fluid element is equal to the divergence of the fluid velocity, $\nabla \cdot \vec{v}$, at that element position, *i.e.*, the tendency of the flow to converge towards, or move away from, that element.

For the equation of conservation of linear momentum, also known as the equation of motion, we assume that the gas viscosity can be neglected (a valid assumption for stellar interiors), that surface forces are due only to pure hydrostatic pressure P only, and that body forces are due to gravity alone. Thus, the equation of momentum conservation is:

$$\rho\frac{\mathrm{d}\vec{v}}{\mathrm{d}t} = -\nabla P + \rho\vec{g}\,, \tag{3.5}$$

where the gravitational acceleration $\vec{g} = -\nabla\Phi$ is the gradient of the gravitational potential Φ. In the static case ($\vec{v} = 0$) Eq. 3.5 reduces to the equation of hydrostatic equilibrium.

Conservation of energy is expressed by the first law of thermodynamics:

$$\frac{\mathrm{d}q}{\mathrm{d}t} = \frac{\mathrm{d}E}{\mathrm{d}t} + P\frac{\mathrm{d}}{\mathrm{d}t}\left(\frac{1}{\rho}\right), \tag{3.6}$$

where q is heat per unit mass and E is the internal energy per unit mass. Thus, Eq. 3.6 states that the net change of heat per unit mass in a given fluid element, along the motion, equals the sum of the change in its internal energy plus the work done to expand or compress the gas.

It is convenient to employ the alternative "astrophysical" forms of Eq. 3.6:

$$\frac{\mathrm{d}\ln P}{\mathrm{d}t} = \Gamma_1\frac{\mathrm{d}\ln\rho}{\mathrm{d}t} + \frac{\rho(\Gamma_3-1)}{P}\frac{\mathrm{d}q}{\mathrm{d}t}, \tag{3.7}$$

$$\frac{\mathrm{d}\ln T}{\mathrm{d}t} = (\Gamma_3-1)\frac{\mathrm{d}\ln\rho}{\mathrm{d}t} + \frac{1}{c_V T}\frac{\mathrm{d}q}{\mathrm{d}t}, \tag{3.8}$$

$$\frac{\mathrm{d}\ln T}{\mathrm{d}t} = \frac{\Gamma_2-1}{\Gamma_2}\frac{\mathrm{d}\ln P}{\mathrm{d}t} + \frac{1}{c_P T}\frac{\mathrm{d}q}{\mathrm{d}t}, \tag{3.9}$$

where c_V and c_P are the specific heats per unit mass at, respectively, constant volume and constant pressure, T is the gas temperature and the adiabatic exponents are defined as:

$$\Gamma_1 = \left(\frac{\mathrm{d}\ln P}{\mathrm{d}\ln\rho}\right)_{\mathrm{ad}}, \tag{3.10}$$

$$\Gamma_3 - 1 = \left(\frac{\mathrm{d}\ln T}{\mathrm{d}\ln\rho}\right)_{\mathrm{ad}}, \tag{3.11}$$

$$\frac{\Gamma_2-1}{\Gamma_2} = \left(\frac{\mathrm{d}\ln T}{\mathrm{d}\ln P}\right)_{\mathrm{ad}} = \nabla_{\mathrm{ad}}\,. \tag{3.12}$$

3.1.2 Heat Gains and Losses

In addition to the conservation equations, an equation is necessary to describe the net rate of gain of heat per unit mass. In general, the amount of heat gained/lost by a fluid element per unit mass is given by the difference between the heat gained by heat sources and the heat lost from sinks:

$$\frac{\mathrm{d}q}{\mathrm{d}t} = \varepsilon - \frac{1}{\rho}\nabla\cdot\vec{F}, \tag{3.13}$$

where ε is the total energy generation rate per unit mass (including nuclear reactions, gravitational contraction, etc.) and $\vec{F}$ is the energy flux associated to all energy transport mechanisms.

In astrophysical contexts, energy is mainly carried by radiation and convection, and possibly by conduction, as in the case of electron degeneracy. Formally, the latter can be treated in the same way as radiation and incorporated in the radiative flux equation. In the interior of stars, radiation can be treated by means of the diffusion approximation, and the radiative flux is given by:

$$\vec{F}_R = -\frac{4acT^3}{3\kappa_{\mathrm{R}}\rho}\nabla T, \tag{3.14}$$

where a is the radiation density constant, c is the speed of light and κ_{R} is the Rosseland mean opacity. Such an approximation is not valid in the outer stellar layers, where, in

principle, the full radiative transfer problem has to be solved. However, simplifications are often introduced (such as that of grey atmosphere) when there is no interest in having a detailed description of the outermost layers.

The description of convective energy transport is much more problematic, being actually one of the major open problems in theoretical astrophysics. Applications to pulsating stars, in particular, would require a time-dependent theory of convection, as the characteristic time scales associated to convection and pulsation can become similar. An appropriate theory to describe convection and the interaction between convection and pulsation that is simultaneously realistic and feasible for calculations of stellar structure and evolution is still missing. Usually, the some version of mixing length theory (Böhm-Vitense, 1958) is employed, possibly with some modification to include a time-dependent behaviour (see, *i.e.*, Fox and Wood (1982), and references therein, and section 4.3).

3.2 Linear Theory

The general equations describing the hydrodynamics of stellar structure are very complex, and it is generally impossible to obtain exact solutions of the complete system of non-linear, partial differential equations.

A great deal of simplification can be obtained by describing stellar oscillations as small perturbations from an equilibrium state, the so-called perturbation analysis or linear theory. Strictly speaking, this approach is only valid only when the oscillation amplitudes are small. However, it can be applied also to variable stars characterised by large surface amplitude, as in many cases most of the oscillation energy is confined in regions far enough from the surface, where the oscillation amplitudes are small.

The equilibrium state is described by the usual equations of stellar structure. In case of spherical symmetry, their Lagrangian form is given by:

$$\frac{\partial r}{\partial m} = \frac{1}{4\pi r^2 \rho}\,, \tag{3.15}$$

$$\frac{\partial P}{\partial m} = -\frac{Gm}{4\pi r^4}\,, \tag{3.16}$$

$$\frac{\partial L}{\partial m} = 4\pi \frac{\partial r^2 F}{\partial m} = \varepsilon\,, \tag{3.17}$$

$$\frac{\partial T}{\partial m} = -\frac{GmT}{4\pi r^4 P}\nabla\,, \tag{3.18}$$

where $L = 4\pi r^2 F$ is the total flow of energy through a sphere of radius r. The temperature gradient ∇ is determined via the diffusion approximation in radiative regions, and an appropriate convection theory (usually the mixing length theory) in convective regions. The equations above describe the equilibrium state in terms of the variables r, P, L, and T, that depend upon the spatial variable m but are independent of time t. As usual, those equations are to be accompanied by the "constitutive" equations describing energy generation, opacity and the state of matter (equation of state).

When small perturbations are introduced, the system variables can be written in the form:

$$X(r,t) = X_0(r) + X'(r,t)\,, \tag{3.19}$$

where the subscript 0 denotes the equilibrium value. The quantity $X'(r,t)$ is the Eulerian perturbation to the quantity X, and describes its difference with respect to the

equilibrium value at the position r, as a function of time. Again, if one wants to follow the evolution of a given fluid element, *i.e.*, a given mass layer, the Lagrangian form of the perturbation should be used. In that case, the perturbation causes a displacement δr of the chosen fluid element with respect to its equilibrium position:

$$\delta r = r - r_0 \,, \tag{3.20}$$

and the Lagrangian perturbation can be computed from the Eulerian one as

$$\delta X(r) = X'(r) + \delta r \frac{\partial X}{\partial r} \,. \tag{3.21}$$

The perturbed equations are obtained by introducing the expressions for the perturbed variables and keeping only terms that are at most linear in the perturbations.

The perturbed equations of mass and momentum conservations have the form (see Cox (1980) and Catelan and Smith (2015)):

$$\frac{\delta\rho}{\rho} = -3\zeta - 4\pi r^3 \rho \frac{\partial \zeta}{\partial m} \,, \tag{3.22}$$

$$\frac{\partial^2 \delta r}{\partial t^2} = \frac{4Gm}{r^2}\zeta - 4\pi r^2 \rho \frac{\partial \delta P}{\partial m} \,, \tag{3.23}$$

where the 0 subscript for the unperturbed values have been dropped, and $\zeta = \delta r/r$ is the relative displacement of the surface of a sphere containing interior mass m, r being its position in the unperturbed solution.

The meaning of the latter equation is the following. The first term means that, as a layer expands ($\zeta > 0$), it moves away from the center of the star, those feeling a weaker gravitational potential, which favors the expansion. Additionally, an exactly identical contribution is given from the fact that the surface area of the layer increases by a factor r^2, so that it feels a stronger outward force due to the pressure gradient. The second term gives the restoring force per unit mass, which results from the pressure perturbation δP associated to the displacement δr: as a layer expand (contracts), pressure decreases (increases), so that the layer will tend to reverse the expansion (contraction).

The perturbed energy equation can be obtained by Eq. 3.7:

$$\frac{\partial}{\partial t}\left(\frac{\delta P}{P}\right) = \Gamma_1 \frac{\partial}{\partial t}\left(\frac{\delta\rho}{\rho}\right) + \frac{\rho(\Gamma_3 - 1)}{P}\delta\left(\varepsilon - \frac{\partial L}{\partial m}\right) \,. \tag{3.24}$$

In regions where energy is carried by radiation alone, using the diffusion approximation the following expression can be obtained for the perturbed energy transport equation:

$$\frac{\delta L}{L} = 4\zeta + 4\frac{\delta T}{T} - \frac{\delta\kappa_{\rm R}}{\kappa_{\rm R}} + \left(\frac{\partial T}{\partial m}\right)^{-1} \frac{\partial}{\partial m}\left(\frac{\delta T}{T}\right) \,. \tag{3.25}$$

3.2.1 Linear Adiabatic Wave Equation

It is often useful to assume that individual mass elements of the star undergo no net exchange of heat during pulsation. This adiabatic approximation has the advantage of simplifying the problem of stellar pulsation from a mathematical point of view. Moreover, it is often a good approximation when the mechanical pulsation of the star

as a whole is considered. Indeed, non-adiabatic effects are often small, and a good description of the pulsation properties of the star can be obtained even when those effects are neglected. Of course, non-adiabatic layers are the very ones causing the star to pulsate, so that the adiabatic approximation comes at the price that the theory is unable to explain the origin of pulsation itself.

In the adiabatic approximation, the perturbed energy equation simply becomes:

$$\frac{\delta P}{P} = \Gamma_1 \frac{\delta \rho}{\rho} \,. \tag{3.26}$$

By replacing it in the perturbed equation of momentum conservation, and using the continuity equation to replace density perturbations with radial displacement perturbations, after some manipulation[2] one obtains:

$$r\frac{\partial^2 \zeta}{\partial t^2} = 4\pi r^2 \zeta \frac{\mathrm{d}}{\mathrm{d}m}\left[(3\Gamma_1 - 4)\, P\right] + \frac{1}{r}\frac{\partial}{\partial m}\left[16\pi r^2 \Gamma_1 P \rho r^6 \frac{\partial \zeta}{\partial m}\right] . \tag{3.27}$$

Eq. 3.27 is solved by separation of the variables, searching solutions of the form:

$$\zeta(r,t) = \xi(r) e^{i\omega t} \,, \tag{3.28}$$

where ξ describes the local displacement at a certain position r along the stellar radius, and the constant ω is the angular frequency of oscillation.

This results in the so-called the *Linear Adiabatic Wave Equation* (LAWE):

$$\frac{\mathrm{d}}{\mathrm{d}r}\left(\Gamma_1 P r^4 \frac{\mathrm{d}\xi}{\mathrm{d}r}\right) + \xi\left\{\omega^2 \rho r^4 + r^3 \frac{\mathrm{d}}{\mathrm{d}r}\left[(3\Gamma_1 - 4)\, P\right]\right\} = 0 \,. \tag{3.29}$$

The LAWE, or the corresponding system of differential equations, requires two boundary conditions to be solved. The first one is that the displacement δr vanishes at the centre of the star. The surface boundary condition is generally imposed either on the pressure perturbation or its gradient (see the discussion in section 4.3.2).

The LAWE corresponds to an eigenvalue problem, in particular it is of the Sturm-Liouville type, that has some well known properties. It has an infinite number of solutions, specified by the eigenvalues ω_n^2 and the corresponding eigenfunctions ξ_n. The eigenfrequencies ω_n^2 are always real, where the case $\omega_n^2 > 0$ corresponds to oscillatory behaviour, while $\omega_n^2 < 0$ corresponds to dynamical instability (explosion or collapse on a free-fall timescale).

The eigenvalue associate to radial order $n = 0$ is called fundamental mode. It corresponds to the lowest frequency (longest period). Moreover, eigenvalues are sorted, so that $\omega_n < \omega_{n+1}$ for $n \geq 0$. The eigenfunctions for modes with $\omega_n > 0$ all correspond to standing wave solutions, and have a number of nodes equal to n. Thus $\xi_n(r)$ describes the maximum amplitude of the perturbation at each position $0 \leq r \leq R$, and $\xi(R)$ is the pulsation amplitude at the surface of the star ($r = R$).

3.2.2 Non-Adiabatic Pulsations

The adiabatic theory comes with the advantage of providing a quite good approximation of the pulsational behaviour of real stars in the form of a relatively simple and

[2] See, *e.g.*, Cox and Giuli (1968).

mathematically convenient problem. Such a theory allows for the computation of the natural modes of oscillation of a stellar structure.

However, by neglecting the energetics involved in stellar pulsations, the adiabatic theory is unable to predict whether energy is fed into or removed from oscillatory motions, *i.e.*, whether the modes of oscillations are excited or damped. In other words, a non-adiabatic theory is necessary to determine whether a stellar structure *actually* pulsate.

When non-adiabatic effects are taken into account, the perturbed energy equation is in the form given by Eq. 3.24. Again, the perturbed equations can be combined (see, *e.g.*, Catelan and Smith (2015)) to obtain a single differential equation:

$$\frac{\partial^3\zeta}{\partial t^3} - \frac{1}{\rho t}\frac{\partial\zeta}{\partial t}\frac{\partial}{\partial r}\left[(3\Gamma_1 - 4)\,P\right] - \frac{1}{r^4\rho}\frac{\partial}{\partial r}\left[r^4\Gamma_1 P\frac{\partial}{\partial r}\left(\frac{\partial\zeta}{\partial t}\right)\right] + \\ + \frac{1}{\rho r}\frac{\partial}{\partial r}\left[\rho\,(\Gamma_3 - 1)\,\delta\left(\varepsilon - \frac{\partial L}{\partial m}\right)\right]. \tag{3.30}$$

Eq. 3.30 is also solved by separation of the variables, assuming the solutions to have the form given by Eq. 3.28. However, in the non-adiabatic case, the angular frequency is in general a complex number having both the real and imaginary parts different than zero,

$$\omega = \sigma + i\kappa\,. \tag{3.31}$$

Thus, solutions have the form:

$$\zeta(r,t) = \xi(r)e^{i\sigma t}e^{-\kappa t}\,, \tag{3.32}$$

where the term with κ represents an exponential increase/decrease of amplitude depending on the sign of κ. Therefore, the non-adiabatic term κ represents a stability coefficient. The situation where there is a net energy gain by oscillatory motions at each pulsation cycle corresponds to $\kappa < 0$, *i.e.*, amplitude grows with time (pulsational instability). On the other hand, when oscillatory motions undergo a net loss of energy at each pulsation cycle ($\kappa > 0$) amplitude decreases with time, to the point that it fades out (the oscillation is damped, or stable).

Energy is fed into pulsation when mechanical work is done my some mass layers on their surroundings, and thus it is converted to kinetic energy of pulsation. Not all mass layers of the star will contribute to maintain the pulsation. The ones that do positive work are the driving layers, while the ones that do a negative work, the damping layers, act towards pulsational stability.

It is useful to discuss this aspect by considering the equation of energy conservation, Eq. 3.7, at each mass layer of the star. In the adiabatic case, when a layer reaches maximum compression ($\partial\rho/\partial t = 0$), pressure is also at maximum. This is not the case for a layer that is exchanging energy with its surroundings. In fact, a layer that is gaining heat at maximum compression is also building up pressure, so that pressure will be higher during expansion than during compression. This is exactly the kind of behaviour required to maintain the pulsation.

Cox (1980) suggests a simplified but intuitive picture of pulsational stability in terms of all the infinitesimal mass layers dm of the star seen as independent Carnot-type heat engine, each one doing either a positive or negative work on the surrounding layers. The star is pulsationally stable if the sum (integral) of the work done by each layer during a pulsation cycle is negative, while the star is pulsationally unstable (undergoes pulsation of growing amplitude) if the total work is positive.

Chapter 4

Methodology

The major goal of the present work is to provide the community with an extended grid of new pulsation models, covering a wide range of stellar parameters for TP-AGB stars, including updated physical ingredients.

This will allow to fill the lack of updated models of long-periods variables, in particular of C-rich stars, that persisted in the last years.

The production of this grid allowed us to address the second major task of this work, which is to simulate the pulsation properties of any synthetic population of luminous red giant stars.

In particular, we used the grid to investigate pulsation properties of stars in the LMC.

4.1 Introduction

The construction of a grid of models involves a number of different codes, the management and combination of which requires the development of appropriate tools.

The present chapter is devoted to the description of the codes we used, and role played by each of them in the production of a grid of pulsation models.

We will discuss the methods employed to handle the computation of a large number of pulsation models, to assemble the results in an organised deliverable, and to integrate them in our population synthesis approach to be applied to the study of observed long-period variables.

The required ingredients are the following:

1. A stellar evolution code, to design the structure of the grid in terms of its parameters, their range and their sampling. Since we are interested in modelling the TP-AGB evolutionary phase, we used evolutionary tracks computed with the `COLIBRI` code (Marigo et al., 2013, 2017);

2. A code to integrate a stellar envelope model and to compute its stability analysis, providing periods and growth rates for several radial pulsation modes. In this work, we used the the linear, radial, non-adiabatic pulsation code described in Wood and Olivier (2014) and in Fox and Wood (1982).

3. An appropriate treatment of the opacity of stellar matter, consistent with the input chemistry, to be included in the computation of pulsation models. We use

the AESOPUS code (Marigo and Aringer, 2009) and the Opacity Project (OP) suite of programs described in Seaton (2005).

4. A population synthesis code. We used the code TRILEGAL (Girardi et al., 2005).

Note the fact that the grid is produced by performing stability analysis on envelope models that do not come from the stellar evolution code. This way, while taking input from the results of detailed evolutionary calculation, pulsation models are decoupled from stellar evolution models.

A major advantage of this approach is that our pulsation models are not restricted to the stellar evolution and synthetic population codes used here. In fact, the grid was designed to be as general and flexible as possible, and can be applied to estimate pulsation properties for any reasonable combination of red giant stellar parameters, regardless of their origin.

We begin by describing the main features of the TP-AGB stellar evolution code in section 4.2.

The pulsation code is discussed in section 4.3, focusing on the physical assumption, general solution methods, and the input/output involved in the computation. The envelope integration and stability analysis phases are discussed separately.

Section 4.3 also includes the description of the basic method employed in the computation of multiple pulsation models, a crucial step in the production of the grid.

The codes and data used to include updated opacities in pulsation models are discussed in section 4.6. Two libraries of opacity tables, produced to assist the computation of pulsation models, are also discussed.

In section 4.7 we provide an overview of the population synthesis code we employed in combination with the grid.

Finally, the structure and properties of the grid of pulsation models are presented in section 4.8

4.2 Stellar Evolution Models

The theoretical modelling of stellar evolution is generally based on codes that solve the time-dependent equations of stellar structure in spherical symmetry. When applied to the calculation of TP-AGB evolution, this approach turned out to meet a number of fundamental difficulties. Such difficulties include numerical uncertainties and instabilities, and the fact that, ultimately, some parametric description of crucial, uncertain processes (mass-loss, convection, overshoot) is necessary and often largely different from study to study.

In a situation where such "full models" struggle to converge towards a unified description of the TP-AGB, "synthetic models" have been developed in which the evolution from one thermal pulse to the next is described by analytical relations that synthesize the result from full models.

Synthetic models provide a valuable asset to complement full models, as they are very agile and suitable to explore wide ranges of parameters and prescriptions, thus helping to constrain the physical domain the physical domain towards which full models should converge in order to reproduce observed properties of TP-AGB stars.

The downside of pure synthetic models stems from the lack of accurate physics and the fact that they are essentially subordinate to the relations obtained by full models, a severe limitation to their capability of exploring new evolutionary effects.

An appropriate compromise is represented by hybrid models, in which accurate physics is employed to describe well known processes, while the most uncertain and least understood ones are treated by means of a parameterised approach.

An example of this combination is `COLIBRI`, a code for the calculation of stellar evolution during the thermally pulsing asymptotic giant branch (TP-AGB) phase from the first thermal pulse up to the complete ejection of the stellar mantle by stellar winds.

We summarise here the relevant features of the code, and refer to Marigo et al. (2013) and Marigo et al. (2017) for a more detailed discussion.

In `COLIBRI`, a detailed physical treatment of the envelope is combined with a parametrisation of the processes subject to large theoretical uncertainties, such as mass loss and convection. This approach maintains a firm physical basis while it is flexible and fast enough to rapidly produce complete grids of stellar evolutionary models, a necessary requirement for the calibration of the main uncertainties in the parameters and processes characterising the TP-AGB.

The stellar envelope is computed by integrating the equations of stellar structure from the atmosphere down to the bottom of the H-burning shell.

The occurrence of third dredge-up events can significantly change the surface chemical abundances, thus affecting subsequent evolution. To account for this, both the equation of state and the Rosseland mean opacity are computed on the fly for the specific chemical composition of the envelope, including about about 800 atomic, ionic and molecular species (the `AESOPUS` and `OP` codes are used, see also section 4.6).

This allows to describe self-consistently the stellar effective temperature, as well as the entire structure of the envelope, including the atmosphere and the conditions under which it may be significantly affected by sphericity effects.

Nucleosynthesis is described by solving a complete nuclear network that includes the pp chains and the CNO, NeNa and MgAl cycles, coupled with a description of diffusive mixing. Energy generation is thus properly accounted for, both in the H-burning shell and in the deepest region of the convective envelope, *i.e.*, hot-bottom burning (HBB). The nuclear network is also solved in a simple model of the pulse-driven convection zone in order to predict the intershell abundances left by each thermal pulse.

The core mass–luminosity relation, as well as its break down due to the occurrence of HBB, are thus also describe self-consistently

The onset and quenching of the third dredge-up is determined based on a temperature criterion applied to the result of envelope integrations at the stage of the post-flash luminosity peak of each thermal pulse.

The third dredge-up is parametrised in terms two characteristic quantities: (1) the minimum core mass $M_{\rm c}^{\rm min}$ for the onset of the third-dredge up, and (2) the efficiency λ of the third dredge-up, defined as the fraction of the core-mass growth over the interpulse period that is dredged-up to the surface at the next thermal pulse.

Fig. 2.3 shows a comparison of the value of λ obtained from *full* AGB calculations by different authors, for the same stellar model of initial mass $M_i = 3.0\,{\rm M}_\odot$ and initial metallicity $Z_i = 0.02$. The large differences from author to author represent a rather clear example of the theoretical uncertainties relative to the TP-AGB, and the need for a consistent calibration of that evolutionary phase.

Typical predictions from the code are displayed in Fig. 4.1, showing the whole TP-AGB evolution of a model of initial mass $M_i = 5\,{\rm M}_\odot$ and initial metallicity $Z = 0.008$, representative of the most luminous M-type giants in the Large Magellanic Cloud. The model experiences 48 thermal pulse cycles, evident in the fluctuations of photospheric

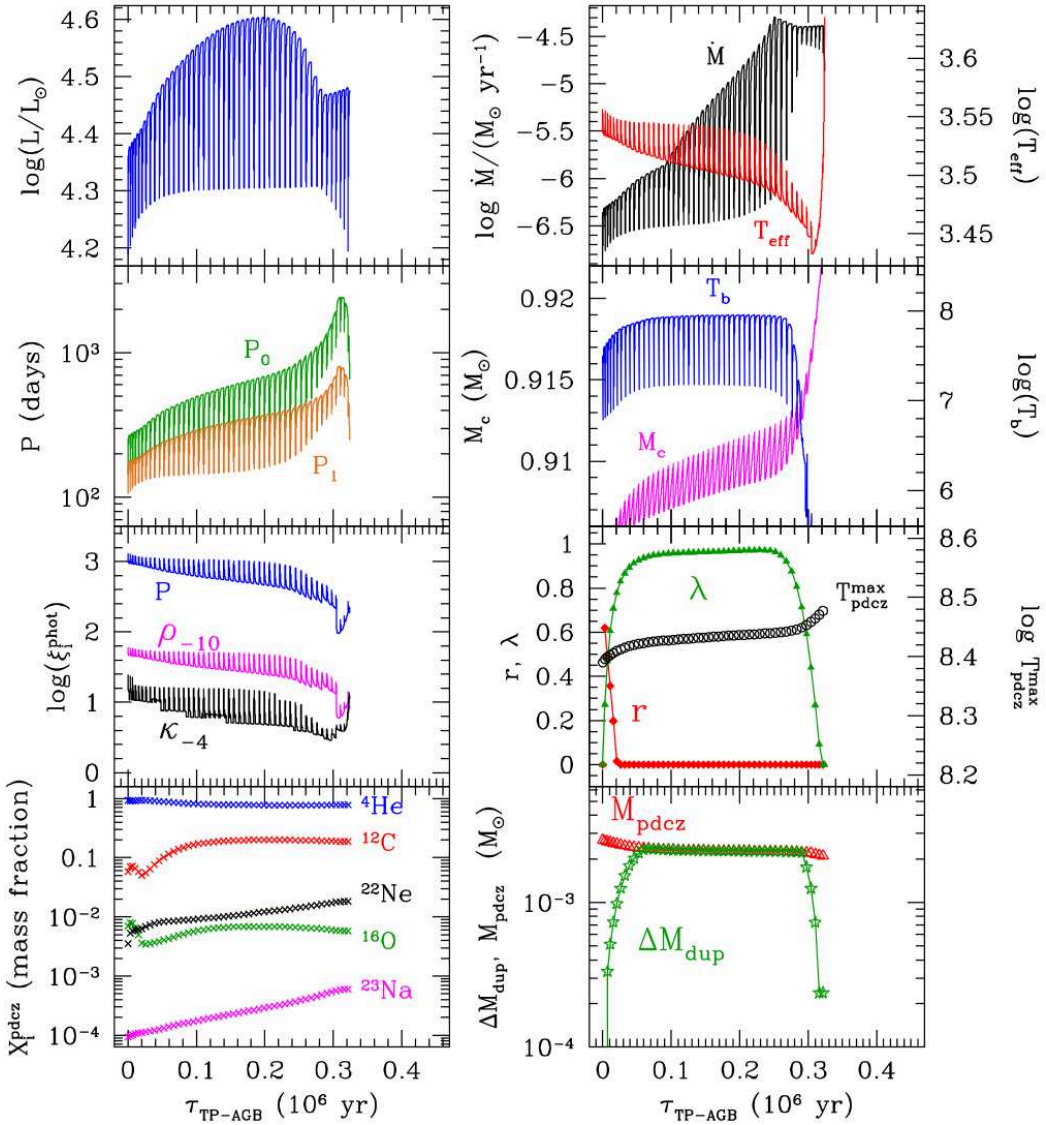

Figure 4.1: Sample output provided by the COLIBRI code. The evolution of several quantities, over the whole TP-AGB phase, is shown for an model of initial mass and metallicity $M_i = 5\,\mathrm{M}_\odot$ and $Z_i = 0.008$, representative of the most luminous M-giant stars in the LMC. From top left to bottom right, the eight panels show the evolution of (1) surface luminosity L; (2) mass-loss rate $\dot{M}$ and effective temperature $T_{\rm eff}$; (3) fundamental and first overtone pulsation periods P_0, P_1; (4) core mass $M_{\rm c}$ and temperature at the base of the convective envelope $T_{\rm bce}$; (5) photospheric values of pressure P, density $\rho_{-10} = \rho/(10^{-10}\mathrm{g\,cm^{-3}})$ and Rosseland mean opacity $\kappa_{-4} = \kappa/10^{-4}$; (6) efficiency λ of the third dredge-up, maximum temperature $T^{\rm max}_{\rm pdcz}$ at the bottom of the pulse-driven convection zone and the degree of overlap r between consecutive zones; (7) intershell abundances of ^{4}He, ^{12}C, ^{16}O, ^{22}Ne, and ^{23}Na; (8) mass of the pulse-driven convective zone $\Delta M_{\rm pdcz}$ and dredged-up mass $M_{\rm Dup}$ at each thermal pulse (reproduced from Marigo et al. (2013))

quantities and global parameters of the envelope.

Of the displayed quantities, the ones predicted by numerical integration of the en-

velope and/or the solution of the nuclear network are the surface luminosity L, the effective temperature $T_{\rm eff}$, the core mass $M_{\rm c}$, the temperature at the base of the convective envelope $T_{\rm bce}$, the photospheric values of pressure P, density ρ and Rosseland mean opacity κ, the intershell abundances and the degree of overlap r between the pulse-driven convection zones of two consecutive thermal pulses.

On the other hand, the mass-loss rate $\dot{M}$, the pulsation periods of the fundamental and first overtone modes, P_0 and P_1, and the third dredge-up parameters (efficiency λ, dredged-up mass $M_{\rm Dup}$, mass of the pulse-driven convection zone $\Delta M_{\rm pdcz}$, and maximum temperature at the bottom of the pulse-driven convection zone $T_{\rm pdcz}^{\rm max}$) are obtained by means of parametrised descriptions.

In the version of the code described in Marigo and Girardi (2007), the pulsation periods P_0 and P_1 were included using the period-mass-radius (PMR) relations by Wood et al. (1983a) for the first overtone mode and those by Groenewegen and de Jong (1994) and Fox and Wood (1982) for the fundamental mode, whereas a relation derived from models by Ostlie and Cox (1986) was used to describe the luminosity at which the dominant pulsation modes shifts from the first overtone to the fundamental mode as a function of stellar mass and effective temperature.

Since all of those models are strictly valid only for O-rich compositions, pulsation in C-rich star was treated by using a fictitious radius in the PMR relations, *i.e.*, the radius corresponding to the effective temperature of an O-rich model at the same luminosity.

Such relations are intended to be replaced by a more detailed description, including proper models of carbon stars, by using the pulsation models computed as part of this work. A preliminary attempt to this revision was made in Marigo et al. (2017), different PMR relations are implemented to describe separately the pulsation of O-rich and C-rich stars in the fundamental and first overtone modes (see also section [ref]).

4.3 The Stellar Pulsation Code

The stellar pulsation code we used is described in Wood and Olivier (2014), based on the one presented in Fox and Wood (1982). The present section is divided in two parts, following the two steps of the computation of a pulsation model: (1) the integration of the structure of a stellar envelope (an envelope model), and (2) the calculation of the oscillation eigenmodes of that structure (a stability model). The envelope model represent the equilibrium state of the star.

4.3.1 Computation of an Envelope Model

General Description and Assumptions

In the computation of the equilibrium model, the star is assumed to be spherically symmetric. Rotation and magnetic fields are ignored.

As discussed in section 2.1.2, the structure of an AGB star consist of a compact CO core surrounded by an extended envelope, through which energy is mainly carried by convective motions. The star is supported by nuclear reactions taking places in a thin shell between the core and the envelope. During most of the TP-AGB evolution, the hydrogen-burning shell is active, while the helium-burning shell is dormant. Such so-called "quiescent" phases alternate to episodes of rapid ignition of the He-burning shell (thermal pulses, or He-shell flashes), during which the H-burning shell is temporarily extinguished.

From a dynamical point of view, the core and the envelope are effectively decoupled. This means that stellar pulsation is essentially an envelope phenomenon, allowing for a great degree of simplification in its modelling. Therefore, it is possible to restrict the computation of a stellar structure model to the envelope alone. Reasonable assumptions are made on the global properties of the core (its mass M_c and radius R_c), that are used as inner boundary conditions, *i.e.*, as input parameters. Note that, anyway, the envelope makes up for the large majority of the stellar volume, although the core amounts to a significant fraction of the total mass M of the star.

For the same reasons, the nuclear shell can also be excluded from the computation of the stellar structure. Thus, in general, when speaking of the "core" we will mean both the actual CO core and the nuclear shell on top of it. The entire stellar luminosity L is assumed to be generate in the core. This way, the luminosity is also an input parameter used as boundary condition. As discussed in sections 2.1.2 and 4.2, its value is connected to the core mass.

An appropriate value has to be chosen for the core radius R_c, consistent with the assumption made that the nuclear shell is included in the core. In the present work, we use a fixed value $R_c = 0.15\,R_\odot$ for all envelope models. This value is large enough to include the shell (at least during quiescent evolution), and small enough to guarantee that the envelope is computed essentially in its entire radial extent. This is clearly a rough approximation, but has a very small impact on the resulting structure, as well as on its pulsation properties. We tested this by comparing such results with those obtained with a more realistic assumption, *i.e.*, a mass-radius relation valid for white dwarfs.

With the above assumptions, the equations of hydrostatic stellar structure can be written as:

$$\frac{\mathrm{d}r}{\mathrm{d}m} = \frac{1}{4\pi r^2 \rho}\,, \tag{4.1}$$

$$\frac{\mathrm{d}P}{\mathrm{d}m} = -\frac{Gm}{4\pi r^4}\,, \tag{4.2}$$

$$L(m) = L = \text{constant}\,, \tag{4.3}$$

$$\frac{\mathrm{d}T}{\mathrm{d}m} = -\frac{GmT}{4\pi r^4 P}\nabla\,, \tag{4.4}$$

where m (the independent variable) is the mass contained within a sphere of radius r, P is pressure, T is temperature, L is luminosity, ρ is density, $\nabla = \mathrm{d}\ln T/\mathrm{d}\ln P$ is the local temperature gradient and G is the constant of gravitation. Equations 4.1, 4.2 and 4.3 correspond to the conservation of mass, momentum and energy, respectively.

In radiative regions, the value of the temperature gradient ∇ in the energy transport equation (Eq. 4.4) is computed using the diffusion approximation:

$$\nabla = \nabla_{\mathrm{rad}} = \frac{3}{64\pi\sigma_{\mathrm{B}}}\frac{P\kappa_{\mathrm{R}}}{T^4}\frac{L}{Gm}\,, \tag{4.5}$$

where σ_{B} is the Boltzmann constant and κ_{R} is a Rosseland mean opacity, that is supplied through suitable tables as a function of temperature and density (see sections 4.6 and [ref]), including conductive opacities.

In convective regions (where $\nabla_{\mathrm{rad}} > \nabla_{\mathrm{ad}}$, according to the Schwarzschild criterion) ∇ is computed by means of the usual mixing length theory[1] (Böhm-Vitense, 1958).

[1] The modified mixing length theory by Arnett et al. (2010) is also implemented in both the envelope and the pulsation codes (Wood and Arnett, 2011), but it was not employed in the present work.

The mixing length ML is described in terms of the mixing length parameter $\alpha_{\rm MLT} = {\rm ML}/H_P$, where $H_P = ({\rm d}\log P/{\rm d}r)$ is the local pressure scale height.

Equations 4.1, 4.2, 4.3, 4.4 and 4.5 can be rewritten as:

$$\begin{aligned}
{\rm d}r^3 &= \frac{3}{4\pi\rho}{\rm d}m\,, &(4.6)\\
{\rm d}P &= -\frac{Gm}{4\pi r^4}{\rm d}m\,, &(4.7)\\
L(m) &= L\,, &(4.8)\\
({\rm d}\ln T)_{\rm rad} &= -\frac{3}{256\pi^2\sigma_{\rm B}}\frac{L}{r^4}\frac{\kappa_{\rm R}}{T^4}f{\rm d}m\,, &(4.9)\\
({\rm d}\ln T)_{\rm conv} &= -\frac{Gm\nabla}{4\pi r^4 P}{\rm d}m\,, &(4.10)
\end{aligned}$$

where Eq. 4.9 is used for the radiative regions and Eq. 4.10 is used in the convective ones. The factor f in Eq. 4.9 is introduced as an attempt to approximate sphericity and deviations from the diffusion approximation in the outer layers, where the optical depth τ is small, and is given by (see Fox and Wood, 1982, their Appendix I, for more details):

$$f = 1 + \left(0.357 + \frac{1.173}{\kappa_{\rm R}\rho r}\right){\rm e}^{-2.54\tau}\,. \qquad (4.11)$$

The system above is thus expressed in difference form. The star is divided into N zones, with boundaries at mesh points $j = 1$, ..., $N+1$. The point $j = 1$, *i.e.*, the inner boundary, corresponds to the edge of the core (including the hydrogen shell) at $r = R_{\rm c}$. The outermost point, $j = N+1$, corresponds to the surface of the model, where $m = M$. This point is not to be confused with the photosphere, where $T = T_{\rm eff}$ (*i.e.*, $L = 4\pi\sigma_{\rm B}r^2T^4$) and $\tau \sim 1$. In fact, models are generally computed so to include the atmosphere of the star, that can be significantly extended.

The difference forms of Equations 4.6, 4.7, 4.8, 4.9 and 4.10 are:

$$\begin{aligned}
r_{j+1}^3 - r_j^3 &= \frac{3}{4\pi\rho_{j+1/2}}\Delta m_{j+1/2}\,, &(4.12)\\
P_{j+3/2} - P_{j+1/2} &= -\frac{Gm_{j+1}}{4\pi r_{j+1}^4}\Delta m_{j+1}\,, &(4.13)\\
L_j &= L\,, &(4.14)\\
\ln T_{j+3/2} - \ln T_{j+1/2} &= -\frac{3}{256\pi^2\sigma_{\rm B}}\frac{L_{j+1}}{r_{j+1}^4}\left\langle\frac{\kappa_{\rm R}}{T^4}\right\rangle_{j+1}f\Delta m_{j+1}\,, &(4.15)\\
\ln T_{j+3/2} - \ln T_{j+1/2} &= -\frac{Gm_{j+1}\nabla_{j+1}}{4\pi r_{j+1}^4(P_{j+1/2}P_{j+3/2})^{1/2}}\Delta m_{j+1}\,. &(4.16)\\
& &(4.17)
\end{aligned}$$

Equations 4.15 and 4.16 are used in radiative and convective regions, respectively. Integer or half-integer indices highlight the fact that some variables (r, $L(r)$, m) are defined at zone boundaries, while thermodynamic quantities (T, P, ρ) are defined at zone centers. The mass increments are defined as $\Delta m_{j+1/2} = m_{j+1} - m_j$ and $\Delta m_{j+1} = (m_{j+2} - m_j)/2$, while the approximation by Stellingwerf (1975) is used for $\langle\kappa_{\rm R}/T^4\rangle$.

Two outer boundary conditions are applied: $T_{\rm eff}$ has a value defined by the user, and a requirement is set on the surface pressure. Fox and Wood (1982) impose that

$P_{\rm gas} = 0$ at the surface ($r_{N+1} = R$). Since pressure P is not defined at zone boundaries, the latter condition is applied in the form:

$$P_{N+1/2} = P_{N+1}(\text{rad}) + \frac{1}{2}\Delta m_{N+1/2}\frac{GM}{4\pi R^4}\,, \tag{4.18}$$

where

$$R^3 - r_N^3 = \frac{3}{4\pi\rho_{N+1/2}}\Delta M_{N+1/2}\,. \tag{4.19}$$

However, in the present work we used an alternative boundary condition, discussed in Wood and Olivier (2014). Instead of setting the gas pressure to zero at the surface ($j = N + 1$), the condition used is:

$$P_{N+1}(\text{gas}) = \alpha \cdot P_{N+1/2}(\text{gas})\,, \tag{4.20}$$

with the arbitrary choice $\alpha = 0.9$, so that there is a significant gas pressure at the surface, but the change across the surface zone is not too large. Additionally, it is required that the optical depth from the surface to the centre of the outermost zone (from $j = N + 1$ to $j = N + 1/2$) has some user-defined value.

The above system of difference equations is integrated inwards, starting from a certain user-defined optical depth (in the present work the value $\log(\tau_0) = -4$ was used). The value of mass at $j = 1$ ($r = R_{\rm c}$) defines the core mass. In Fox and Wood (1982), the required core mass was obtained by adjusting the value of the mixing length parameter. In the present work, on the other hand, we use a slightly different approach. Since we are not interested in obtaining a specific value of the effective temperature, we iterate the integration by changing the input $T_{\rm eff}$ by a small amount, until the required core mass $M_{\rm c}$ is obtained, while $\alpha_{\rm MLT}$ is unchanged. Iterations are stopped when the difference between the input core mass and the resulting one is smaller than 0.5% of the total mass. Therefore, in a way, the boundary condition is that $m = M_{\rm c}$ at $j = 1$, while the input value of the $T_{\rm eff}$ is rather a first guess, while the effective temperature of the final model, determined by the iteration process, is to be regarded as an output parameter.

Input and Output

The input parameters to the envelope integration code are essentially global properties that define the star to modelled.

The user has to provide values of:

- the total stellar mass, M;
- the mass and radius of the core, $M_{\rm c}$ and $R_{\rm c}$;
- the total bolometric luminosity of the star, L;
- the chemical composition, defined by the mass fractions of hydrogen (X), helium (Y), carbon ($X_{\rm C}$), nitrogen ($X_{\rm N}$) and oxygen ($X_{\rm O}$), as well as the star's metallicity (Z);
- the optical depth τ_0 at the surface of the model;
- the first guess value of the effective temperature, $T_{\rm eff,0}$;

- the mixing length parameter, $\alpha_{\rm MLT}$;

As discussed above, we kept the core radius fixed at $R_{\rm c} = 0.15\,{\rm R}_{\odot}$ for all models, as well as the optical depth at the surface ($\tau_0 = 10^{-4}$).

It is clear that the first guess effective temperature does not affect the properties of the resulting models. It may, however, affect the convergence of the code. In fact, picking value that is too far from the actual effective temperature of the model can cause the code to run a large number of iterations, and thus slow down, or even not to converge at all. For this reason, it is necessary to set the first guess $T_{\rm eff}$ to a value that, given all other physical input (M, L, chemistry), is realistic from the point of view of stellar physics. As discussed in section [ref], to this aim a fitting relation was derived from evolutionary tracks to describe the effective temperature of AGB stars as a function of their mass, luminosity and metallicity.

The remaining parameters are those that really define the properties of the resulting envelope model, and thus of the corresponding pulsation model. It is by varying each of those parameters, independently on the others, on an appropriate range that the grid of pulsation models was constructed, as will be discussed in section [ref]. In brief, a number of values (or nodes) was selected for each parameter, and a pulsation model was computed for all (physically realistic) combinations of values of each parameter. By varying the mixing length parameter as well, models with different effective temperatures were obtained. Something slightly different was done for the case of the core mass. Since it cannot be assumed to be independent on luminosity, instead of using fixed values at the grid nodes, we computed the values at the nodes with different functions of luminosity, as explained in more detail in section [ref]. This way, each model was computed with different value of the core mass that are realistic for its luminosity.

The output data, besides those that are the same as the input parameters (M, L, $M_{\rm c}$, and the chemical composition) are the true effective temperature $T_{\rm eff}$ and the stellar radius. Moreover, the structure of the model is also output, in the form of the local values of r, m, T, and P at each mesh point, as well as an information on whether the corresponding zone is convective or radiative.

4.3.2 Computation of a Stability Model

General Description and Assumptions

The calculation of the pulsation modes of a given envelope structure is done by solving the equations of linear, non-adiabatic, radial oscillations, that are obtained by taking linear perturbations of the equations of stellar structure. The oscillation equations form a linear system of differential equations in the independent perturbation variables δL, $\delta \ln T$, δr, and $\delta \ln P$. The determinant of the system is a function of the complex frequency ω. Note that, in the formalism we used, a time dependence $\exp(\omega t)$ is assumed for the perturbations, instead of the form $\exp(\mathrm{i}\omega t)$ which is also commonly employed. The eigenvalues of the system, *i.e.*, the frequencies of the oscillation modes, can be computed by finding the values of ω for which the determinant of the system is zero.

The perturbed equations of continuity, momentum conservation and energy conser-

vation are:

$$\frac{\mathrm{d}\delta r}{\mathrm{d}m} = -\frac{1}{4\pi r^2\rho}\left(\frac{\delta\rho}{\rho}+3\frac{\delta r}{r}\right), \tag{4.21}$$

$$\frac{\mathrm{d}\delta P}{\mathrm{d}m} = \frac{\delta r}{4\pi r^2}\left(\frac{4Gm}{r^3}-\omega^2\right), \tag{4.22}$$

$$\frac{\mathrm{d}\delta L}{\mathrm{d}m} = -\omega\left(\delta U-\frac{P}{\rho^2}\delta\rho\right), \tag{4.23}$$

where U is the internal energy per unit mass, and δU the corresponding perturbation. An acceleration term has been added to the momentum conservation equation corresponding to hydrostatic equilibrium, while the energy conservation equation, Eq. 4.3, was replaced with the usual form, assuming that no nuclear energy generation takes place in the envelope and neglecting any energy loss due to neutrinos.

The treatment of time-dependent convection, used for the perturbation of convective energy transport, is schematically as follows. Convective velocity is assumed to vary on a time scale $\tau_v = \mathrm{ML}/(4v)$ (based on the formalism of Arnett (1969)), where ML is the local mixing length and v is the local convective velocity in the equilibrium model. It is assumed that convective velocity in the steady state is given by:

$$\dot{v} = \frac{\dot{v}_0}{1+\omega\tau_v}, \tag{4.24}$$

where $\dot{v}$ and $\dot{v}_0$ are, respectively, the actual rate of change of convective velocity and the rate of change it would had if convective velocity adjusted instantaneously to the local physical conditions.

The difference forms of the perturbed equations (Eq.4.21, 4.22 and 4.23) are:

$$\delta r_{j+1}-\delta r_j = -\tfrac{1}{4\pi r^2\rho}\left(\tfrac{\delta\rho_{j+1/2}}{\rho_{j+1/2}}-3\tfrac{\delta r_j}{r_j}\right), \tag{4.25}$$

$$\delta P_{j+3/2}-\delta P_{j+1/2} = \tfrac{\delta r_{j+1}}{4\pi r_{j+1}^2}\left(\tfrac{4Gm_{j+1}}{r_{j+1}^3}-\omega^2\right)\Delta m_{j+1}, \tag{4.26}$$

$$\delta L_{j+1}-\delta L_j = -\omega\left(\delta U_{j+1/2}-\tfrac{P_{j+1/2}}{\rho_{j+1/2}^2}\delta\rho_{j+1/2}\right)\Delta m_{j+1/2}, \tag{4.27}$$

The inner boundary conditions are applied by requiring that $\delta L_j = 0$ and $\delta r_j = 0$ at $j = 1$. Two additional boundary conditions are imposed at the surface of the model. The first one is that, at optical depth $\tau = 0$, the temperature satisfies the equation for a plane-parallel gray atmosphere:

$$T^4 = \frac{3L}{16\pi\sigma_{\mathrm{B}}r^2}\left[\tau+q(\tau)\right], \tag{4.28}$$

where the approximation by Böhm-Vitense (1958) is used for the function

$$q(\tau) = 0.727-0.1406\mathrm{e}^{-2.54\tau}. \tag{4.29}$$

A simple choice for the other boundary condition is to add an acceleration term to Eq. 4.18,:

$$\delta P_{N+1}(\mathrm{rad})-\delta P_{N+1/2} = \frac{\delta R}{4\pi R^2}\left(\frac{4GM}{R^3}-\omega^2\right)\frac{\Delta m_{N+1/2}}{2}. \tag{4.30}$$

However, gas pressure at the surface of the static models is not zero and it varies as the stellar surface oscillates, which has to be taken into account. Thus, we employed here another boundary condition, as described in Wood and Olivier (2014), based on the approach of Baker and Kippenhahn (1965). The region above the surface of the star that can influence the interior pulsation is assumed to be effectively isothermal and small with respect of the total stellar radius, so that the pressure scale height H_P is constant, as well as the quantity $h = H_P/r \simeq H_P/R$. The radius and pressure perturbations in that region are given by:

$$\delta r = x\mathrm{e}^{\mathbf{i}\omega t}\,, \qquad \delta P = p\mathrm{e}^{\mathbf{i}\omega t}\,, \tag{4.31}$$

and with the assumptions above one finds that $x \propto \exp(\nu r/R)$, where

$$\nu = \frac{1}{2h}\left\{(1-4h) - \left[(1-4h)^2 - 4h\left(\frac{4+3\sigma^2}{\gamma} - 3\right)\right]^{1/2}\right\}. \tag{4.32}$$

The quantity σ is the dimensionless oscillation frequency of a given mode, *i.e.*, it is normalised to the dynamical frequency of the star:

$$\sigma = \frac{\omega_{\mathrm{Im}}}{\omega_{\mathrm{dyn}}} = \frac{\omega_{\mathrm{Im}}}{(3GM/R^3)^{1/2}}\,. \tag{4.33}$$

For the pressure perturbation, one has then $p = -\gamma(\nu+3)x$. We set $\gamma = 1$, corresponding to isothermal oscillations in the outer layers.

The mechanical outer boundary condition given by 4.33 allows us to account for the fact that the frequencies of the higher overtone modes can approach or exceed the value corresponding to the acoustic cut-off frequency at the atmosphere (see, *i.e.*, Aerts et al., 2010, their Appendix D). In that case, pulsation energy is dissipated via running waves escaping through the atmosphere, and the corresponding mode is stabilised. Running waves correspond to solutions oscillating solutions for which the expression in square brackets in Eq. 4.32 is negative, making ν a complex number.

The difference equations 4.25, 4.26, 4.27, and the perturbed transport equationare discretised over $N-1$ mesh points, corresponding to $4(N-1)$ difference equations. Together with the four boundary conditions, they amount to a total of $4N$ independent linear equations in the $4N$ independent perturbation variables (δL_j, δr_j, $\delta \ln T_j$, $\delta \ln P_j$). These equations yield a determinant $D = D(\omega)$ which eigenvalues ω_n are the complex frequencies of all possible oscillation modes of the envelope structure in account. In order to find them, we exploit the fact that $D(\omega_n) = 0$ if ω_n is an eigenvalue.

In order to compute the non-adiabatic eigenvalues, the adiabatic problem is solved first. In that case, the perturbed energy equation becomes:

$$\frac{\delta P}{P} = \Gamma_1 \frac{\delta \rho}{\rho}\,. \tag{4.34}$$

The eigenvalues of adiabatic oscillations are purely imaginary (with the time dependence assumed here for the perturbations), and can be determined by evaluating the determinant along the imaginary axis until it changes sign. A secant method is then used to determine the exact eigenvalue.

We are interested in computing the frequencies of the N_{modes} lowest order pulsation modes, *i.e.*, the fundamental mode and the overtone modes up to the $(N_{\mathrm{modes}}-1)$-th one. Modes are identified by their radial order n: the fundamental mode has $n = 0$,

the first overtone mode (1O) has $n = 1$, the second overtone mode (2O) has $n = 2$, and so on. In the adiabatic case the eigenvalues are sorted, with the fundamental mode corresponding to the smallest frequency (longest period). In order to be sure to find the fundamental eigenvalue, one has to start to scan the imaginary axis from a small enough value of frequency. This starting value is an input parameter (see next section) that has to be set with care since we want to compute models of Long-Period Variables, for which the frequency of the fundamental mode can be especially small (of order of a few 10^{-9} Hz).

Once all $N_{\rm modes}$ adiabatic eigenvalues have been found, they can be used as starting point for the search of the non-adiabatic ones. For each mode, a region in the complex frequency plane is explored around the position of the adiabatic eigenvalue, looking for changes in the sign of the determinant (of the non-adiabatic system). This is done using a method similar to the one described by Dennis (1971).

More precisely, the search for each eigenvalue is performed the following way. Say the adiabatic eigenvalue is already known, and has a frequency (purely imaginary) $\omega_{{\rm ad},n}$. We use this value to define an alternative coordinate system in the complex frequency plane, so that we have the quantities $\omega_{\rm Re}/\omega_{{\rm ad},n}$ on the x-axis and $\omega_{\rm Im}/\omega_{{\rm ad},n} - 1$ on the y-axis. This way, the already known adiabatic eigenvalue is located in the origin, and the space around it is measured in units of its frequency.

Now, say we have some approximate knowledge of the expected value of the corresponding non-adiabatic eigenmode, that we call $\omega_{n,{\rm approx}}$. We define a rectangular grid around its position in the alternative frequency plane (see Fig. [ref]). The grid cells have size F_R and F_I along the real and imaginary axes, respectively. The size of the grid is defined by the number of cells along each axes. More precisely, since the grid is not expected to be centred on the origin, its width (*i.e.*, the size along the real axis) is given by

$$L_R = L_R^- + L_R^+ = N_R^- F_R + N_R^+ F_R = \left(N_R^- + N_R^+\right) F_R \,, \tag{4.35}$$

where N_R^- and N_R^+ are the number of cells on the negative and positive sides of the adiabatic eigenvalue, respectively. Similarly, the grid's height (*i.e.*, its size along the imaginary axis) is given by

$$L_I = L_I^- + L_I^+ = N_I^- F_I + N_I^+ F_I = \left(N_I^- + N_I^+\right) F_I \,. \tag{4.36}$$

The determinant of the system is evaluated at each node of the grid, until a change in sign (between two nodes) of both the real and imaginary parts of the determinant is found. A two-dimensional secant method is thus used to determine the exact non-adiabatic eigenvalue.

The critical point of this method is that we require some prior knowledge of the non-adiabatic eigenvalue with respect to the corresponding adiabatic one. This has to be carefully taken into account in the calculation of the grid (and of individual models in general), as discussed in section [ref].

Input and Output

The basic input to the code that solves the linearised perturbation equations is the output from the envelope code, *i.e.*, the values of the mass, radius, luminosity, temperature and pressure at each mesh point j the star is divided in.

Note that the computation of stellar pulsations is particularly sensitive to small deviations from precise hydrostatic equilibrium. Since numerical deviations can arise

during the integration of an envelope, the resulting structure needs to be processed by a non-linear, hydrodynamic code (Olivier and Wood, 2005) in order to obtain a fully converged static model, that is the one actually passed in input to the pulsation code.

Additional input include the mixing length parameter, $\alpha_{\rm MLT}$, the number $N_{\rm modes}$ of eigenmodes to be searched, the starting point for the search of adiabatic eigenvalues along the imaginary axis (in the form of a maximum value of period, `Pmax`), and the parameters defining the search region in the complex frequency plane, for each one of the $N_{\rm modes}$ pulsation modes to be computed.

A treatment of turbulent viscosity is included in the code (Keller and Wood, 2006) that makes use of a free turbulent viscosity parameter α_ν. Positive values of the turbulent viscosity parameter modify the excitation of pulsation modes, making them more stable.

However, such parameter lacks an appropriate calibration as a function of stellar properties, and affect distinct pulsation modes in a different way. Therefore, it was set to $\alpha_\nu = 0$ in the models presented here, thus ignoring the effects of turbulent viscosity.

The output data consist of the complex frequencies for the $N_{\rm modes}$ modes, and the corresponding eigenfunctions, *i.e.*, the values of the perturbations variables δL_j, δr_j, $\delta \ln T_j$ and $\delta \ln P_j$ at each mesh point $j = 1$, ..., $N-1$.

Two additional quantities are provided for each mode: the partial work integral W_r and the partial frequency contribution function $J\Sigma_r^2$ (see, *i.e.*, Cox and Giuli, 1968; Cox, 1980), that are computed as:

$$W_k = -\sum_{j=1}^{k-1} \pi \left(\frac{P}{\rho}\right)_{j+1/2} \mathbf{Im}\left(\delta \ln \rho^*_{j+1/2} \delta P_{j+1/2}\right) \Delta m_{j+1/2}\,, \tag{4.37}$$

$$\begin{aligned} J\Sigma_k^2 = & \sum_{j=1}^{k-1} \Bigg[\left(\frac{\Gamma_1 P}{\rho}\right)_{j+1/2} \left|\delta \ln \rho_{j+1/2}\right|^2 \Delta m_{j+1/2} + \\ & - \frac{4Gm_{j+1}}{r_{j+1}^3} \left|\delta r_{j+1}\right|^2 \Delta m_{j+1} \Bigg]\,. \end{aligned} \tag{4.38}$$

The partial work integral W_r can be used to investigate the regions of the star that give the main contributions to the stability/excitation of a mode (see, *e.g.*, Fig. 4.2). Similarly, the contribution of different regions to the frequency of a mode can be studied with $J\Sigma_r^2$.

In general, we will not describe a pulsation mode n in terms of its frequency ($\omega_n = \omega_{{\rm Re},n} + \mathbf{i}\omega_{{\rm Im},n}$), but rather of its period and growth rate, defined as:

$$P_n\,[\text{days}] = \frac{2\pi}{\omega_{{\rm Im},n}\,[\text{Hz}]} \cdot \frac{1}{86400\,\text{sec}}\,, \tag{4.39}$$

$$GR_n = \exp\left(2\pi \frac{\omega_{{\rm Im},n}}{\omega_{{\rm Re},n}}\right) - 1\,. \tag{4.40}$$

The growth rate GR_n of a mode represents the fractional change in its radius amplitude per pulsation cycle, and can be used to assess the stability of that mode, under the assumption that a mode with $GR_n < 0$ is stable, while a mode with $GR_n > 0$ is excited.

This kind of information is essential in order to compare results of theoretical models with observations. In fact, only the excited models can be expected to be observed, and therefore, only the modes with positive growth rate are to be compared with observations. Also, given a set of $N_{\rm modes}$ theoretical modes for a certain envelope

model, we can select the one with the largest growth rate (the "dominant" mode), that can be compared with the most significant periodicity in observed multi-periodic variables (those that are called "primary periods" in the OGLE Collection of Variables stars, see section 2.2.4).

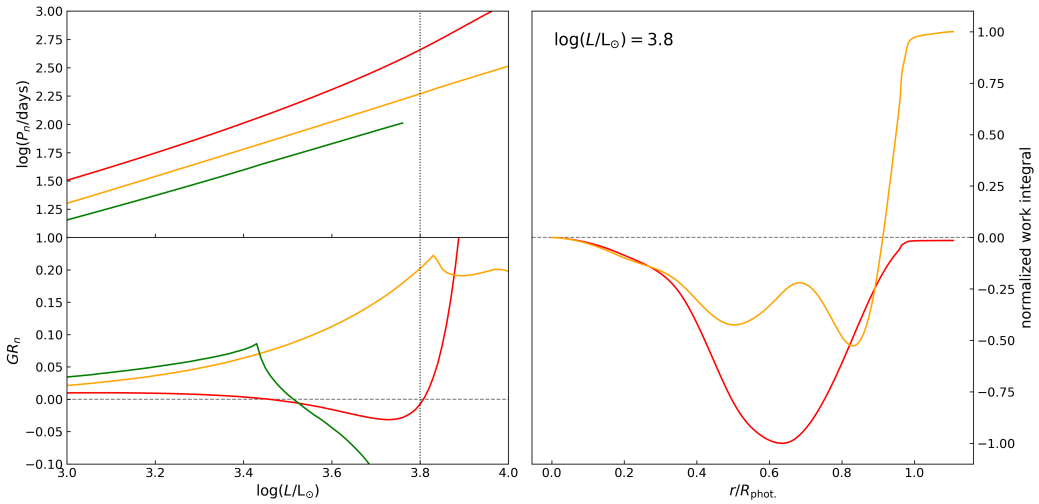

Figure 4.2: Left panels: periods (top) and growth rates (bottom) as a function of luminosity for the fundamental (red) first overtone (orange) and second overtone (gree) modes of a sequence of O-rich models with $M = 1\,\mathrm{M}_\odot$ and $Z = 0.014$. Right panel: work integral of the fundamental (red) and first overtone (orange) modes as a function of fractional radius in the model with $\log(L/\mathrm{L}_\odot) = 3.8$ (marked with a vertical dotted line in the left panels). The work integral is normalised to its maximum absolute value. The main contribution to the excitation of the first overtone mode is given by the region of partial ionisation of hydrogen.

It is worth to point out that growth rates are sensitive to the treatment of energy transport, much more than the periods.

A significant source of uncertainties affecting the growth rates is expected to originate in the treatment of convective transport in the static model and, most importantly, of the interaction between convection and pulsation. Both processes are dealt with in a simplified manner here.

Therefore, growth rates provide only an approximate indication of the behaviour of real stars in term of pulsational stability. In contrast, the values of periods can be considered reasonably correct.

A second remark is necessary, regarding the stability criterion. A mode with a positive but small growth rate, although theoretically assumed to be excited, is likely not to be observed.

In fact, as growth rates are expected to be indicative of the amplitude of pulsation, a very small growth rate should correspond to an amplitude too small to be observed.

This means that a better criterion would involve a positive threshold for the growth rates, below which modes are expected to be effectively stable.

What value should be used as a threshold is hard to tell on a purely theoretical standpoint. A constant value would probably be inappropriate, but a dependence upon stellar parameters is not trivial to derive. Moreover, the threshold is not necessarily the same for all modes.

A reasonable choice, in absence of more detailed information, is to calibrate the stability criterion in order to reproduce the observed instability strip of of the smallest amplitude variables, as described in section [ref].

4.4 Tools for Calculation Management

4.4.1 Series of Pulsation Models

It has been shown in the previous sections that input parameters for the computation of both the envelope and the pulsation models require some care in being set. This is especially true for the parameters defining the search grid of each eigenvalue in the frequency plane.

We recall that, in order to set appropriately such parameters, it is required to have some information on the expected distance of the non-adiabatic eigenvalue from the corresponding adiabatic one in the frequency plane.

One could ask if this is really necessary. In principle, a wide search of the frequency plane could be performed, using a large and fine-meshed grid, in order to be sure to find all the eigenvalues. This approach, however, has a number of problems, the main one being that it is time consuming, and thus not feasible for the computation of a large number of pulsation models.

The most convenient approach turns out to be based on the computation of a series of pulsation models with luminosity increasing by a small amount for each model. An example of the results is shown in Figures 4.3 and 4.4 where the periods and growth rates of several modes are plotted versus the luminosity of each model.

It is important to remark that, although it may mimic the average trend of evolution along the giant branch, such a series of models *is not* an evolutionary track.

In fact, a different approach (see section 4.5) is used to compute the evolution of pulsation, which makes use of the methods described in this section, but takes the relevant physical inputs directly from a true evolutionary track.

A characteristic feature of a series of pulsation models (or a "luminosity sequence") is displayed in Fig. 4.4 It is evident that the growth rates follow a pattern.

At relatively low luminosity (the exact range depending on the eigenmode and on the properties of the envelope model), the growth rate GR_n of a given mode n is positive but quite small. The growth rate has the tendency to increase with luminosity, making the corresponding mode increasingly unstable. This trend culminates at a peak-shaped maximum, corresponding to the maximum degree of excitation for that pulsation mode. Immediately after, the growth rate drops to large negative values, becoming definitively stable.

From a physical point of view, this is due to overtone modes reaching the acoustic cut-off frequency in the atmosphere. When the acoustic cut-off is exceeded, the mode's energy is dissipated through the atmosphere via running waves, causing the strong damping right after the maximum of the growth rate.

Note that the first overtone might deviate from this pattern and maintain a positive growth rate for some time after the maximum (as in Fig. 4.4), depending on the properties of the envelope model.

The fundamental mode shows a completely different behaviour. Its growth is almost constant with luminosity throughout most of the luminosity sequence. At a certain point, it even decreases with luminosity, down to a minimum value (possibly negative),

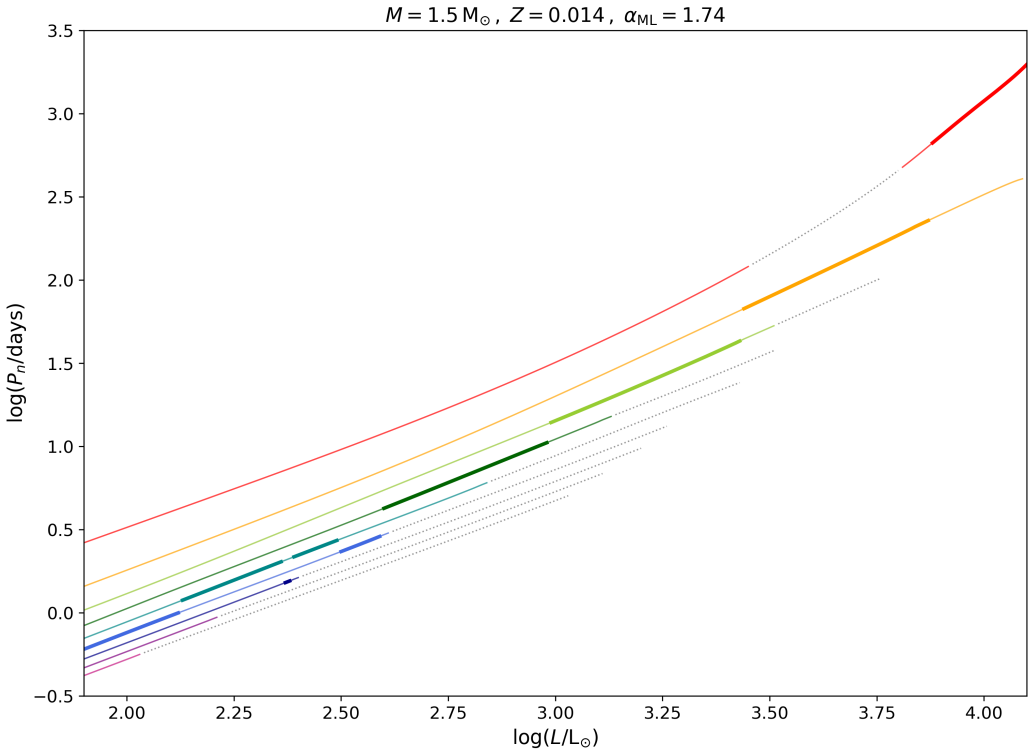

Figure 4.3: Example of a series of pulsation models with $M = 1.5\,\mathrm{M}_\odot$ and $Z = 0.014$. Modes from the fundamental (longest period) to the eighth overtone (shortest period) are shown. Dotted lines indicate that the corresponding mode is not excited. Coloured lines correspond to excited modes, and are thicker where modes are dominant (largest growth rate than all other modes).

after which it starts rising very steeply. This last phase of very strong driving is though to correspond to the latest evolution of a Long-Period Variable, when it becomes a large amplitude, fundamental radial pulsator, *i.e.*, a Mira variable.

The fact that a mode's growth rate (and thus the real part of its frequency, see Eq. 4.40) is close to zero at low luminosities means that the non-adiabatic eigenvalue is close to the adiabatic one in the complex frequency plane. At luminosities in the range $2 \lesssim \log(L/\mathrm{L}_\odot) \lesssim 3$ (depending on stellar mass), this is true for all modes we are interested in.

This explains why it is convenient to compute models in series of increasing luminosity. In fact, at low luminosity, the search grid for each mode in the frequency plane can be defined in a small region around the origin. If luminosity is increased by a small step, the eigenvalues do not change much from model to model, so that their path in the frequency plane can be followed with continuity. Once a few models have been computed, their eigenvalues can be used to extrapolate those of the next model. To be effective, this method also requires the luminosity step to be small enough and constant (in $\log(L/\mathrm{L}_\odot)$).

The extrapolation scheme we employed is essentially based on an empirical knowledge of the behaviour of the eigenvalues in typical models of evolved red giants. Basically, the parameters defining the search grid in the frequency plane are increased proportionally to the change in eigenfrequency between the last three models of the

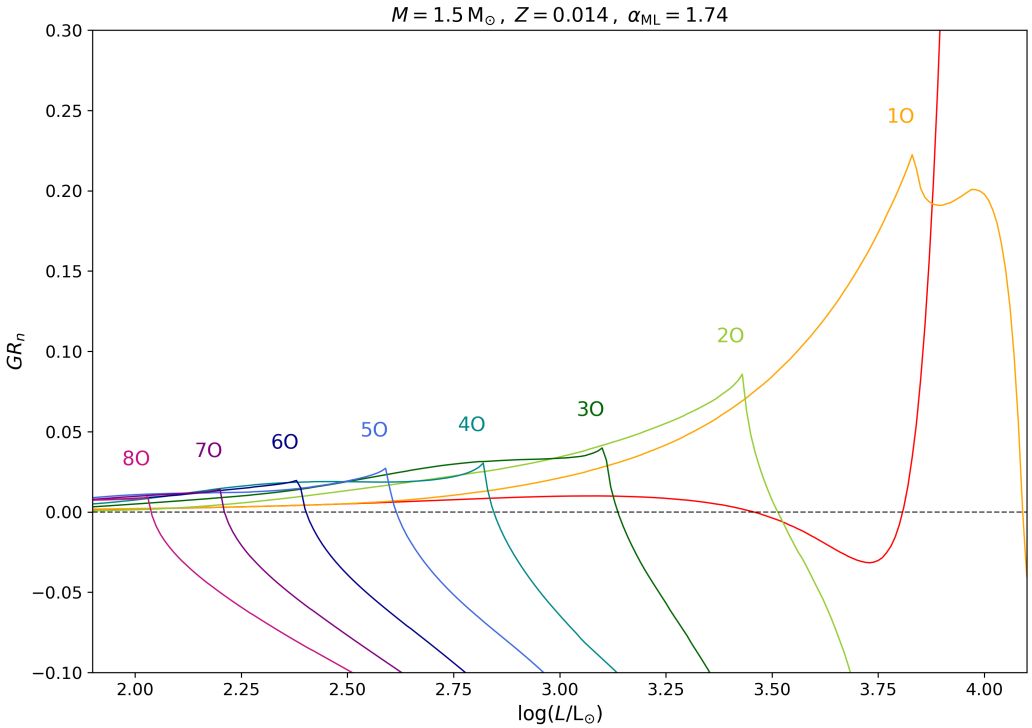

Figure 4.4: Growth rates for the same series of pulsation models of Fig. 4.3. There is a very evident pattern with modes being marginally stable ($GR \sim 0$) at relatively low luminosity, then becoming increasingly unstable as the growth rate grows to a maximum value, and becoming strongly damped immediately afterwards, as the mode's frequency exceeds the acoustic cut-off in the atmosphere. The higher the luminosity, the lower the radial order of the dominant mode.

series that have been computed. This is the same scheme employed in previous applications of the pulsation code used here (Wood, 2017, private communication) with some small variants to account for the fact that we explored a wider region of the space of stellar parameters. Modifications include the fact that, when an eigenvalue is "missed", *i.e.*, not found within the specified search region, the search grid is expanded and the computation is repeated until that mode is found or a maximum number of iterations is reached. In the latter case, that mode is discarded.

Note that, if such convergence failure occurs for, say, the mode $n_{\rm miss}$, the only way to exclude it from the computation is to reduce the number $N_{\rm modes}$ to be computed down to $N_{\rm modes} = n_{\rm miss} - 1$. This means that all modes of order $n > n_{\rm miss}$ are also abandoned, which in principle represent a significant problem in the computation of a series of model.

Since this kind of situation can arise due to numerical instability, there is no way to be sure to avoid it. We did, however, check all series of models computed to assemble the grid of pulsation models (section 4.8) to assess the importance of the problem, and found only a small fraction ($< 1\%$) of them to be affected. Those series have then been recomputed with the supervision of a user.

For practical purposes, global stellar parameters and pulsation parameters of the models a series consist of are then collected in a single file. It has a tabular structure were each column correspond to a global parameter, and each row to a model

with different luminosity. To maintain a regular format, periods and growth rates of abandoned modes are replaced with undefined values.

4.4.2 Handling Strange Modes

It has been shown by Wood and Olivier (2014), using the same linear pulsation code employed in this work, that two independent sets of radial modes can be found in luminous red giants.

Modes belonging to the first group are the usual normal modes of pulsation, corresponding to the ones observed in LPVs.

The other group is formed by the red giant equivalent of the so-called strange modes encountered in classical Cepheids and RR Lyrae variables, as well as in massive main-sequence stars.

Strange modes may occur in different types of stars with high luminosity-to-mass ratios. The interior amplitude in these modes is much smaller than that in the outermost layers, so that they are strongly concentrated on the surface (see Wood and Olivier, 2014, their Fig. 1).

This behaviour is due to the presence of a region in the outer layers acting as a potential barrier, effectively confining the pulsation to the surface. In the case of luminous red giant star, this role is played by the region of partial ionisation of hydrogen.

In the present work, we are not interested in studying strange modes, but we need to account for their appearance in models. A discussion on the properties of strange modes can be found, *e.g.*, in Saio et al. (1998).

Note that, in principle, two distinct modes cannot have the same eigenvalue, so that they should avoid crossing.

This is not necessary in the case of non-adiabatic modes, as their eigenfrequency consist of a real and an imaginary part. Therefore, a normal mode and a strange one can have the same period (imaginary part of the eigenfrequency), provided that they have a different growth rate.

Indeed, strange modes in luminous red giant models always have much smaller growth rates than normal modes.

Thus, normal modes and strange modes often cross (either in the real or imaginary part of the frequency). Avoided crossings also occur, in which case the normal mode and the strange one exchange in character.

Being so strongly damped, strange modes are not expected to be observed in LPVs. However, strange modes can appear in models, and can have the same period as another normal mode.

This fact represent a possible source of error in the automated computation of pulsation models, which has to be taken into account. Therefore, our only interest in strange modes is to avoid them.

This can be done in a rather simple way, *i.e.*, by discarding all modes that have growth rates smaller than a certain limit. In fact, although we did not perform a systematic analysis of strange modes, we noticed that in general they have $GR_n \lesssim -0.5$, while normal modes generally have larger growth rates than that value.

In order to be sure to avoid strange modes,, we arbitrarily placed the limit at $GR_{\min} = -0.2$. Of course, this means that some normal modes may be discarded. However, they would be so damped to be unobservable, and therefore of no interest to use.

Moreover, normal modes that reach so small growth rates have likely already exceeded the acoustic cut-off, so that not only they are very stable, but they will stay so for the rest of the luminosity sequence (see Fig. 4.4).

At a given point along a luminosity sequence, we have a set of $N_{\rm modes}$, of which some are excited and some other are stable. We know that, as luminosity increases, one of those mode is going to reach the acoustic cut-off, and thus it will become definitively stable. That mode is the one of highest radial order among the ones we are following. That mode is also the next one that will drop below the growth rate threshold. When that happen, it can be discarded by decreasing the input value of $N_{\rm modes}$ by one. This way, we are sure to discard only that mode.

Eventually, all overtone modes are abandoned, but not the fundamental mode, that never exceeds the acoustic cut-off. However, as it becomes increasingly non-adiabatic, it also becomes more difficult to compute, in spite of the extrapolation method and the iterative expansions of the grid, so that it is also eventually abandoned. When this occurs, the computation of the series of models is "spontaneously" concluded.

4.5 Pulsation Along an Evolutionary Track

A series of pulsation models as the one described in the previous section can be thought as a gross description of the evolution of a variable star along either the RGB or the AGB.

However, it is far from an evolutionary track. In fact, the evolution of the core mass is only approximately modelled, and processes such as mass loss and dust formation are not included. Nuclear energy generation is not considered at all.

Most importantly, thermal pulses are completely neglected, so that the chemical evolution due to dredge-up events is ignored as well as the changes in structure and luminosity.

Therefore, if one is interested in investigating the actual behaviour of pulsation during realistic evolution, luminosity sequences are not appropriate.

On the other hand, it is possible to apply a scheme entirely similar to the one used to produce luminosity sequences in order to compute pulsation models corresponding to a sequence of evolutionary models.

While sequences of pulsation models are most suitable to be assembled into a larger structure of models, *i.e.*, a grid, pulsation models along evolutionary tracks are the appropriate tool for the interpretation of the results.

Pulsation models along evolutionary tracks turn out to be more realistic for a number of reasons. All global stellar parameters to be passed as input are taken directly from evolutionary models.

This allows us to include realistic values of the core mass rather than using an approximate relation with luminosity. This is especially important when such a relation becomes completely inappropriate, for instance during the luminosity dip corresponding to a thermal pulse or in stars undergoing Hot-Bottom Burning[2].

[2]In principle, the assumptions made in the computation of envelope models (section 4.3.1) are valid only for quiescent TP-AGB phases with no HBB. Results from the computation of pulsation models along evolutionary tracks that include thermal pulses and/or HBB should thus be handled with some care. Nonetheless, they should give a reasonable picture of the behaviour of pulsation in those conditions.

Table 4.1: Calibration of the mixing length parameter $\alpha_{\rm MLT}$ for pulsation models applied to the study of long-period variables in globular clusters in studies that made use of the same stellar pulsation code employed in the present work.

Reference	Target	Calibration
Lebzelter and Wood (2005)	47 Tuc	$\alpha_{\rm MLT} = 1.80 - 1.90$
Lebzelter and Wood (2007)	NGC 1846	$\alpha_{\rm MLT} \propto L^{0.3}$
Lebzelter and Wood (2011)	NGC 362, NGC 2808	$\alpha_{\rm MLT} = 1.70$
Lebzelter and Wood (2016)	ω Cen	$\alpha_{\rm MLT} = 1.6$

Evolutionary tracks can include different prescriptions for mass-loss, allowing for a study of its impact on pulsation (but not their interaction).

Chemical composition changes due to dredge-up events are now included, and the effects of different values of C/O is accounted for in terms of opacity.

A critical aspect concerns the treatment of convection. The mixing length theory is used in both evolutionary models and static envelope models used in pulsation computations.

However, due to a number of different assumptions and approximations (mainly in terms of boundary conditions), even if the same $\alpha_{\rm MLT}$ is used in both static envelope models and evolutionary models, the results may be slightly different.

Such differences, mostly noticeable in terms of effective temperature, become significant in somewhat "extreme" models, *i.e.*, those with very high or very low metallicity, or those with a high luminosity and an envelope much less massive than the core.

As discussed in section 4.3.1, the calibration of the mixing length parameter for pulsation models is necessarily different than what is usually done for evolutionary models.

In the latter case, the calibration is performed by reproducing the observed properties of the present Sun, which generally yields values around $\alpha_{\rm MLT} \sim 1.8$.

In the case of `COLIBRI`, a value $\alpha_{\rm MLT} = 1.74$ is used based on the calibration of the `PARSEC` code (PAdova and TRieste Stellar Evolution Code, Bressan et al., 2012).

In general, the calibrate value is then assumed to be valid for all evolutionary phases of all kinds of stars (although there is no theoretical reason for such an assumption).

Obviously, the same kind of calibration cannot be done for pulsation models. The standard approach is that of tuning the value of $\alpha_{\rm MLT}$ to reproduce a chose effective temperature.

This has been applied, for instance, in the study of long-period variables in several globular clusters (Lebzelter and Wood, 2005, 2007, 2011, 2016, note that all these studies made use of the same codes employed in the present work), where the mixing length parameter was calibrated in order to reproduce the slope and position of the observed giant branch.

Calibrated values for those studies, summarised in table 4.1, vary between 1.6 and 1.9. The case of NGC 1846 (Lebzelter and Wood, 2007) is peculiar, in that a dependence on luminosity had to be assumed to reproduce observations.

It is evident that, although the values so obtained are largely consistent with most calibrations of evolutionary models, $\alpha_{\rm MLT}$ is really a free parameter that needs to be tuned appropriately depending on the requirements of the study one wants to perform.

For the purpose of computing pulsation models along an evolutionary track, the reference quantity to tune $\alpha_{\rm MLT}$ is the theoretical effective temperature from evolutionary

models. We developed a simple scheme based on a semi-implicit bisection method, similar to that described in Fox and Wood (1982).

Given a target $T_{\rm eff}$ to reproduce, we procede as follows. To begin with, a range of $\alpha_{\rm MLT}$ is determined within which convergence of an envelope model for a given physical input is possible (values of $\alpha_{\rm MLT}$ that are too small or too large cause the envelope model to be dynamically unstable).

Then, two values of $\alpha_{\rm MLT}$ are selected in that range, such that envelope models computed with those values produce effective temperatures bracketing the target value.

Assuming an approximately linear relation between $T_{\rm eff}$ and $\alpha_{\rm MLT}$), a new value of the mixing length parameter is computed by linear interpolation on the effective temperatures of the two models.

The new value is used to compute a new envelope model, that replaces one of the other two in the next step of the bisection method.

The process is iterated until the target effective temperature is reproduced within a certain tolerance.

Note that, aside of the different source of input parameters, the procedure is really similar to that of computing a pulsation sequence.

In fact, the same kind of issues are encountered, such as the requirement to appropriately set the eigenvalue search grid in the complex frequency space, and that of avoiding strange modes.

Therefore, even when pulsation models are computed along an evolutionary track, one has to start at a low enough luminosity, and has to use a small step in $\log(L/{\rm L}_\odot)$ between two consecutive models.

Evolutionary tracks used as input come in the form of global stellar parameters sequentially listed as a function of increasing age since the beginning of TP-AGB.

It is possible that they do not satisfy the requirements on luminosity, *i.e.*, a low starting value and a small step. In those cases, some pre-processing is performed. All global parameters are extrapolated to a low enough luminosity, and are inserted as new starting point of the track. Then, additional points are inserted by linear interpolation between every pair of consecutive models that are that are not closely enough spaced in luminosity.

4.6 Management of Opacity Libraries

As discussed in section(s) [ref], the occurrence of repeated third dredge-up events during the TP-AGB can result in the production of carbon stars. In such stars, the abundance of carbon atoms by number is larger than that of oxygen. This is measured in terms of the carbon-to-oxygen number ratio, C/O.

This has a significant consequences on the sources of opacity in the atmospheric layers, where the temperature is low enough for molecules to form. In fact, given the high binding energy of the CO molecule, almost all atoms of the least abundant element (C or O) are locked into form CO. The remaining atoms of the most abundant of the two elements can then form other molecular species.

This drastic alteration of molecular equilibria and opacities at the transition C/O $\sim$ 1 is displayed in Fig. 4.5 and 4.6. Fig. 4.7 shows the same effect in terms of the dependence of the Rosseland mean opacity upon temperature and C/O.

In fact, the spectra of O-rich and C-rich stars exhibit completely different molecular features. The former present strong absorption bands of TiO, VO and H_2O, while the

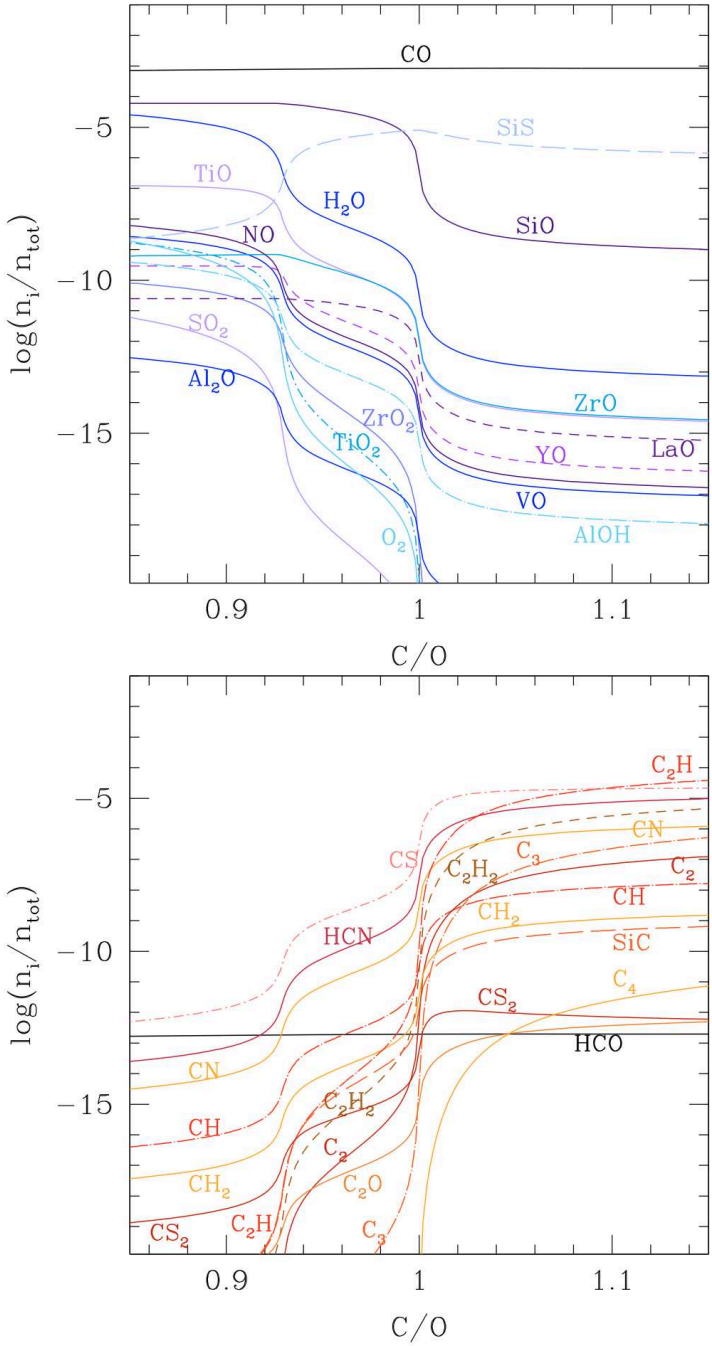

Figure 4.5: Concentrations of several gas species as a function of the C/O ratio, in a gas mixture with $\log(T) = 3.3$, $\log(R) = -3$ (or equivalently $\log(\rho) = -11.1$), $Z_{\rm ref} = 0.02$, and $X = 0.7$, and adopting the reference solar mixture of Grevesse et al. (2007). The increase of C/O follows that of C, while O abundance is kept unchanged. The actual metallicity Z also increases with C. The molecules are divided into two groups, namely: O-bearing moleculs (top panel) and C-bearing molecules (bottom panel). Note the sharp change in molecular concentrations at C/O $\sim$ 1 (reproduced from Marigo and Aringer (2009))

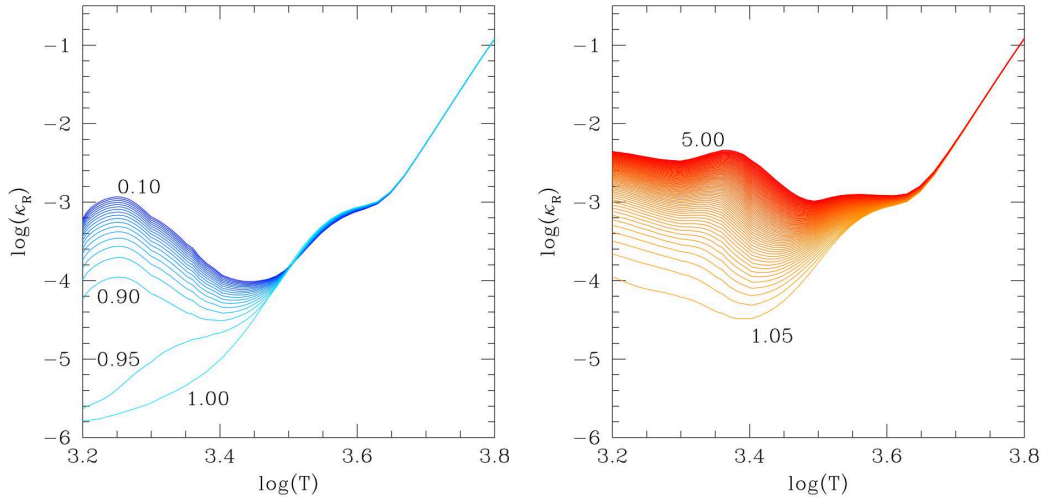

Figure 4.6: Rosseland mean opacities, computed with `AESOPUS`, according to the temperature-pressure stratification of a complete envelope-atmosphere model with $\log(T_{\rm eff}) = 3.45$, $\log(L/{\rm L}_\odot) = 3.7$, $M_i = 2\,{\rm M}_\odot$ and solar metallicity $Z_i = Z_\odot \sim 0.0152$ according to Caffau et al. (2011). The C/O ratio is increased from 0.10 to 1.00 (left panel) and from 1.05 to 5.00 (right panel) in steps of 0.05 (reproduced from Marigo et al. (2013)).

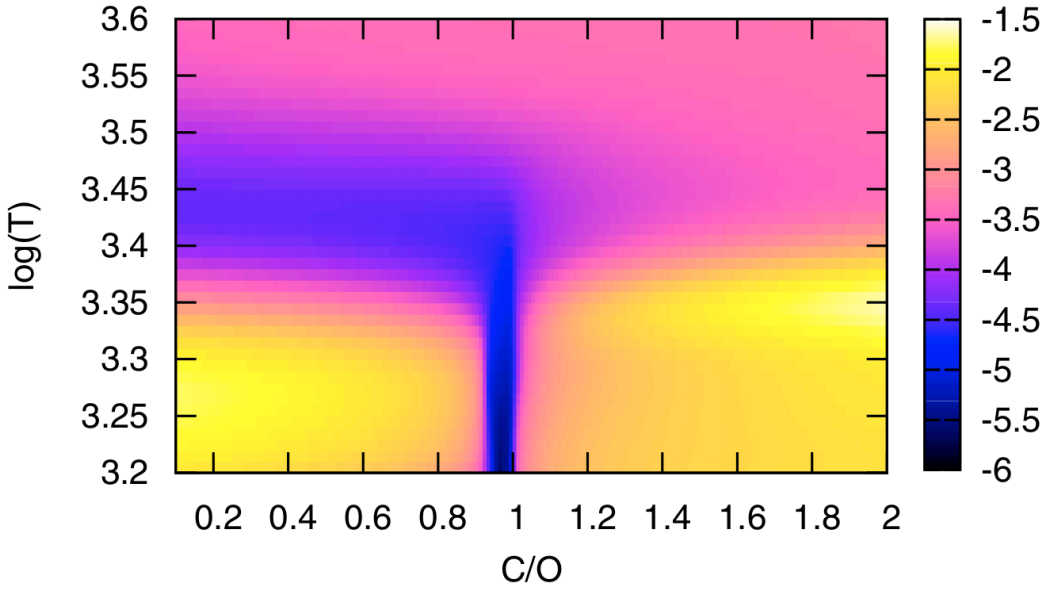

Figure 4.7: Rosseland mean opacity as a function of the temperature and increasing C/O, adopting the solar mixture of Grevesse et al. (2007), and assuming $Z_{\rm ref} = 0.02$, $= 0.7$, and $\log(R) = -3$. The abundance of carbon is made vary accordingly to the current C/O ratio (so that the actual metallicity varies as well), while that of oxygen is kept fixed at its scaled-solar value.

latter are dominated by those of C_2, CN and SiC.

From a theoretical point of view, larger atmospheric opacities usually correspond to lower effective temperatures and larger radii, *i.e.*, lower mean densities of the stellar envelope.

Since the pulsation periods are directly connected with the mean density of the envelope, it is immediately clear that a systematic analysis of stellar pulsation in the AGB must account for such effects. In particular, it is necessary to: (1) account for changes of the chemical composition in terms of metallicity and the individual abundances of carbon and oxygen, and (2) employ opacity data that is entirely consistent with the given chemical composition. In other words, opacities computed assuming a scaled-solar composition are not appropriate for this study.

Our approach to study stellar pulsation in AGB stars relies on the computation of a grid of models, therefore we will need to compute models for different chemical compositions.

Opacity data is supplied to the stellar pulsation code (section [ref]) through tables providing values of the Rosseland mean opacity $\kappa_{\rm R}$ as a function of temperature and density, for a given composition. We thus computed suitable libraries of opacity tables to be used in the calculation of the grid of pulsation models.

In the present section we will describe the tools and data used to compute the opacity tables, *i.e.*, the `AESOPUS` code, the `OP` suite of programs and opacity data, and the tools we designed to combine the output of the two codes into tables appropriate for the pulsation code. Then, we will describe the properties of the opacity library used in the computation of the grid.

4.6.1 `AESOPUS`

The code `AESOPUS` (Accurate Equation of State and OPacity Utility Software Marigo and Aringer, 2009) is a tool to compute the equation of state and Rosseland mean opacity of ideal gases of arbitrary chemical mixtures. It covers the low-temperature regime, $3.2 \leq \log(T/\mathrm{K}) \leq 4.5$), for gas densities in the range $-8 \leq \log(R) \leq 1$, where

$$R = \frac{\rho\,[\mathrm{g\,cm^{-3}}]}{(T\,[\mathrm{K}]/10^6)^3}\,. \tag{4.41}$$

The chemical network includes ~ 300 atomic species and ~ 500 molecular species. The treatment of opacity includes continuum and discrete sources, such as atomic transitions, molecular bands and colliison-induced absorption.

The computational performance is optimised by using pre-tabulated absorption cross-sections from metals (from the `OP` database) and by employing the opacity sampling method to describe molecular line absorption. Marigo and Aringer (2009) have shown that the resulting $\kappa_{\rm R}$ are comparable with those of other opacity codes, and thus their method represent an ideal compromise between good accuracy and computational efficiency.

The large degree of freedom in choosing the chemical composition of the gas is especially appropriate for our purpose, allowing us to vary the abundances of CNO elements.

Input/Output

The computation of Rosseland mean opacity with `AESOPUS` requires the following input[3]:

[3]Note that, being a multi-purpose tool, `AESOPUS` requires slightly different input according to the kind of study one is interested in. Our purpose is the study of AGB stars, thus the relevant input

- the reference metal mixture (a number of choices are possible, see Marigo and Aringer (2009), their table 3);
- the reference metallicity, $Z_{\rm ref}$, used to scale the reference metal mixture;
- the reference hydrogen abundance by mass fraction, $X_{\rm ref}$;
- the variation factors of CNO elements with respect to the reference mixture.

The reference mass fraction $Y_{\rm ref}$ of helium is set implicitly by the condition:

$$X_{\rm ref} + Y_{\rm ref} + Z_{\rm ref} = 1\,. \tag{4.42}$$

Variation factors of CNO elements are given by the following expressions:

$$f_{\rm C} = \log(X_{\rm C}) - \log(X_{\rm C})_{\rm ref}\,, \tag{4.43}$$
$$f_{\rm N} = \log(X_{\rm N}) - \log(X_{\rm N})_{\rm ref}\,, \tag{4.44}$$
$$f_{\rm O} = \log(X_{\rm O}) - \log(X_{\rm O})_{\rm ref}\,. \tag{4.45}$$

It is usually convenient to replace the latter with the variation factor of the C/O:

$$f_{\rm C/O} = \log\left(\frac{X_{\rm C}}{X_{\rm O}}\right) - \log\left(\frac{X_{\rm C}}{X_{\rm O}}\right)_{\rm ref} = f_{\rm C} - f_{\rm O}\,. \tag{4.46}$$

When variations of the CNO elements are applied to the reference metal mixture, metallicity is not preserved with respect to the reference value. In other words, an increase of one of more of the mass fractions of carbon, nitrogen and/or oxygen correspond to an equivalent increase in the total metallicity. Since the condition must hold that

$$X + Y + Z = 1\,, \tag{4.47}$$

an increase $\Delta Z = Z - Z_{\rm ref}$ in metallicity with respect to the reference value is compensated by an equal decrease in helium abundance with respect to $Y_{\rm ref}$:

$$Y = Y_{\rm ref} - \Delta Z\,. \tag{4.48}$$

On the other hand, the hydrogen mass fraction is preserved. Note that this is substantially consistent with stellar evolution, as the new CNO elements that increase the metallicity are produced by reactions that deplete helium.

Assuming the only element that can be varied are C, N and O, the relation between the actual metallicity Z and the reference one $Z_{\rm ref}$ is:

$$\begin{aligned} Z &= Z_{\rm ref}\left[\left(\frac{X_{\rm C}}{Z}\right)_{\rm ref}\left(10^{f_{\rm C}} - 1\right) + \right. \\ &+ \left.\left(\frac{X_{\rm N}}{Z}\right)_{\rm ref}\left(10^{f_{\rm N}} - 1\right) + \left(\frac{X_{\rm O}}{Z}\right)_{\rm ref}\left(10^{f_{\rm O}} - 1\right)\right], \end{aligned} \tag{4.49}$$

where the quantities $(X_{\rm C}/Z)_{\rm ref}$, $(X_{\rm N}/Z)_{\rm ref}$, and $(X_{\rm O}/Z)_{\rm ref}$ have been specified in terms of the reference metal mixture. It is clear that $Z = Z_{\rm ref}$ only when $f_{\rm C/O} = f_{\rm C} = f_{\rm N} = 0$.

parameters concern the variation of CNO abundance. We limit our description to this case, and remand the interested reader to Marigo and Aringer (2009) for further details.

Additional input includes the specification of the temperature and density grid. We always used the following grid:

$$\begin{aligned} \log(T) &\in [3.2, 3.5] \quad \text{in steps of} \quad 0.01\,, \\ &\in]3.5, 4.5] \quad \text{in steps of} \quad 0.05\,, \\ \log(R) &\in [-8.0, 1.0] \quad \text{in steps of} \quad 0.5\,. \end{aligned}$$

The output consist of a table of Rosseland mean opacity in the specified $\log(T)$–$\log(R)$ nodes, together with the actual metallicity and helium mass fraction, and the individual abundances of heavier elements after applying the CNO variations.

4.6.2 Opacity Project

Opacity data obtained with `AESOPUS` are appropriate to describe gases at temperature lower than $\log(T/\mathrm{K}) = 4.5$, *i.e.*, the outer stellar layers, including the atmosphere, of RGB and AGB stars. `AESOPUS` opacities need thus to be complemented with those for the high temperature regime, for which we made use of data and codes from the Opacity Project provided in the package described in Seaton (2005), and references therein.

The package consist of all `OP` monochromatic opacities, together with the codes required for the computation of the Rosseland mean opacity for arbitrary chemical mixtures (we used the `mixv.f` code). The covered ranges in temperature and density are:

$$\begin{aligned} 3.5 \leq \log(T\,[\mathrm{K}]) \leq 8.0\,, \\ -7.5 \leq \log(R) \leq 1.0\,, \end{aligned}$$

where R is defined as in Eq. 4.41.

Input/Output

The computation of opacity data with the `OP` code requires the following input parameters to be specified:

- the hydrogen mass fraction, X;
- the metallicity Z;
- the relative abundance of individual metals.

Note that individual abundances can be specified for any combination of the 15 elements C, N, O, Ne, Na, Mg, Al, Si, S, Ar, Ca, Cr, Mn, Fe and Ni.

The temperature and density ranges have also to be specified in input. In order to `AESOPUS` and `OP` tables compatible with each other, we used the following structure:

$$\begin{aligned} \log(T) &\in [3.5, 4.5] \quad \text{in steps of} \quad 0.01\,, \\ &\in]4.5, 6.0] \quad \text{in steps of} \quad 0.05\,, \\ &\in]6.0, 8.0] \quad \text{in steps of} \quad 0.1\,, \\ \log(R) &\in [-7.5, 1.0] \quad \text{in steps of} \quad 0.5\,. \end{aligned}$$

Note that the range of $\log(R)$ in `OP` is slightly smaller than that of `AESOPUS` at low values, so that the smallest node is missing. To account for this, we usually extrapolate to $\log(R) = -8.0$ when merging tables from the two codes (see next section).

4.6.3 Handling Opacity Tables

In order to combine opacity data from `AESOPUS` and `OP`, we employ the following procedure.

We start by computing a table of low-temperature opacity with `AESOPUS`, for a given combination of metal mixture, reference metallicity, hydrogen abundance and variation factors of CNO elements.

Then, we compute an opacity table with the `OP–mixv.g` code using the same hydrogen mass fraction, and we set the input values of the true metallicity Z and of the relative abundances of metals by taking the corresponding output from the `AESOPUS` table.

Rosseland mean opacity at $\log(R) = -8.0$ is extrapolated linearly from the nodes $\log(R) = -7.5, -7.0$. We checked visually for a sample of tables that the result is smooth, but in general we do not expect to the conditions in the interior of our models to reach this region of the $\log(T)$–$\log(R)$ space, so that this approach can be considered reasonably safe.

The tables are then merged together. In the overlapping temperature range, $3.5 \leq \log(T) \leq 4.5$, a weighted mean of values from each table is taken. Weights are taken to vary linearly from 0 to 1 between the edges of this region: the `AESOPUS` table has weight 1 at $\log(T) = 3.5$, where the weight is 0 for the `OP` table, then the former's weight is decreased down to 0 in correspondence to $\log(T) = 4.5$, where the `OP` table has weight 1. This procedure allows us to smoothly merge the two tables.

Finally, conductive opacities are added using data from Hubbard and Lampe (1969) and Canuto (1970).

The resulting table is defined on the following $\log(T)$–$\log(R)$ grid:

$$\begin{aligned}
\log(T) &\in [3.2, 3.5] \quad \text{in steps of} \quad 0.01\,, \\
&\in\ ]3.5, 6.0] \quad \text{in steps of} \quad 0.05\,, \\
&\in\ ]6.0, 8.0] \quad \text{in steps of} \quad 0.1\,, \\
\log(R) &\in [-8.0, 1.0] \quad \text{in steps of} \quad 0.5\,.
\end{aligned}$$

The resulting table is in the format appropriate to be read by the pulsation code, which will use opacity data by means of a bi-cubic fit over the temperature-density grid. The table includes information on the chemical composition in terms of the reference metallicity $Z_{\rm ref}$ and the true metallicity Z, and the abundances by mass fraction of hydrogen, helium and the CNO elements.

Since the starting point of the procedure is the computation with `AESOPUS`, the identifying parameters of the final table are the input data to `AESOPUS`: $Z_{\rm ref}$, X, $f_{\rm C}$, $f_{\rm N}$ and $f_{\rm O}$ (or $f_{\rm C/O}$).

4.6.4 Opacity Library

Using the method describe above, we computed two grids of opacity tables, labelled `OPAC16` and `OPAC17`, summarised in tables [ref] and [ref]. The grids were obtained by varying values of:

- reference metallicity, $Z_{\rm ref}$;
- hydrogen mass fraction, X;

- C/O variation factor, $f_{\mathrm{C/O}}$;
- C variation factor, f_{C}.

We used the reference solar mixture provided by Caffau et al. (2011).

We did not vary the abundance of nitrogen, keeping it fixed to the scaled-solar value ($f_{\mathrm{N}} = 0$). The value of the oxygen variation factor is implicitly defined by setting f_{C} and $f_{\mathrm{C/O}}$ (see Eq. 4.46).

The two grids have the same sampling in terms of X and $f_{\mathrm{C/O}}$, but differ in the sampling of Z_{ref} and f_{C}. In fact, the `OPAC16` grid has a wider range in Z_{ref}, from 10^{-4} to 0.06, and was computed under the simplifying assumption that variations of the C/O with respect to the reference value are due entirely to changes in the abundance of C, while O is kept fixed to the scaled-solar value. In terms of input parameters, this means that $f_{\mathrm{O}} = 0$ and $f_{\mathrm{C/O}} = f_{\mathrm{C}}$ for all tables in the `OPAC16` grid.

On the other hand, the `OPAC17` grid, computed for Z_{ref} in the smaller range 0.001–0.017, includes the possibility of changes of O with respect to the reference value.

The different structures of the grids, and related assumptions, reflect the fact that they have different purposes.

The grid `OPAC16` is intended to be used for the calculation of the grid of pulsation models. The grid parameters and corresponding ranges and sampling were chosen to be representative of the chemical composition of AGB stars, so that the nodes of the opacity grid will also be nodes of the pulsation grid.

The justifications for assuming a fixed, scaled-solar abundance of oxygen are that (1) on the basis of a preliminary analysis, oxygen is expected to have a minor effect on the pulsation properties of AGB stars, the relevant dependence being upon C/O, and (2) that this assumption allows for a reduction of the computational time by at least a factor of 10 in the construction of the pulsation grid. We aim to investigate in more detail the effects of non scaled-solar oxygen abundances on pulsation properties in a future work.

The grid `OPAC17`, on the other hand, includes tables with oxygen variations, and is intended for selected studies. Namely, tables for an arbitrary chemical composition (within the ranges of the grid) can be obtained by linear interpolation in the grid parameters. This approach is faster, although less precise, than computing and merging `AESOPUS` and `OP` tables, thus allowing for a higher degree of flexibility in the computation of pulsation models (see next section).

Values at grid nodes in the two opacity grids are summarised in tables 4.2 and 4.3.

4.6.5 An Interpolation Tool for Opacity Tables

Pulsation models need always to be computed with opacity data that is consistent with the input chemical composition, but this implies that the input chemical parameters to the computation of pulsation models are restricted to those of the opacity grid.

This limitation becomes an issue when, for instance, one wants to compute detailed pulsation models along an evolutionary track (where clearly the chemical composition cannot be limited to the opacity grid nodes) instead of estimating pulsation properties through the grid of pulsation models.

In principle, in order to compute a model with arbitrary composition, one should compute `AESOPUS` and `OP` tables anew, and merge them into one. On the other hand, a faster approach, with a small loss in terms of precision, consist in obtaining the new

Table 4.2: Nodes in the opacity grid `OPAC16`.

Parameter	Nodes			
$Z_{\rm ref}$	0.0001	0.0002	0.0005	0.001
	0.002	0.004	0.006	0.008
	0.01	0.014	0.017	0.02
	0.03	0.04	0.05	0.06
X	0.5	0.6	0.7	0.8
$f_{\rm C/O}$	-0.263	0.0	0.105	0.238
	0.260	0.281	0.374	0.515
		0.737	0.959	
$f_{\rm C}$	($f_{\rm C} = f_{\rm C/O}$)			
$f_{\rm N}$	0.0			
$f_{\rm O}$	0.0			

Table 4.3: Nodes in the opacity grid `OPAC17`.

Parameter	Nodes			
$Z_{\rm ref}$	0.001	0.002	0.004	0.006
	0.008	0.01	0.014	0.017
X	0.5	0.6	0.7	0.8
$f_{\rm C/O}$	-0.263	0.0	0.105	0.238
	0.260	0.281	0.374	0.515
		0.737	0.959	
$f_{\rm C}$	-0.263	0.0	0.105	0.238
	0.260	0.281	0.374	0.515
		0.737	0.959	
$f_{\rm N}$	0.0			
$f_{\rm O}$	(defined by $f_{\rm C/O} - f_{\rm C}$)			

table by linear interpolation in the opacity grid. The appropriate set of opacity tables to do so is the one we labelled `OPAC17`, which includes both carbon and oxygen variations.

We developed a tool to perform this operation in an efficient and flexible way, that can be easily integrated with the codes described in section [ref].

The following scheme is employed. The required chemical composition is input in terms of metallicity Z and the mass fractions of hydrogen, carbon and oxygen (X, $X_{\rm C}$ and $X_{\rm O}$).

The corresponding values of $Z_{\rm ref}$, $f_{\rm C/O}$ and $f_{\rm C}$ are computed using Equations 4.49, 4.46 and 4.43, and are used to retrieve the appropriate opacity tables for the interpolation (recall that opacity tabels are identified by their values of $Z_{\rm ref}$, X, $f_{\rm C/O}$ and $f_{\rm C}$).

Multi-linear interpolation is thus performed over the parameters Z, X, $X_{\rm C}$ and $X_{\rm O}$. The resulting table is directly produced in the input format required for the pulsation code.

4.7 Models of Synthetic Stellar Populations

In this work we made use of the code `TRILEGAL` (Girardi et al., 2005), which features are briefly described in the present section.

`TRILEGAL` (TRIdimensional modeL of thE GALaxy) is a population synthesis code that can be used to produce realistic mock catalogues representative of the photometry of star clusters and galaxies, including the possibility to simulate the Milky Way foreground population.

The process of simulating the photometry of external galaxies makes use of:

- a set of stellar evolutionary tracks, consisting of bolometric magnitude, effective temperature, surface gravity, core mass, and other global stellar parameters, as a function of initial mass, age and metallicity;
- tables of bolometric corrections (as a function of effective temperature, surface gravity, and metallicity $[M/H]$) and relative absorption with respect to the V magnitude, both provided for several pass-bands;
- Initial Mass Function (IMF), Star Formation Rate (SFR), and Age-Metallicity Relation (AMR) for the target galaxy;
- IMF, SFR, AMR, and geometry of the Milky Way components associated to the observed foreground.

The code performs a Monte Carlo simulation according to a given probability distribution. Based on the input SFR, AMR, and IMF, a value of age, initial mass and metallicity is assigned to each star in the simulated sample.

Current stellar parameters are assigned based on an interpolation in the grid of evolutionary tracks, and are used to assign absolute magnitudes to simulated stars.

Finally, the apparent photometry is computed using bolometric corrections, distance modulus and extinction.

Heavy mass-loss during the TP-AGB produces dusty circumstellar envelope that change significantly the photometric properties of those stars. To account for this effect, suitable bolometric corrections are applied, based on dust models [ref].

Simulated photometric data can then be modified to reproduce observational effects such as photometric errors, incompleteness, etc.

The final output consist, for each simulated star, of bolometric luminosity, effective temperature, initial and final mass, age, metallicity $[M/H]$, C/O, core mass, etc., and the apparent magnitudes in the selected photometric system.

4.8 A Grid of Pulsation Models

4.8.1 Computation of the Grid

The tools and codes describe in the previous sections have been used to produce a grid of new, updated pulsation models, including chemistry and opacity data to describe O-rich and C-stars, and providing periods and growth rates for five radial pulsation modes, from the fundamental to the fourth overtone.

The grid construction process, pictured by the scheme in Fig. 4.8, can be summarised as follows.

To begin with, `COLIBRI` evolutionary tracks for the TP-AGB phase have been used to identify the key stellar parameters that change during AGB evolution, and their characteristic variation range.

Moreover, evolutionary tracks have been used to model the connection between some main quantities, in order to derive analytic relation useful to optimise the computation. We studied the following quantities.

We analysed the dependence upon total mass of the luminosity at the beginning of TP-AGB. This allowed us to define the starting values for luminosity sequences at different masses.

In order to compute envelope models, one needs a realistic first guess for the effective temperature, thus we derived a rough dependence of $T_{\rm eff}$ on mass, luminosity and metallicity.

Finally, we investigated the relation between core mass and luminosity. We aim to provide pulsation models not restricted to a single core mass-luminosity relation, proved to be a simplified description of real evolution.

Thus, we defined an appropriate range of core masses, at each luminosity, for which models have been computed.

A suitable sampling of the space of TP-AGB stellar parameters has been determined, that defines the structure of the grid.

We computed an opacity table for each combination of the chemical parameters, using the `AESOPUS` and `OP` codes. This resulted in the production of the opacity libraries described in section 4.6.

We used an especially designed suite of tools to handle the massive computation of models that make up the grid.

Pulsation models have been computed following the "luminosity sequence" approach for each combination of the other stellar parameters, chemical parameters and corresponding pre-computed opacity table.

The resulting grid is described in the following sections in terms of its coverage of the stellar parameters, namely:

- total mass, M;
- total bolometric luminosity, L;

Table 4.4: Parameters and corresponding nodes defining the structure of the grid of pulsation models.

Parameter	Nodes			
$M/\mathrm{M}_\odot$	$[0.6, 1.0]$	in steps of	0.05	
	$]1.0, 2.0]$	in steps of	0.1	
	$]2.0, 7.0]$	in steps of	0.2	
$\log(L/\mathrm{L}_\odot)$	lower limit: $\max(2.5, 3882\,M/\mathrm{M}_\odot - 9294)$			
	upper limit: 5.0			
	step: $\Delta \log(L/\mathrm{L}_\odot) = 0.01$			
M_c	$M_\mathrm{c,low}^\mathrm{TPAGB}(L)$, $M_\mathrm{c,up}^\mathrm{TPAGB}(L)$			
α_MLT	1.5, 2.0, 2.5			
Z_ref	0.001	0.002	0.004	0.006
	0.008	0.01	0.014	0.017
X		0.6	0.7	0.8
$f_\mathrm{C/O}$	-0.263	0.0	0.105	0.238
	0.260	0.281	0.374	0.515
		0.737	0.959	
$f_\mathrm{C} \equiv f_\mathrm{C/O}$	-0.263	0.0	0.105	0.238
	0.260	0.281	0.374	0.515
		0.737	0.959	

- core mass, M_c;
- mixing length parameter, α_MLT;
- hydrogen mass fraction, X;
- reference metallicity, Z_ref;
- variation factor of carbon with respect to the reference metal mixture.

The values of the grid nodes in terms of the above parameters are summarised in table 4.4.

The chemical parameters are the same as in the `OPAC16` grid of opacity tables, described in section 4.6, except for metallicity, that is limited to the range $0.001 \leq Z_\mathrm{ref} \leq 0.017$, and the hydrogen mass fraction that is between 0.6a dn 0.8.

For the mixing length parameter, we chose three values (1.5, 2.0, 2.5) that effectively bracket the range of α_MLT required to reproduce effective temperatures from evolutionary tracks (see section 4.5).

The characteristic ranges of total mass, core mass and luminosity are not independent of each other, so that an absolute definition of the nodes of those parameters is not possible.

The sampling in those cases is described in the following sections.

Mass-Luminosity Coverage

TP-AGB stars have masses approximately in the range $0.8 \lesssim M/\mathrm{M}_\odot \lesssim 8.0$, depending on metallicity and model details.

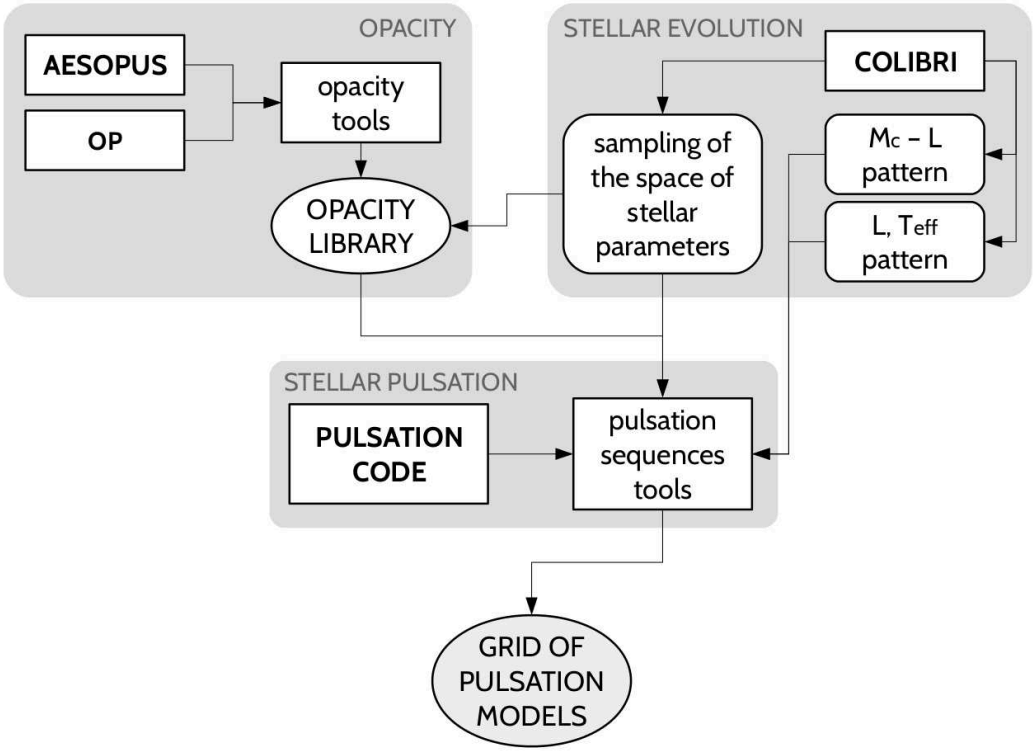

Figure 4.8: Schematic description of the steps involved in the production of the grid of pulsation models. Opacity tables for specific chemical compositions are computed with `AESOPUS` and the `OP`. The computation and merging of the tables is handled by a specifically designed set of tools. TP-AGB evolutionary tracks computed with `COLIBRI` are used to: (1) define the range and sampling of the grid parameters, and (2) study the relevant dependencies of input parameters for the pulsation code. This information is supplied to a suite of programs that handles in detail the computation of pulsation models and links it to the opacity library. Using the appropriate interpolation tools, the resulting grid of models is then employed to assign pulsation parameters to each simulated red giant star in a synthetic population.

In the grid presented here, we covered the range $0.6 \leq M/\mathrm{M}_\odot \leq 7.0$, with the following sampling:

$$\begin{aligned} M/\mathrm{M}_\odot &\in [0.6, 1.0] \quad \text{in steps of} \quad 0.05\,, \\ M/\mathrm{M}_\odot &\in]1.0, 2.0] \quad \text{in steps of} \quad 0.1\,, \\ M/\mathrm{M}_\odot &\in]2.0, 7.0] \quad \text{in steps of} \quad 0.2\,. \end{aligned}$$

The grid covers luminosity values in the range $2.5 \leq \log(L/\mathrm{L}_\odot) \leq 5.0$. It is clear, however, that the more massive stars begin their TP-AGB evolution with a higher luminosity than the less massive ones.

Therefore, the starting luminosity for the computation of series of pulsation models has to depend on mass.

We derived an approximate analytic function to describe this dependence from `COLIBRI` evolutionary tracks. The functional form is the following:

$$\frac{L_{\mathrm{low}}(M)}{\mathrm{L}_\odot} = 3882 \cdot \frac{M}{\mathrm{M}_\odot} - 9294\,. \tag{4.50}$$

For masses lower than $\sim 2.5\,M_\odot$, the above function predicts values smaller than $\log(L/L_\odot) = 2.5$, the lower limit of the grid. In those cases, the starting luminosity was set at $\log(L/L_\odot) = 2.5$.

Most of the luminosity sequences for masses smaller than $\sim 3\,M_\odot$ are truncated below the upper luminosity limit $\log(L/L_\odot) = 5.0$. This is due to the fact that, for high values of L/M, the fundamental mode becomes strongly non-adiabatic, and the pulsation code is not able to compute it.

The resulting coverage in the M-L plane, compared with TP-AGB evolutionary models, is shown in Fig. 4.9. The grid, thus, is widely representative of the luminosity interval experienced by TP-AGB stars.

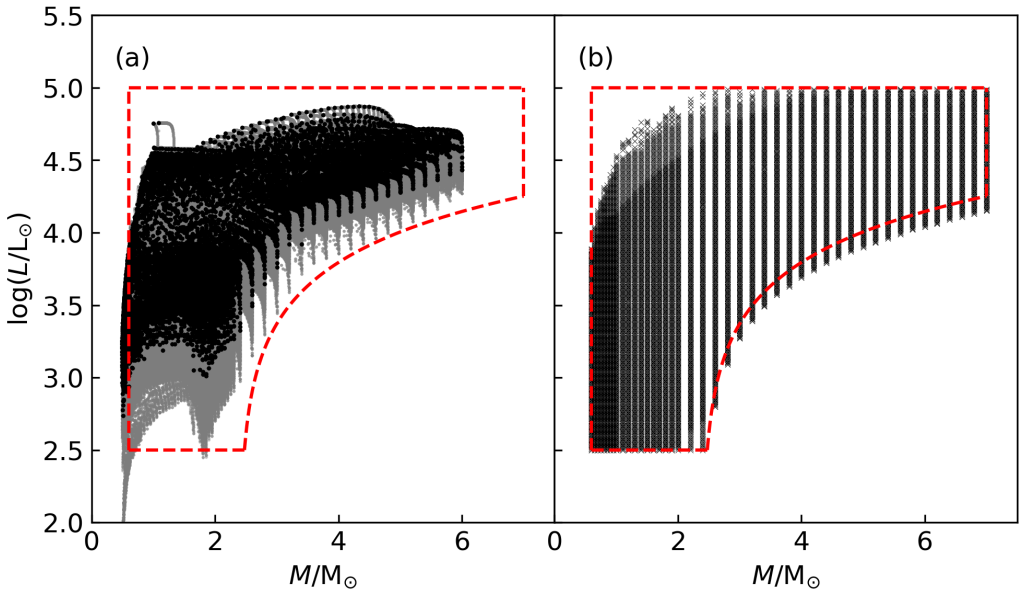

Figure 4.9: Panel (a): distribution of TP-AGB evolutionary tracks on the M–$\log(L)$ plane. Grey symbols in background represent full evolutionary models (including thermal pulses), while black symbols represent only quiescent points in the same evolutionary tracks. Panel (b): grid coverage in the M–$\log(L)$ plane. Each symbol represent a pulsation model. Dashed contours in both panel represent the nominal coverage. The lack of models in the upper-left portion is due to the spontaneous termination of low-mass sequences of pulsation models at luminosities lower than $\log(L/L_\odot) = 5.0$.

Core Mass-Luminosity Coverage

A common approach in modelling AGB evolution consist in the assumption of a core mass-luminosity relation. A number of different prescription for such a relation can be found in literature (Wood and Zarro, 1981; Boothroyd and Sackmann, 1988, *e.g.*).

However, the use of these relations is often inappropriate, such as in the case of Hot-Bottom Burning or in phases of the thermal pulse cycle other than quiet H-shell burning.

Nonetheless, values of the core mass have to be restricted to a realistic range that naturally has to depend upon luminosity.

Therefore, we assumed a luminosity-dependent range of core mass. The upper and

lower limit of that range are described by two core mass nodes that are computed as a function of total luminosity.

Fig. 4.10 shows the region of the core mass-luminosity plane where COLIRBI TP-AGB evolutionary models are located.

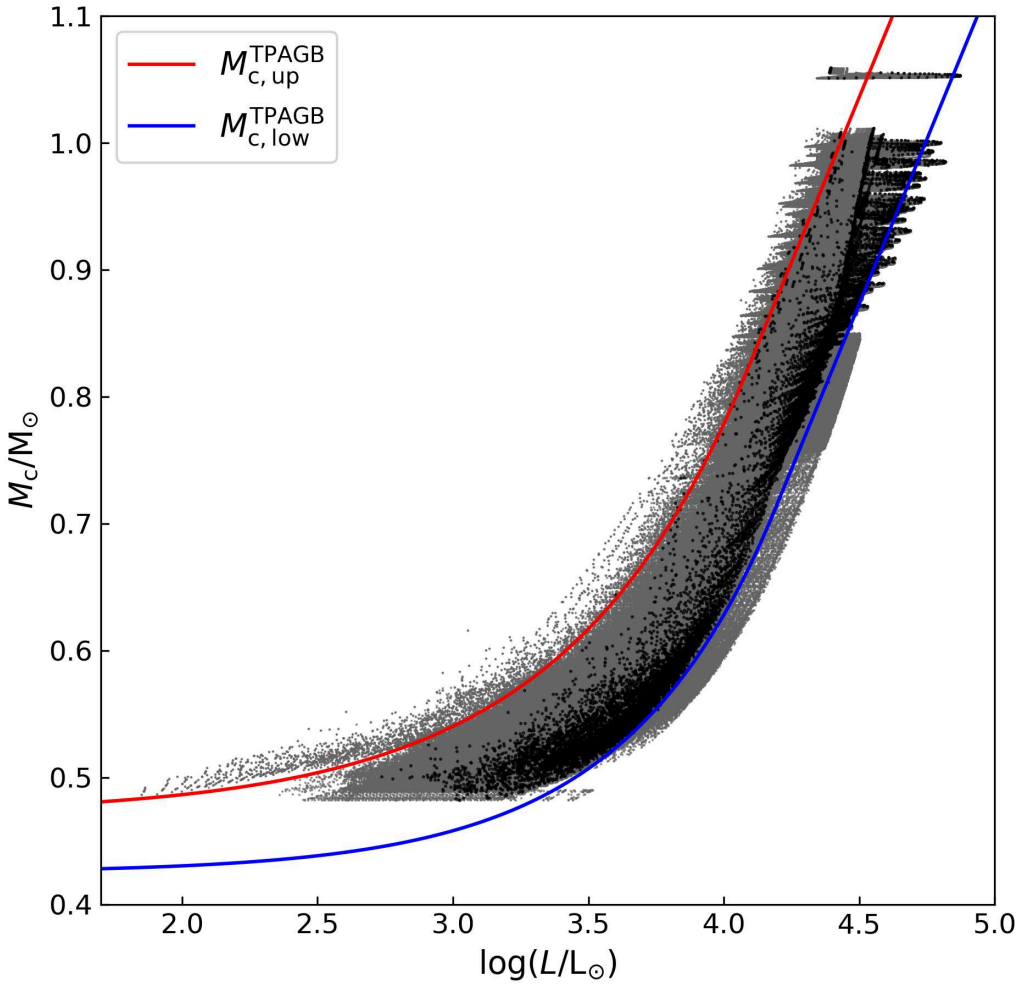

Figure 4.10: TP-AGB evolutionary models computed with the COLIBRI code, in the core mass-luminosity plane. Grey dots in the background represent models including the full thermal pulse cycle, whereas black dots are quiescent phases. Solid lines represent the analytic relations for the upper (red) and lower (blue) limits of the region occupied by models.

At each luminosity, models can have values of the core mass within a rather wide interval. Our approach consisted in modelling the upper and lower boundary of that region in terms of two analytic functions of luminosity.

Both functions have the same form, and exhibit a linear dependence of M_c upon L at low luminosity, while at bright luminosity the dependence becomes logarithmic:

$$\frac{M_c^{TPAGB}}{M_\odot} = \begin{cases} a_1 + a_2 \cdot 10^{a_3 \cdot [\log(L/L_\odot) + a_4]} & \text{if } \log(L/L_\odot) < \ell \\ b_1 + b_2 \cdot [\log(L/L_\odot) + b_3] & \text{if } \log(L/L_\odot) \geq \ell \end{cases} , \tag{4.51}$$

where ℓ is the luminosity at which the dependence changes form. The values of the

Table 4.5: Coefficients of the functions describing the upper ($M_{\rm c,up}^{\rm TPAGB}$) and lower ($M_{\rm c,low}^{\rm TPAGB}$) boundaries of the region populated by TP-AGB evolutionary models in the $M_{\rm c}$–$\log(L)$ plane. See also Fig. 4.10.

	$M_{\rm c,low}^{\rm TPAGB}$	$M_{\rm c,up}^{\rm TPAGB}$
ℓ	4.19	4.08
a_1	0.425	0.4708
a_2	$9.425 \cdot 10^{-6}$	$2.293 \cdot 10^{-3}$
a_3	0.7884	0.6468
a_4	1.4964	−0.7103
b_1	−1.52	−1.279
b_2	0.5202	0.5202
b_3	0.1	−0.05

coefficient are shown in table 4.5.

Any TP-AGB model, even those not computed with the same evolutionary code, is very likely to have the core mass being between those limits.

Therefore, it is straightforward to compute the pulsation parameters from the grid by linear interpolation over the values of the core mass.

This approach has been tested by comparing periods and growth rates obtained by interpolation on core mass with those resulting from actual pulsation models at the same value of core mass (figure to be added).

The results show that both periods and growth rates exhibit an almost perfectly linear dependence upon core mass, although the slope obviously depend upon the other stellar parameters and differ between distinct pulsation modes.

This guarantees the validity of our approach, and also means that extrapolation towards higher or lower core masses is in general safe.

4.9 Properties of Pulsation Models

A detailed analysis of the grid of pulsation models will be presented in a forthcoming paper (Trabucchi et al., in prep.).

We limit the discussion here to a few relevant properties resulting from the inclusion of updated opacity data, consistent with the chemical mixture of the envelope.

In Fig. 4.11 we show the value of the fundamental mode pulsation constant,

$$\frac{Q_0}{\rm days} = \frac{P_0}{\rm days} \left(\frac{M}{\rm M_\odot}\right)^{1/2} \left(\frac{R}{\rm R_\odot}\right)^{-3/2} , \tag{4.52}$$

as a function of $Z_{\rm ref}$ and C/O.

The pulsation constant represents the periods normalised to the mean stellar density, allowing us to investigate in more detail the dependence on periods of changes in the chemical composition.

The pulsation constant increases with metallicity, but shows essentially no dependence upon C/O in O-rich models (C/O < 1).

Approaching the value C/O = 1, a slight dependence on C/O appears, with the pulsation constant decreasing with C/O, but only at $Z_{\rm ref} \gtrsim 0.004$.

There is a clear change in trend as a model changes from O-rich to C-rich. Indeed, the pulsation constant exhibits a clear dependence on C/O for C-rich models, showing an increase with C/O.

Again, the dependence is stronger at higher metallicity, and tends to become more mild towards higher values of C/O.

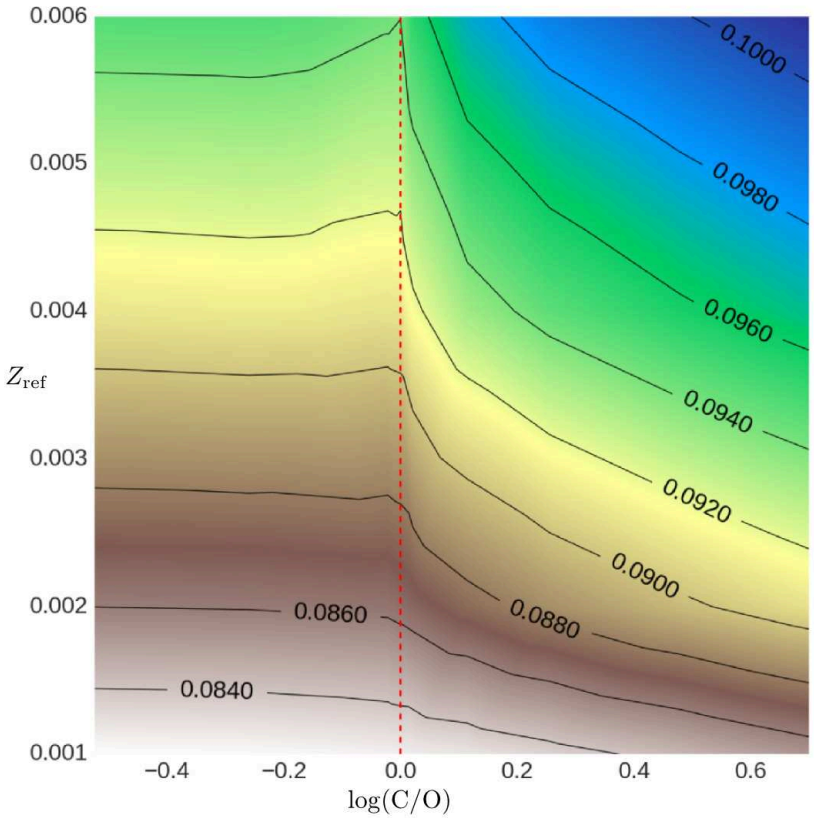

Figure 4.11: Contour levels of equal fundamental mode pulsation constant as a function of reference metallicity and C/O. In O-rich models (C/O < 1) the pulsation constant increases with metallicity and is essentially independent on C/O. Approaching the transition C/O $= 1$ (red dashed line) the pulsation constant tends to slightly decrease with C/O, although the effect is relevant only for $Z_{\rm ref} \gtrsim 0.004$. C-rich models, on the other hand, show a clear increase of the pulsation constant with increasing C/O. Again, the dependence becomes stronger towards higher metallicity.

4.9.1 Fitting Relations for the Periods: Preliminary Implementation in Isochrones

The new pulsation models presented in the previous sections have manifold applications, one of which is to implement realistic prescription of pulsation periods in isochrones and evolutionary tracks including the AGB phase.

Detailed prescriptions are going to be soon included in `COLIBRI` models. As a preliminary work towards this step, we derived simple period-mass-radius relations from pulsation models, and implemented them into `PARSEC-COLIBRI` as part of a recent, global update (Marigo et al., 2017).

Table 4.6: Coefficients for the periods in Eq. 4.53.

m	T	a	b	c	d
0	O	−0.683	1.874	−0.109	−1.957
0	C	−0.757	2.018	−0.121	−2.282
1	O	−0.585	1.620	0.083	−1.641
1	C	−0.499	1.515	0.107	−1.406

LPV properties were introduced in `PARSEC-COLIBRI` isochrones for the first time in Marigo et al. (2008), using a series of fitting relations derived from Fox and Wood (1982), Wood et al. (1983b) and Ostlie and Cox (1986) to describe periods in the fundamental and first overtone modes (P_0 and P_1 respectively), as well as luminosity at which the dominant period changes between these modes.

They have been used in many works for comparisons with observed periods in Local Group galaxies and star clusters.

In summary, we have computed fitting formulae for the predicted P_0 and P_1, of the form:

$$\log\left(\frac{P_n^{\rm T}}{\rm days}\right) = a\log\left(\frac{M}{\rm M_\odot}\right) + b\log\left(\frac{R}{R_\odot}\right) + c\log\left(\frac{M_{\rm env}}{M}\right) + d\,, \tag{4.53}$$

where n is the radial order of the mode (0/1 for fundamental/first overtone) and T is the chemical type (O- or C-rich).

The fitting coefficients are presented in Table 4.6. These relations where derived from models along `COLIBRI` evolutionary tracks covering the $Z_{\rm i}$ interval from 0.002 to 0.017, and for masses between 0.8 to 2.6 $\rm M_\odot$.

The fitting relations provide periods accurate to within a few per cent. The likely transition luminosity between the first overtone to fundamental mode was computed in the same way as in Marigo et al. (2008), based on Ostlie and Cox (1986).

Importantly, P_0 and P_1 pulsation periods are computed along the isochrones but the periodic changes in the photometry are not taken into account.

Therefore, the photometric properties we provide should be regarded as *mean properties* over the LPV pulsation periods, rather than instantaneous values.

Although preliminary, this method allowed us to have a first idea of the complex behavior of pulsation periods expected as stars evolve along the upper part of the HR diagram: In general, in the isochrone TP-AGB sections, pulsation periods change from point to point, according to equation 4.53, thanks to the large changes in M, L, $T_{\rm eff}$, and $\{X_i\}$, both between isochrones and inside thermal pulse cycles (TPC) of single isochrones.

Although the pattern of these changes can be rather complicated, a few general trends can be drawn with the help of Fig. 4.12. There, examples of isochrones from Marigo et al. (2017) are shown. In particular, Fig. 4.12 shows how luminosity, effective temperature, and the fundamental and first overtone periods change as a function of initial mass for an intermediate age isochrone (2 Gyr, left panels) and a much younger one (0.1 Gyr, right panels).

Selected points along the isochrones are colour-coded according to the surface value of C/O, showing the transition from spectral type M (blue symbols) to carbon stars (red symbols), going through the S-type stars (white symbols).

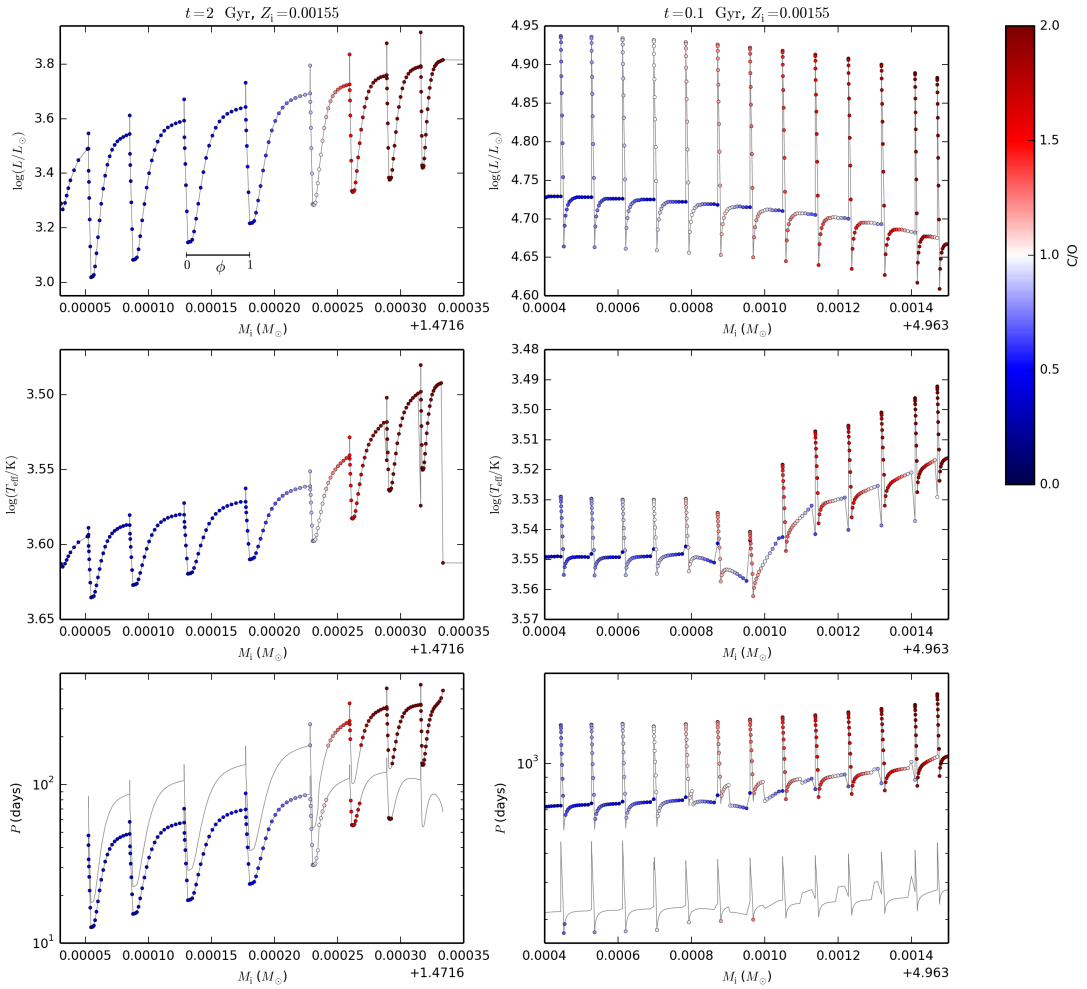

Figure 4.12: Examples of `PARSEC-COLIBRI` isochrones (Marigo et al., 2017). Panels shows the variation of luminosity, effective temperature and pulsation period (from top to bottom) as a function of initial stellar mass. Symbols are color coded according to C/O, showing the transition from M- to S- to C-type stars. In the bottom panels, both the fundamental and the first overtone modes are shown (the grey lines with longer and shorter periods, respectively). Only the mode expected to be dominant is marked by colored symbols.

At low luminosities and relatively high $T_{\rm eff}$, the dominant pulsation mode is the first-overtone one, of shorter period. Most isochrone TP-AGB sections will start with this dominant mode. Later along the isochrone, a transition to a dominant fundamental mode (longer period) can occur.

As illustrated in the bottom panels of Fig. 4.12, the transition happens along a few TPCs. In the isochrones of intermediate-age populations, the transition from first-overtone to fundamental mode often coincides with the main transition from O- to C-rich phases, where a marked reduction of the $T_{\rm eff}$ takes place (Marigo, 2002; Marigo and Girardi, 2007); whenever this happens, however, there are always small C-rich sections expected to appear in the first-overtone, as there are O-rich sections expected in the fundamental mode.

For younger isochrones where the TP-AGB develops at high luminosities and cool effective temeperatures, larger sections of the isochrones appear with a dominant fundamental mode. This includes most of the stars undergoing HBB, with their characteristic high L and low C/O ratio.

In reality, as we have seen, the situation is more complex with stars appearing in multiple pulsation modes and in higher-order overtones. Future releases of the `PARSEC-COLIBRI` isochrones will take into account the more complete modeling and interpolation described in this work.

4.10 Combination with Population Synthesis

The grid of pulsation models can be used to estimate pulsation properties of models of luminous red giant stars from their global parameters.

We developed a tool to perform this operation on the output of a stellar population synthesis tool.

This is done by means of multi-linear interpolation over the following stellar parameters:

1. total luminosity: $\log(L/{\rm L}_\odot)$,
2. effective temperature: $\log(T_{\rm eff}/{\rm K})$,
3. total mass: $M/{\rm M}_\odot$,
4. core mass: $M_{\rm c}/{\rm M}_\odot$,
5. hydrogen abundance by mass fraction: X,
6. metallicity by mass fraction: Z,
7. carbon-to-oxygen ratio: C/O.

The procedure is summarised in the present section, and discussed in more detail in Appendix A.

It is worth to recall the few basic assumption the procedure relies upon. Pulsation takes place in the stellar envelope, which are effectively decoupled from the core from a dynamical point of view, at least during quiescent TP-AGB evolution (*i.e.*, most of the lifetime of TP-AGB stars).

Therefore, only the envelope has been modelled in the construction of the grid, assuming it to be chemically homogeneous as a consequence of efficient convective mixing.

In contrast, the core region (that we simply call "the core") is not modelled. It includes the compact CO core as well as any energy source, *i.e.*, the H-burning or He-burning shell, whichever is assumed to be active.

This means that the entire energy output of the star (the total stellar luminosity L) originates in the core, *i.e.*, the radial profile of luminosity is flat, $L(r) = L$.

This is consistent with the existence of a (broad) core-mass luminosity relation. Core mass values in grid models are connected with luminosity as discussed in section 4.8.1.

Models were computed including variations of the abundance of carbon (*i.e.*, non-scaled-solar mixtures), and opacities consistent with the envelope composition.

Both oxygen and nitrogen have been kept fixed to the scaled-solar value. Thus the reference metallicity (required to identify interpolation nodes in the grid) can be computed from the input value of true metallicity using Eq. 4.49.

Our tool, written in FORTRAN 90, reads input parameters from a suitable file in a table format, where each row correspond to a different combination of global parameters, *i.e.*, to a different stellar models.

In other words, it is compatible with typical output from stellar evolution or population synthesis codes.

There is no restriction on the size of the input file. Also, there is no strict requirement on the order of the input columns, as long as there is one corresponding to each input parameters.

If the columns corresponding to the input parameters are not sorted according to the list above, the user is required to pass the number of the corresponding columns as argument from command line as the interpolation tool is launched.

There is however a requirement on commented text in the input file: the first line has to be commented (with a # symbol) and should contain the legend for the file's columns.

The output consist of a copy of the input file, where interpolated pulsation data are appended to each row. A piece of legend for the new columns is also appended to the original first line of the input file. New data consist of:

1. adiabatic period: $\log(P_{\rm ad}/{\rm days})$,
2. non-adiabatic period: $\log(P_n/{\rm days})$,
3. growth rate: GR_n,

for each one of the specified $N_{\rm modes}$ (up to 5 for the current grid).

A final quantity is also provided, that is a flag used to assess the validity of the interpolation procedure. It is a seven-digit string, each digit corresponding to one of the input parameters (in the same order as the list at the beginning of the chapter). Digits can assume one of the following values:

- `0`: it means interpolation was performed correctly in the corresponding parameter;
- `1`: it means the value of the corresponding input parameter is outside of the grid, (too small) and the code extrapolated towards smaller values;
- `2`: it means the value of the corresponding input parameter is outside of the grid, (too large) and the code extrapolated towards higher values.

In general, provided that the input values are not too far out of the grid's range, extrapolation can be considered safe both upward and downward, except for luminosity. A number of tests suggest that extrapolation to luminosities higher than the grid's limits may give unreliable results, and should be treated carefully.

On the other hand, the dependence of periods and growth rates upon the core mass has been thoroughly tested, and appears to be very close to linear and generally weak. For this reason, we expect the application of our interpolation scheme to RGB models to be generally safe (see also section A.2).

Chapter 5

Application: Long-Period Variables in the Large Magellanic Cloud

The Large Magellanic Cloud is the ideal environment to examine long-period variables from the perspective of stellar population studies.

Indeed, it hosts a large number of LPVs in the RGB or AGB evolutionary phase. The fact that all of them can be considered to lie at the same distance from us significantly simplifies the analysis.

Period-luminosity sequences of long-period variables are commonly interpreted as different pulsation modes, but there is disagreement on the modal assignment.

Here, we re-examine the observed PL sequences in the Large Magellanic Cloud, including the sequence of long secondary periods (LSPs), and their associated pulsation modes.

To this aim, we make use of the grid of linear, radial, non-adiabatic pulsation models presented in section 4.8, and combine it with a population synthesis model as described in section 4.10.

Then, we use a semi-empirical approach to assign modes to the pulsation sequences by exploiting observed multi-mode pulsators.

As a result of the combined approaches, we consistently find that sequences B and C′ both correspond to first overtone pulsation, although there are some fundamental mode pulsators at low luminosities on both sequences.

The masses of these fundamental mode pulsators are larger at a given luminosity than the mass of the first overtone pulsators.

These two sequences B and C′ are separated by a small period interval in which large amplitude pulsation in a long secondary period (sequence D variability) occurs, meaning that the first overtone pulsation is not seen as the primary mode of pulsation.

Observationally, this leads to the splitting of the first overtone pulsation sequence into the two observed sequences B and C′.

Our two independent examinations also show that sequences A′, A and C correspond to third overtone, second overtone and fundamental mode pulsation, respectively.

5.1 Introduction and Context

Luminous red giants are known to be variable, and their periods of observed variability lie on well defined sequences in period-luminosity (PL) diagrams. Wood et al. (1999) and Wood (2000) identified five sequences (labelled A, B, C, D and E) in the PL diagram of the Large Magellanic Cloud (LMC) using observations from the MACHO project.

Ita et al. (2004a) found that sequence B is in fact two sequences, B and C′, while Soszyński et al. (2004) showed that an additional sequence exists on the short-period side of sequence A. They labelled that sequence a_4, although we use here the alternative designation A′, as in Wood (2015) and references therein. Moreover, sequences A and B, and possibly A′, each consist of three or more closely spaced sequences (Soszyński et al., 2004, 2007).

Here, we are interested in sequences A′, A, B, C′ and C, which are attributed to pulsating stars. All these long period variables (LPVs) can be either on their red giant branch (RGB) or asymptotic giant branch (AGB) phases, with just a slight offset between the respective period distributions (Ita et al., 2002; Kiss and Bedding, 2003). Sequence D consists of long secondary periods (LSPs), while sequence E is due to binary stars. We do not discuss sequence E further in this work.

Existing interpretations of the observed sequences A′, A, B, C′ and C all assume that these sequences correspond to distinct and adjacent radial orders of pulsation.

There are two incompatible interpretations in the literature (already discussed in some detail in section 2.2.4). Wood (2015) assumed that sequence C, containing the Mira variables, corresponded to the radial fundamental mode so that sequences C′, B, A and A′ corresponded to the radial 1st, 2nd, 3rd and 4th overtones, respectively. On the other hand, Mosser et al. (2013) and Soszyński et al. (2007) matched sequences B and A to the 1st and 2nd radial overtones, meaning that sequence C′ is the fundamental mode and that sequence C has no explanation. Note that there is a one sequence offset between the above two sets of mode assignments.

A solution to the above mode assignment incompatibility is to relax the requirement that the adjacent observed sequences correspond to adjacent radial modes of pulsation, where we identify radial order $n = 0$ with the fundamental mode, radial order $n = 1$ with the 1st overtone (1O) mode, and so on.

Here, we explore the possibility that sequence B corresponds to 1O mode pulsation as suggested by Mosser et al. (2013), sequence C corresponds to radial fundamental mode pulsation as required by Wood (2015), but that sequence C′ is associated with 1O or fundamental radial mode, or both these modes.

To do this, we firstly construct theoretical pulsation sequences and compare them with observations, following which we take an independent semi-empirical approach and examine observations of stars exhibiting multiple periods.

5.2 Period-Luminosity Relations in a Population Synthesis Model

5.2.1 Methods

We used the code `TRILEGAL` (Girardi et al., 2005) to compute a synthetic stellar population representative of the LMC, assuming a constant star formation rate from ages

$\sim$ 5Myr to $\sim$ 10Gyr and the age-metallicity relation by Pagel and Tautvaišienė (1999).

Such a simplifying assumption is made to eliminate discontinuities that could be caused by periods of reduced or null star formation. The technical details of such simulations are discussed elsewhere (Pastorelli et al., in prep.).

Here, it suffices to recall that the simulations include single stars in all relevant evolutionary phases, as extracted from the `PARSEC` (Bressan et al., 2012) and `COLIBRI` (Marigo et al., 2013) grids of stellar evolutionary tracks.

As to the AGB phase, stellar models account for the formation of carbon stars due to the third dredge-up, as well as for the occurrence of hot-bottom burning (Marigo et al., 2017).

The simulation output includes many intrinsic stellar quantities such as luminosity, radius, core mass, surface abundances, and evolutionary stage, as well as the apparent photometry.

We then used the radial, non-adiabatic pulsation models described in Wood and Olivier (2014) and Trabucchi et al., in prep. (see also section 4.8), to assign periods and growth rates for five radial modes to each simulated RGB or AGB star.

Models include detailed atomic and molecular opacities (Marigo and Aringer, 2009) for a realistic description of carbon stars. The growth rates provide an indication of the stability of pulsation modes: a mode having a negative growth rate should be stable, while a positive growth rate means a mode is excited.

In a given stellar model, we call the *dominant* mode the one with the largest growth rate, and it is also expected to have the largest amplitude.

5.2.2 Comparison with Observations

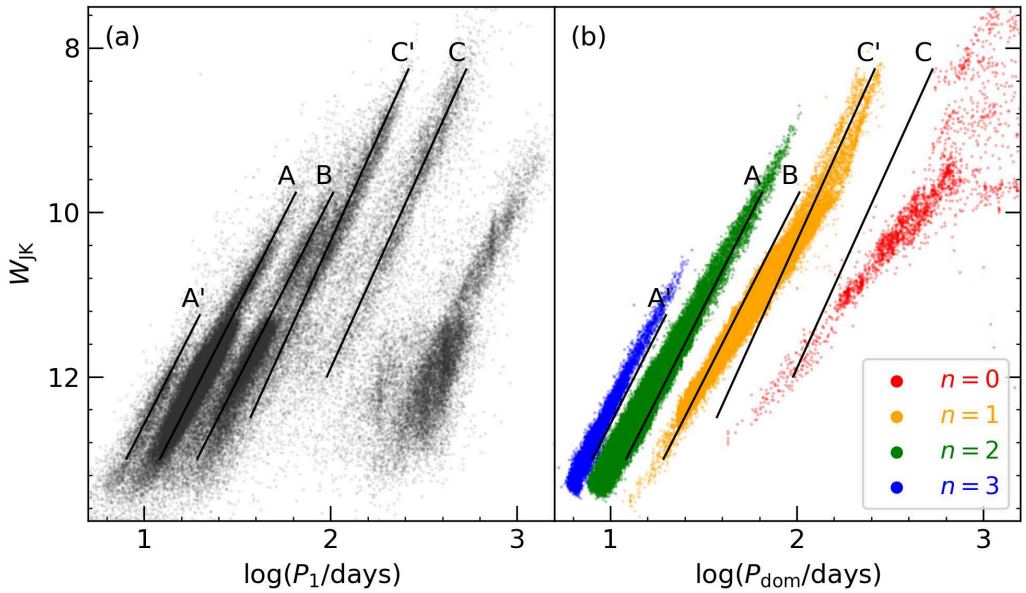

Figure 5.1: Observed primary periods (panel (a)) are compared to theoretically dominant periods obtained from radial, linear, non-adiabatic models (panel (b)). Different colours represent periods of different modes: red for fundamental mode, orange for 1O, green for 2O mode, blue for 3O mode. Solid lines provide a visual aid to identify the approximate location and slope of observed sequences.

We compare the results with observations using data from the OGLE-III Catalogue of LPVs in the LMC (Soszyński et al., 2009) combined with near-infrared photometry from the Two Micron All Sky Survey (2MASS) Point Source Catalogue (Skrutskie et al., 2006).

The comparison is made in the $\log(P)$-$W_{\rm JK}$ plane, where the Wesenheit index defined as

$$W_{\rm JK} = K_{\rm s} - 0.686(J - K_{\rm s}) \tag{5.1}$$

is a reddening-free measure of the luminosity. The advantage of using a Wesenheit index is that the PL sequences of LPVs become even better defined, as immediately clear when comparing, for instance, a $K_{\rm s}$-$\log(P)$ diagram with a $W_{\rm JK}$-$\log(P)$ one (see, *i.e.*, Fig. 2.8).

On the other hand, it must be employed with some care, as various stellar properties, including some related with pulsation, depend on stellar colors (see, *i.e.*, Feast et al., 1989). Such a color term should be properly accounted for when one intends to provide a quantitative analysis or description of observed variability properties, especially since uncertainties exist regarding the circumstellar reddening law, and it is likely not the same for O-rich and C-rich stars.

However, in the present work we are rather interested in pulsation properties from a qualitative point of view, and in a global comparison between theory and observations. Thus, the color term is expected to be too small to affect our conclusions.

Long-period variables are often multi-periodic. To account for this, three different periods for each star are included in the OGLE-III Catalogue.

The three observed periods of each variable have different importance. The one corresponding to the highest peak in the power spectrum is assumed to be the most significant one (for a more detailed description of the classification, the reader is referred to Soszyński et al., 2009, and references therein).

It is classified as primary mode, and is usually the one with the largest amplitude in each star. It is also assumed to be the one subject to the largest driving, *i.e.*, it should correspond to the theoretical mode with the largest growth rate.

The two other periods, if not resulting from spurious detection, are excited modes with smaller growth rates. They are called secondary and tertiary periods, (or simply secondaries).

We use periods derived from radial, non-adiabatic models, and compare the dominant mode in the models (the one with the highest growth rate) to the observed primary modes in the OGLE data.

Theoretical modes having a positive but small growth rate are not expected to be observed, therefore only dominant modes with a growth rate larger than 0.04 are shown, where the growth rate is the fractional growth in amplitude per period as defined by Wood and Olivier (2014). The comparison is shown in Fig. 5.1.

We find the models to be in reasonably good agreement with observations. The observed sequences can be explained with exactly four radial oscillation modes, from the fundamental to the 3O mode. The radial 4O mode, also computed for the simulation, is never predicted to be dominant, and is not required to reproduce the observations.

Sequences A′ and A are fairly well reproduced by radial 3O and 2O mode periods, respectively, although in both cases the theoretical sequences are slightly offset towards short periods with respect to observed ones.

When the radial 1O mode is dominant, it has periods extending across both sequences B and C′. However, there is no theoretical counterpart in the models for the

gap between the two sequences (this will be discussed in Section 5.3.3).

Dominant fundamental periods are distributed mainly to the right of sequence C, and are not as a good match to the observations as are the overtones. However, according to the models, the fundamental mode is the only mode possibly responsible for sequence C, as no other mode can reach such long periods.

The reasons for the poor agreement between the positions of sequence C and the positions of predicted fundamental mode pulsators are explored further in Section 5.2.3.

Some of the brightest O-rich stars observed in the LMC are undergoing HBB. However, they are too few to draw any conclusion based on a comparison of models with observations. This is especially true given the difficulties in reproducing the region of the PLD at long periods and bright magnitudes. Therefore, HBB stars won't be further discussed in the present work.

5.2.3 Amplitudes and Growth Rates

Here, we examine observed amplitudes to interpret LPVs in terms of different pulsation modes. In panel (a) of Fig. 5.2, the distribution of observed amplitudes[1] is shown against the variable $\log(P_{W_{\rm JK}=12})$ defined by

$$\log(P_{W_{\rm JK}=12}) = \log(P) + \frac{W_{\rm JK} - 12}{4.444}\,, \tag{5.2}$$

which represents $\log(P)$ projected along a line parallel to the observed sequences until it meets the level $W_{\rm JK} = 12$. This way, periods on a given sequence are bounded to the same horizontal range (see also Wood, 2015).

Similarly to what happens in the PL diagram, where observations lie on well defined sequences, in Fig. 5.2 observed modes are distributed into four distinct groups, that are actually period-amplitude-luminosity (PAL) relations (luminosity plays a role through the dependence of $\log(P_{W_{\rm JK}=12})$ upon $W_{\rm JK}$ in Eq. 5.2).

At short periods ($\log(P_{W_{\rm JK}=12}) \lesssim 1.2$), the cluster of observed modes of small amplitude is the counterpart of sequence A′, while the one with $1.2 \lesssim \log(P_{W_{\rm JK}=12}) \lesssim 1.4$, and extending up to larger amplitudes, corresponds to sequence A.

Towards long periods, clusters become elongated and slanted. The one starting at $\log(P_{W_{\rm JK}=12}) \simeq 1.4$ with small amplitude, corresponding to sequence B, culminates at larger amplitude at $\log(P_{W_{\rm JK}=12}) \simeq 1.6$, where it is the counterpart of the bright end of sequence C′.

Finally, the faint end of sequence C′ corresponds to the clump at small amplitude at $\log(P_{W_{\rm JK}=12}) \simeq 1.6$, which extends to larger amplitudes at $\log(P_{W_{\rm JK}=12}) \simeq 1.9$, corresponding to sequence C. It then shows a tendency to bend back to the short period side of sequence C at the largest amplitudes, corresponding to Miras, whose amplitude is limited by nonlinear effects.

In the previous subsection, we showed that the region occupied by the sequences in the PL diagram is also reproduced by exactly four radial modes. This suggest that the four PAL relations can be identified with radial modes from the fundamental to the 3O. To support this hypothesis, we use theoretical growth rates as a proxy for mode

[1] Amplitude data in the OGLE3 catalogue comes rounded to the third decimal digit. As a consequence, visual inspection of low-amplitude distributions in log-scale is virtually impossible. For this reason, we added random errors with a standard deviation of $7.5 \cdot 10^{-4}$ mag to amplitude data, making their distribution visually smooth in Fig. 5.2.

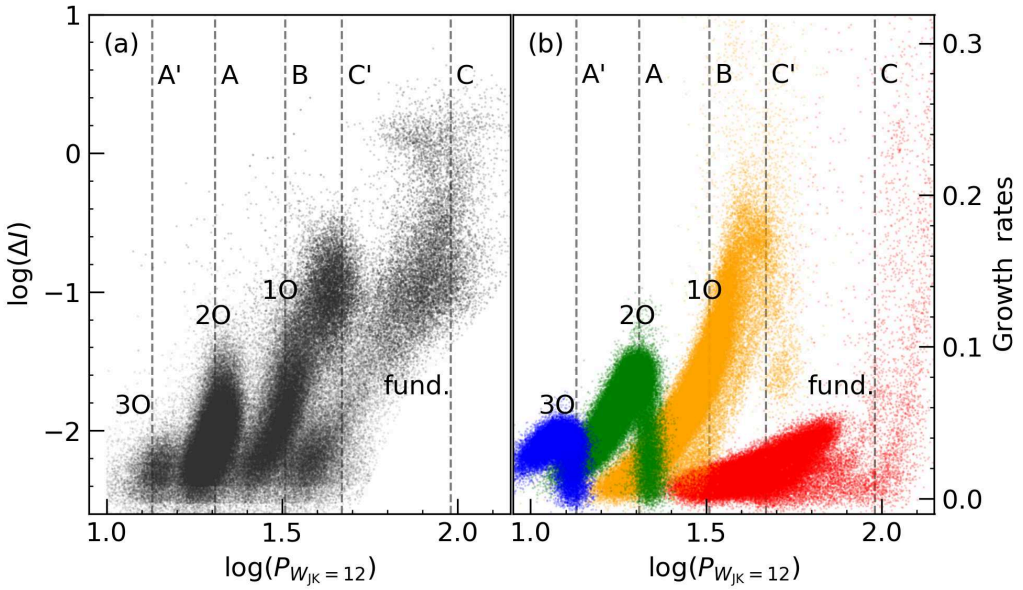

Figure 5.2: Panel (a): logarithm of observed I band amplitudes, for all three periods of stars in the OGLE3 catalogue, as a function of $\log(P_{W_{\rm JK}=12})$. The distinct PAL relations are labelled with the corresponding mode according to the interpretation provided here (see text). Periods on sequence D and longer than sequence C have been ignored, as they are not related to the normal modes of pulsation (see Section 5.3.1). **Panel (b):** theoretical growth rates for all excited modes up to the 3O, labelled and colour coded according to their radial order as in Fig. 5.1. Vertical dashed lines in the background of both panels approximately identify the centre of the PL sequences.

amplitude in order to make a comparison with the observed distribution of amplitudes, as shown in panel (b) of Fig. 5.2.

The distribution of growth rates there exhibits a characteristic behaviour typical of the evolution of pulsational stability in luminous red giants (this will be discussed in section 5.3.2, see also Fig. 5.6, and Fig. 4.4 in section 4.4).

At short periods, the 3O mode is dominant (has the largest growth rate) and its period falls in the vicinity of sequence A′. With further evolution, its growth rate drops, forming the vertical strip at $\log(P_{W_{\rm JK}=12}) \simeq 1.1$.

The 2O mode shows the same behaviour with changing $\log(P_{W_{\rm JK}=12})$. For the 1O mode, the growth rate rises with $\log(P_{W_{\rm JK}=12})$ as for the 2O and 3O modes but the vertical strip corresponding to the growth rates dropping to negative values is absent.

The fundamental mode shows a different pattern, being stable or weakly unstable most of the time, and becoming suddenly very unstable (very large growth rates, like those at $\log(P_{W_{\rm JK}=12}) \gtrsim 2$).

In Fig. 5.2, the observed amplitudes seen in panel (a) and the predicted amplitudes seen in panel (b) describe an entirely similar pattern as long as only overtone modes are considered.

We interpret this agreement as a validation of our hypothesis to assign a different radial order of oscillation to each PAL relation. It also supports the idea that sequences B and C′ are both due to 1O mode pulsation.

The remaining PAL relation has periods longer than the 1O mode and is related

to sequence C, which is almost certainly due to fundamental mode pulsation (Wood, 2015). Thus, we identify it with the fundamental mode in spite of the poor agreement of models with observations.

Such a poor agreement is a consequence of the fact that the fundamental mode is generally well reproduced in terms of periods, but not of driving. We further explore this aspect in Section 5.3.2.

To show that the issue is limited to the modelling of driving, and to validate our identification of PAL relations with pulsation modes, in Fig. 5.3 we examine the distribution of *all* theoretical fundamental periods, regardless of their growth rates. We compare this distribution with the PAL relation of longest period (the one labelled "fund."), including primary, secondary and tertiary periods rather than only the primary periods.

Fundamental mode periods, both in the observations and in the models, cover not only the region of sequence C, but also a wide area including the faint part of sequences B and C′.

The global agreement found is a confirmation that fundamental mode periods are generally correct, although models show a rather clear tendency to overestimate them, especially towards higher luminosities.

It is important to discuss this result in some detail. It is obvious that all observed periods are due to excited modes, while, on the other hand, simulated periods are associated to both excited and stable fundamental mode. However, as discussed above, we are not able to reliably tell which when the fundamental mode is stable/excited in models.

Thus, assuming the underlying synthetic population model is a good description of the LMC, all observed fundamental mode periods are reproduced (statistically speaking) within the set of simulated ones. The fact that the distribution of theoretical periods is more bent towards longer periods than the observed one suggests that models tend to overestimate fundamental mode periods, an effect that increases with luminosity. On the other hand, theoretical fundamental mode periods beyond the right edge of the observed sequence C are not overestimated[2], but are rather modes that are probably stable, but not predicted to be so due to the shortcomings in the description of the driving mechanism (or possibly stabilised by some other effect not included in models).

To summarise, under the regime in which the fundamental mode is excited, its period is reasonably well reproduced (at least in terms of bulk distribution), although increasingly overestimated with increasing luminosity. The "plumes" of theoretical periods at $W_{\rm JK} \lesssim 10$ on the right of sequence C in Fig. 5.3, panel (b), showing poor agreement with observations, are partly due to overestimation of fundamental mode periods, but mostly to the fact that those modes are very likely stable, but not predicted to be so. In other words, they simply shouldn't be there.

[2]More precisely, they are probably overestimated, but that's not the main source of disagreement with observations.

5.3 Semi-Empirical Analysis of the Pulsation Sequences of LPVs

5.3.1 The Pulsation Modes Associated with the Observed PL Sequences

In this section, we examine the periods in the many multimode LPVs in the LMC. In Fig. 5.4 we show six $\log(P)$-$W_{\rm JK}$ diagrams for LPVs in the LMC. Black points in the background are observed primary periods, and form the approximately parallel PL sequences A′, A, B, C′ and C. The sequence identifications are shown on panel (a) of Fig. 5.4.

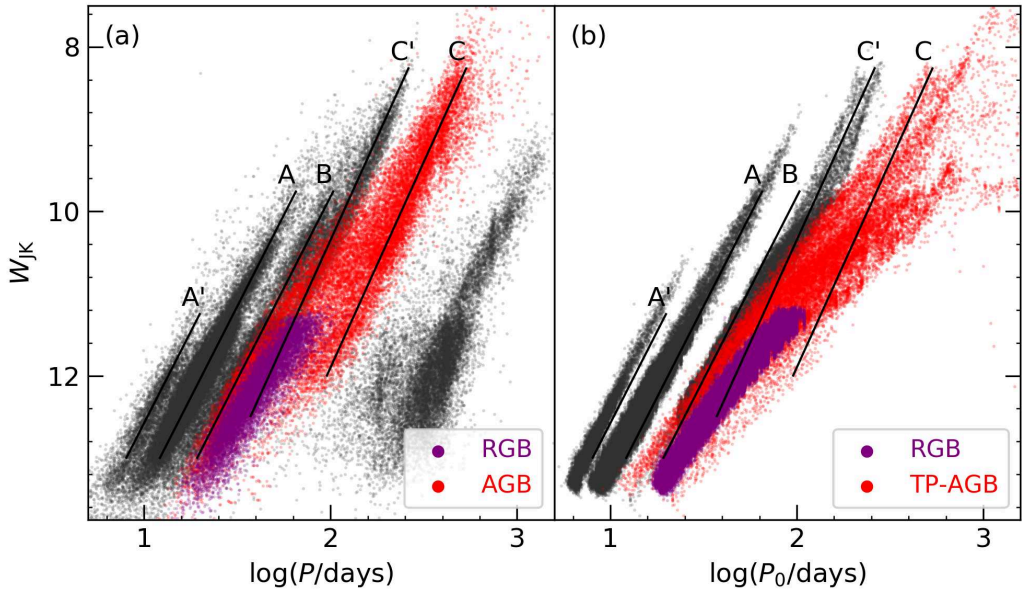

Figure 5.3: Panel (a). Each star in the OGLE3 Catalogue has three observed periods: primary, secondary and tertiary. Here, all of them are shown, provided that they belonging to the fourth amplitude group in Fig. 5.2 (labelled "fund."). They are shown as red or purple points if classified, respectively, as AGB or RGB stars (according to the OGLE evolutionary classification as in Soszyński et al. (2004)). As a reference, all primary periods are shown in the background as dark points (same as Fig. 5.1). **Panel (b).** Theoretical fundamental mode periods, regardless of their growth rates, shown in red if belonging to TP-AGB models and in purple if belonging to RGB models. Dominant overtone modes are shown as dark points in the background for reference.

Panel (a) of Fig. 5.4 shows the secondary and tertiary periods (green points) associated with stars whose primary periods (orange points) lie is a channel down the centre of sequence A. There are clearly three additional modes associated with those stars[3].

The most important point to note about panel (a) is that there are only two modes (green strips) with periods longer than the mode associated with sequence A (sampled by the orange strip).

[3]We ignore the broad area of green points on the long period side of sequence C which are a mixture of periods related to the presence of LSPs on sequence D and many other periods caused by the annual observing cycle for the OGLE data and possibly by convection-related variability.

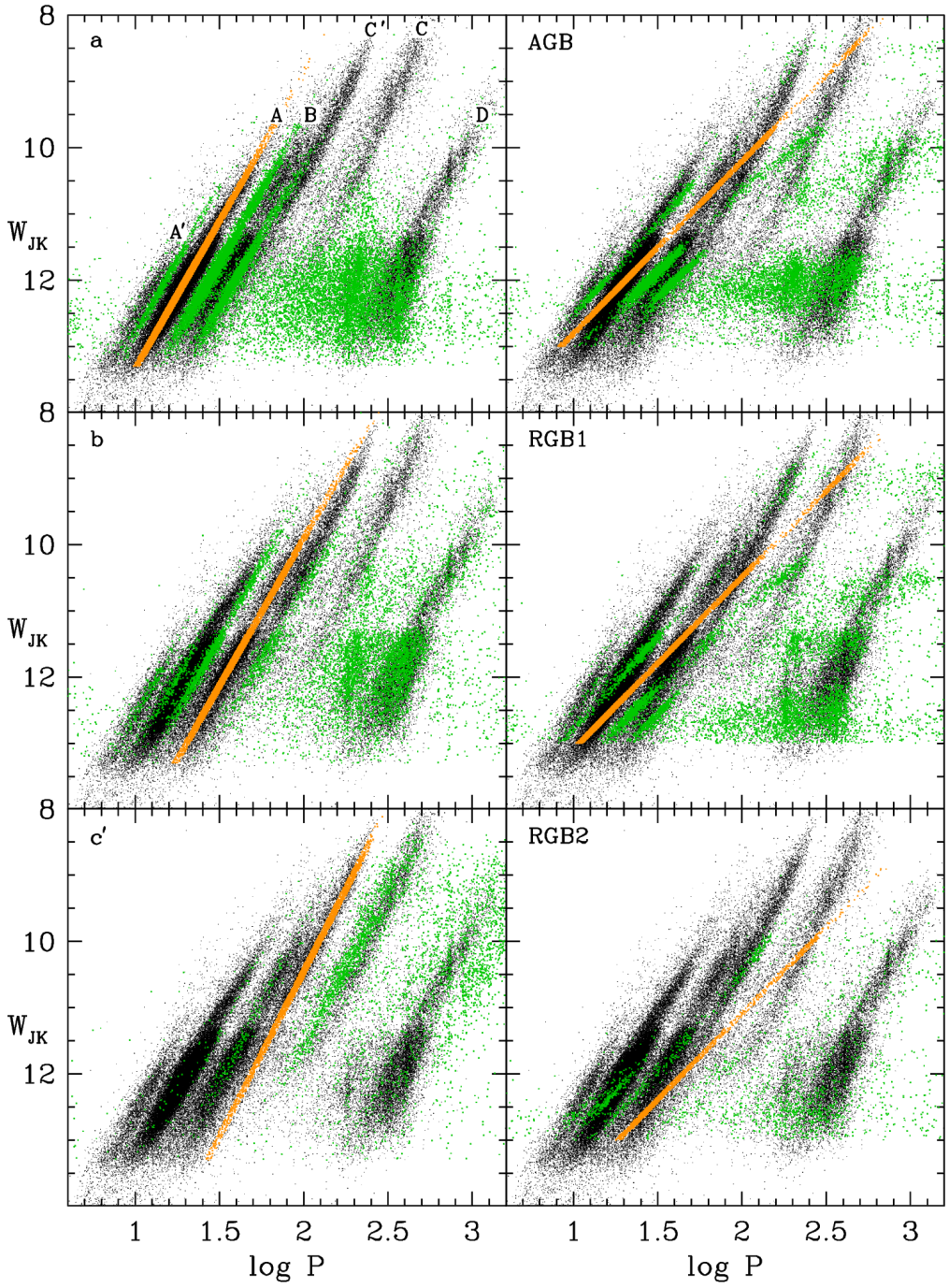

Figure 5.4: Plots of $W_{\rm JK}$ against $\log(P)$. Black points in each panel are the primary periods of each star. These points fall mostly on the six sequences labelled in panel (a). In the left three panels, a channel of small width centred on a sequence is defined and all primary periods in these channels are coloured orange. The secondary and tertiary periods of these stars are plotted as green points. In the right three panels, a sloping channel approximating an evolutionary track is defined and the same colour scheme is used for primary, secondary and tertiary periods.

Assuming the longest period mode corresponds to fundamental mode pulsation, then sequence A must correspond to second overtone (2O) pulsation.

There is one green strip in panel (a) with a period shorter than that of sequence A and this must correspond to the 3O mode of pulsation. Sequence A′, which is on the short period side of sequence A, should therefore also correspond to the 3O mode of pulsation.

Note that, for simplicity, we consider here only radial modes (angular degree $\ell = 0$), although nonradial modes are also present in LPVs. Indeed, dipole ($\ell = 1$) and quadrupole ($\ell = 2$) modes are present within sequences A and B and possibly A′, as discussed by Soszyński et al. (2004), Soszyński et al. (2007) and Wood (2015). Stello et al. (2014) analysed a sample of late K and early M type giants on the RGB which were observed by *Kepler* and they found their power spectra to be dominated by dipole modes for the 2nd and higher overtones, even for the most luminous stars in their sample.

This suggests that nonradial modes may also be dominant for the 2nd and higher overtones in LPVs in the OGLE sample, which overlaps in luminosity the sample used by Stello et al. (2014). Since the dipole and quadrupole periods are longer than the radial period of the same radial order, the dominance of the dipole mode could help explain why the predicted 3O and 2O periods for sequences A′ and A, respectively, in panel (b) of Fig. 5.1 are slightly shorter than the mean observed periods for these two sequences.

We are currently making nonradial pulsation models for LMC AGB stars in order to better understand the observed nonradial modes and their contribution to the period-luminosity sequences (Montalban et al., in prep).

Moving to panel (b) of Fig. 5.4, we see that for the stars whose primary period lies in sequence B, there is only one associated mode whose period is longer than the sequence B period. Once again, if this longer period mode is the fundamental mode, then the stars on sequence B which exhibit the longer period correspond to 1O pulsaton. This is consistent with a picture whereby the adjacent sequences A and B are associated with adjacent radial modes.

In panel (b), there appear to be three additional modes (green strips) shorter than the sequence B mode at low luminosities. These would be the 4O, 3O and 2O modes if all the stars on sequence B where 1O mode pulsators. However, this is not the case.

In the faint part of sequence B there are in fact two groups of stars, each with a different mass at a given luminosity. The first group consists of the 1O mode pulsators mentioned above. The second group consists of more massive stars whose primary period normally belongs to sequence A′ and which, by chance, have their longest period mode coinciding with sequence B, as shown by Wood (2015).

For these stars, the mode found on sequence B is the fundamental mode so that, at low luminosities, sequence B contains both 1O and fundamental mode pulsators. Normally, the latter group would have a primary period located on sequence A′ (the 3O mode), but sometimes the fundamental mode is detected as the primary pulsation mode, as both have rather small amplitudes.

Moving to panel (c′) of Fig. 5.4, we see that for the stars whose primary period lies in sequence C′, there is also one associated mode whose period is longer than the sequence C′ period, at least for AGB stars above the tip of the RGB at $W_{\rm JK} \approx 11.3$ and for some stars (possibly AGB stars) just below the RGB tip.

This indicates that for these stars, sequence C′ corresponds to 1O pulsation, just

like the luminous stars on sequence B. The longer period mode coincides with sequence C or its shorter period edge, consistent with the assumption that sequence C is made up of fundamental mode pulsators as argued by Wood (2015).

In addition to the sequence C′ stars exhibiting a longer secondary or tertiary period, there are some C′ stars at lower luminosities that exhibit a shorter period coinciding with sequence B. These are the analogs of the sequence B stars which have their fundamental mode on or to the long period side of sequence C′.

Thus, especially at RGB luminosities, sequence C′ contains some fundamental mode pulsators. As with sequence B, the fundamental mode pulsators on sequence C′ are more massive at a given luminosity than the 1O mode pulsators on this sequence. Note that sequence C′ is sparsely populated at low luminosities and it is poorly defined there.

We now have a picture in which sequences B and C′ are made up predominantly of 1O pulsators but at low luminosities they also contain fundamental mode pulsators of higher mass at a given luminosity. Note that this is consistent with the results of Section 5.2.3 based on the identification of PAL relations with the four lowest order pulsation modes.

In this situation, the idea that adjacent sequences correspond to adjacent radial orders of pulsation breaks down.

Another anomaly is that sequences B and C′ seem to be unusually close together in $\log(P)$. The longer period mode associated with sequence B stars has a period that is longer than the period of the adjacent sequence, C′.

For all other sequences, the secondary and tertiary periods form strips that are closer to their primary mode sequence than are the adjacent primary mode sequences. Wood (2015) argued that this is because the mass of stars at a given luminosity decreases in moving from sequence A′ through to C.

In this situation, and under the assumption that sequences B and C′ corresponded to adjacent radial orders, Wood (2015) tried to explain the unusually close positions of sequences B and C′ by assuming the sequences C′ and C were radial $\ell = 0$ pulsators but that sequences A′, A and B were dominated by nonradial $\ell = 1$ pulsators whose periods were slightly larger than those of the $\ell = 0$ pulsators.

If we relax the condition that sequences B and C′ coincide with adjacent radial orders, such a strong assumption is not necessary anymore, and we can safely assume the presence of dominant modes on sequences A′, A and B that are due to radial pulsation (although, as noted above, nonradial modes have a presence within these sequences).

In order to throw further light on the modes associated with the PL sequences, in the right hand panels of Fig. 5.4 we consider sloping channels in the $\log(P)$-$W_{\rm JK}$ diagram so that we can follow mode evolution in passing from one sequence to the next (see an example in Fig. 5.5). Remember that the orange points are primary modes (the largest amplitude) and the green points are the secondary and tertiary modes (smaller amplitude).

As the orange channel crosses from sequence B to sequence C′ in the right hand panels of Fig. 5.4, we see that the fundamental mode, represented by the longest period green strip, increases in period from that of sequence C′ to that of sequence C.

This green strip terminates at the right hand edge of sequence C due to the fact that very large amplitude Mira-like pulsation occurs there and the star disappears from optical detection due to mass loss and the formation of a dense obscuring circumstellar shell. At this time, the primary mode (orange strip) lies at the long period edge of

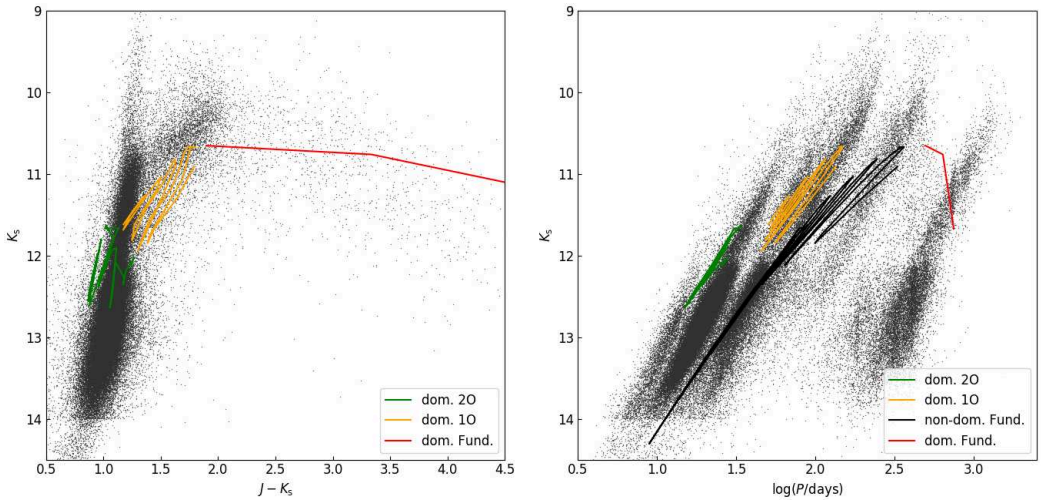

Figure 5.5: Stellar isochrones overplotted to the CMD and PLD of long-periods variables in the Large Magellanic Cloud. Different colors correspond to regimes where different modes are dominant: the 2O mode (green), the 1O mode (orange) and the fundamental mode (Fund., red). The black line in the PLD represents periods of the theoretical fundamental mode where it is not predicted to be dominant (based on growth rates). Isochrones correspond to initial metallicity $Z_i = 0.00155$ and age 1.26 Gyr.

sequence C′.

Related to this is the fact that where the orange channel (primary periods) crosses sequence C, the secondary periods lie at the long period edge of sequence C′. This suggests an evolutionary sequence during which stars evolve through the regions of sequences B and C′ with the 1O mode as the dominant mode of pulsation and the fundamental mode as a secondary oscillation.

Then at the long period edge of sequence C′, the fundamental mode takes over as the dominant mode and the 1O mode becomes the secondary mode. But very soon, large amplitude Mira-like pulsation occurs so that the 1O mode can no longer be detected and then mass loss occurs and the star disappears from optical detection.

5.3.2 An Evolutionary Picture of Pulsational Stability

Theoretical estimates of the stability of radial pulsation modes in red giant stars support the picture of modal evolution described above. In Fig. 5.6, we show the growth rate of the fundamental, 1O, 2O and 3O radial modes as a function of luminosity in a 1.6 $M_\odot$ star using the code discussed in Wood and Olivier (2014).

At the lowest luminosities shown, all modes are unstable with higher order modes tending to have the highest growth rates and these are presumably the ones that are most likely to be the detected as the primary period of oscillation. This accounts for the prominence of sequences A′, A and B at low luminosities in Fig. 5.4.

As the luminosity increases, the 3O mode becomes stable soon after its frequency exceeds the acoustic cutoff frequency ($\log(L/L_\odot) \approx 3.22$). This means that the primary mode of pulsation will no longer be on sequence A′ but will lie on sequence A which corresponds to the 2O mode which now has the highest growth rate. Similarly, the 2O mode becomes stable as the luminosity increases further ($\log(L/L_\odot) \approx 3.55$) so that

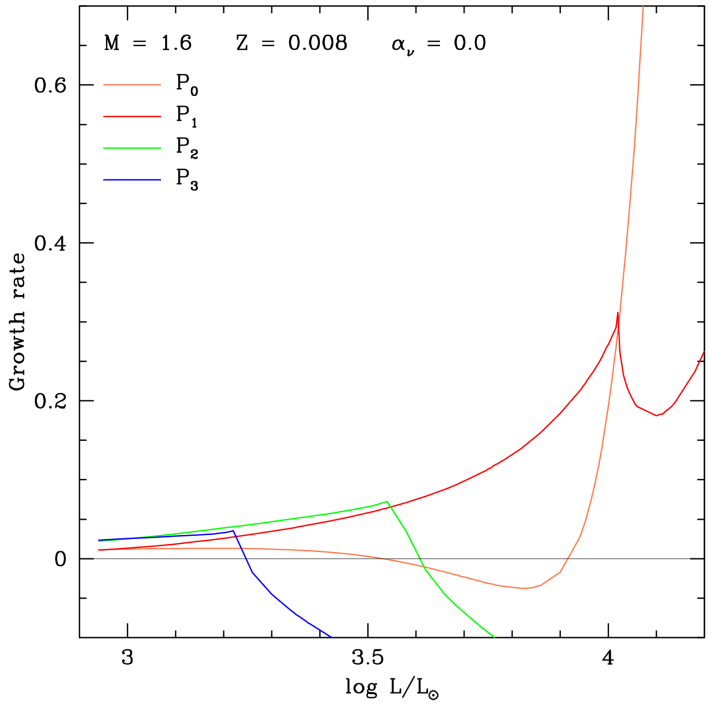

Figure 5.6: The growth rate of the first four radial pulsation modes in a 1.6 $M_\odot$ star as a function of luminosity. The metallicity is LMC-like (Z=0.008) and turbulent viscosity has been neglected. See Wood and Olivier (2014) for details of the modelling.

the primary mode of pulsation now moves to sequence B which corresponds to the 1O mode which now has the highest growth rate.

The evolution of the 1O mode is somewhat different to the evolution of the 2O and 3O modes. With further increase in luminosity, the 1O mode is never stabilised by acoustic energy loss in these calculations.

Note that the fundamental mode has become stable by the time the 1O mode becomes the mode with the highest growth rate. In lower mass models, the fundamental mode may not be completely stable but its growth rate is still much smaller than that of the 1O mode.

At very high luminosities, the fundamental mode becomes extremely unstable. These results suggest the following picture for further evolution of the star.

The star evolves so that the observed primary mode, corresponding to unstable 1O mode, moves through sequences B and C′ while at the same time the observed secondary mode, corresponding to the stable or weakly unstable fundamental mode, moves across the gap between sequences C′ and C. When the star evolves to the luminosity where the fundamental mode becomes unstable, the star becomes a large amplitude Mira-like variable and the 1O mode is no longer seen (defining the long period edge of sequence C′).

This is followed by mass loss and termination of giant branch evolution, thus defining the long period edge of sequence C.

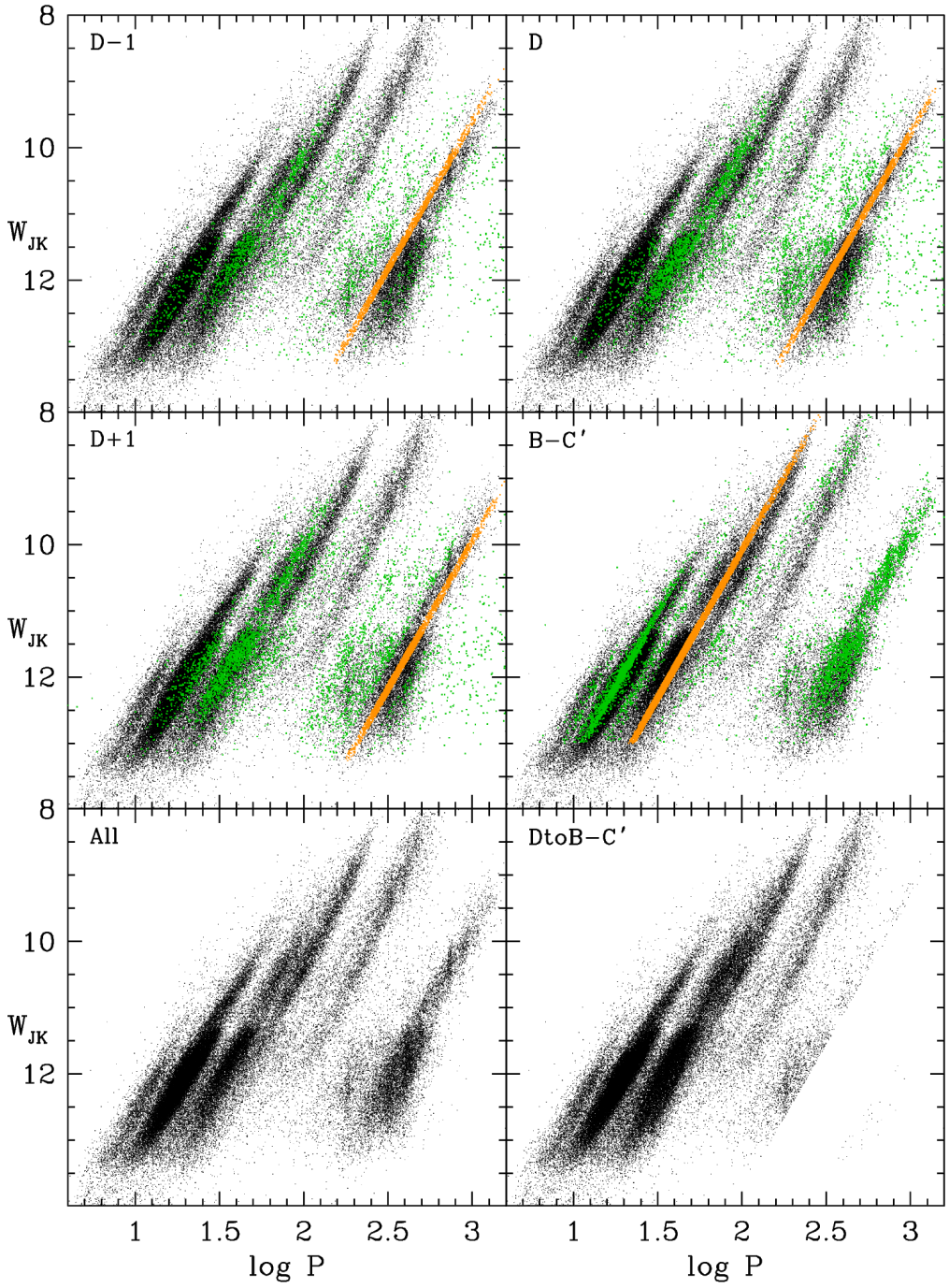

Figure 5.7: Similar to Fig. 5.4. In panels (D-1), (D) and (D+1), the channels are placed in sequence D. In panel (B-C′), the meaning of orange and green points is reversed so that the orange points correspond to secondary or tertiary periods and the green points are the primary periods of the stars marked with orange points. In panel (All), the raw OGLE III data is plotted. In panel (DtoB-C′), the sequence D variables have been shifted to a position lying between sequences B and C′, as described in the text.

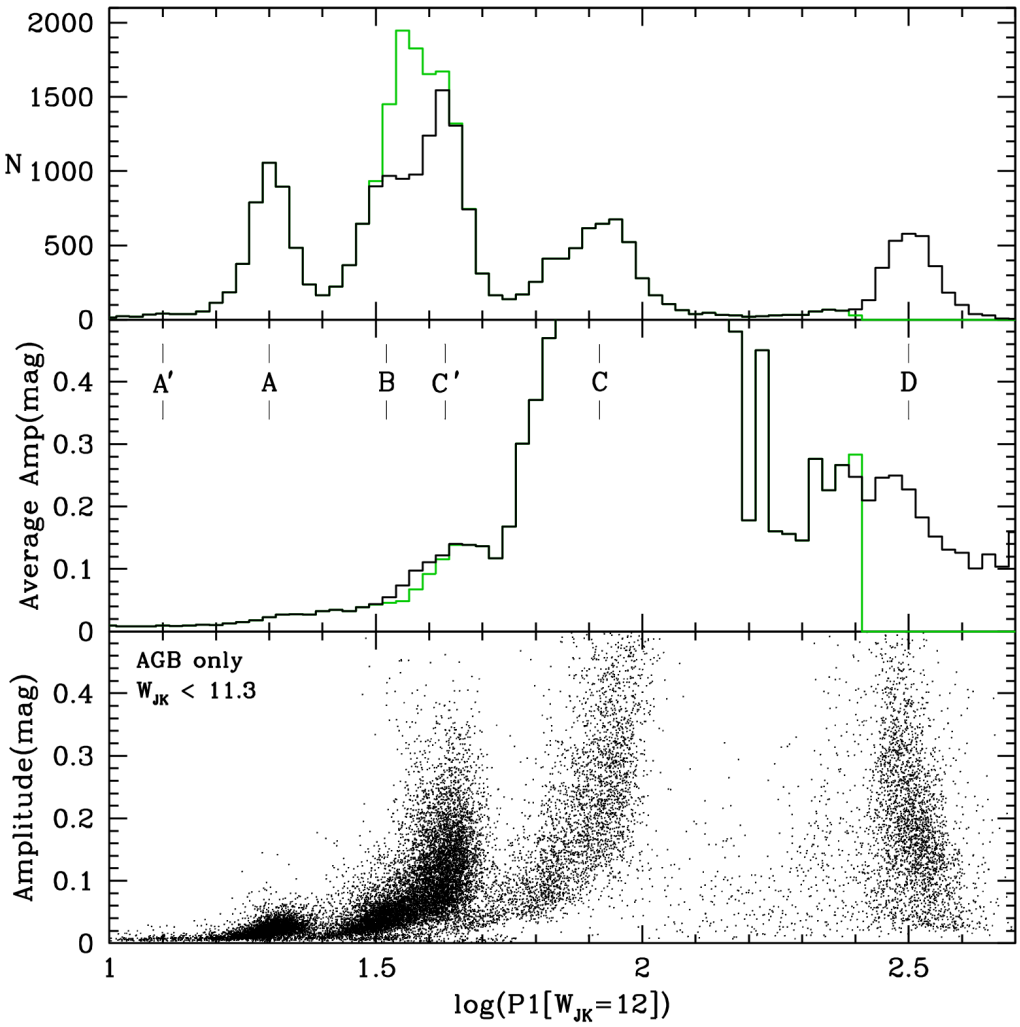

Figure 5.8: Bottom panel: Pulsation amplitude of individual AGB stars in the OGLE III catalogue plotted against $\log(P_{1,W_{\rm JK}=12})$. The selected AGB stars have $W_{\rm JK} < 11.3$. Middle panel: The average amplitude of the AGB stars in bins of width 0.025 in $\log(P_{1,W_{\rm JK}=12})$. Top panel: The numbers of stars in the bins. The positions of the PL sequences are shown in the middle panel. Black lines and points are plotted when the stars have the values of $\log(P_{1,W_{\rm JK}=12})$ in the OGLE III catalogue. The green lines in the top panel are plotted when $\log(P_{1,W_{\rm JK}=12})$ values for all stars in sequence D have been shifted to a new value between sequences B and C′, as described in the text. The green lines in the middle panel are plotted when only the 40% of sequence D stars with a secondary or tertiary period between sequences B and C′ have been shifted.

5.3.3 The Splitting of Sequences B and C′

The problem with the picture presented so far is a lack of explanation for the distinct gap between sequences B and C′ even though both sequences contain 1O pulsators.

The whole region from the short period edge of sequence B to the long period edge of sequence C′ should be populated roughly uniformly in the above picture.

The solution to this problem appears to be provided by the mysterious sequence D variables. In the panels of Fig. 5.7, we show $\log(P)$-$W_{\rm JK}$ plots similar to those in

Fig. 5.4.

In panels (D-1), (D) and (D+1), the orange channel containing the primary mode pulsation lies on the left, middle and right side of sequence D, respectively. Keeping to AGB luminosities where sequences B and C′ are both well defined, we see that the secondary modes of the sequence D variables lie between sequences B and C′ regardless of the position of the orange channel on sequence D.

In panel (B-C′) of Fig. 5.7, we have selected secondary and tertiary periods in a channel between sequences B and C′, and the corresponding primary periods are shown as green points. It is evident that many of these primary modes coincide with sequence D variability.

Therefore, there is clearly a one-to-one correspondence between sequence D variability and stars with oscillation periods lying between sequences B and C′.

The tight correlation of the sequence D period with 1O pulsation period shown by the green and orange strips in Fig. 5.7 strongly suggests that sequence D is associated with some sort of stellar pulsation (e.g. Wood et al. 2004; Saio et al. 2015) and is not caused by a phenomenon such as binarity (e.g. (Wood et al., 2004); (Soszyński, 2007)).

How the sequence D oscillations are related to 1O pulsation is not clear. However, it does seem that sequence D variability is the sole cause of the gap between sequences B and C′.

Stars that would, in the absence of sequence D variability, be positioned in the gap between sequences B and C′, are now positioned in sequence D. In the following, we will show that by transferring all the sequence D stars into the gap between sequences B and C′, the gap disappears.

To begin this process, we identify all stars having a primary period on sequence D and a secondary or tertiary period lying in a strip of width 0.12 in $\log(P)$ located between sequences B and C′.

These stars (40% of all stars on sequence D) are then shifted from the position of their primary period on sequence D to the position of their secondary or tertiary period between sequences B and C′.

The remaining stars in the sequence D region (60% of the original sequence D population) are also shifted into the strip between sequences B and C′ with an offset in $\log(P)$ from the centre of the strip equal to half the offset of the sequence D period from the centre of sequence D.

Now all the original sequence D stars lie in between sequences B and C′. The PL sequences after this shift has been completed are shown in panel (DtoB-C′) of Fig. 5.7. These can be compared to the original PL sequences shown in panel (All) of Fig. 5.7.

It is clear that after the shifting procedure, the gap between sequences B and C′ essentially disappears in the PL diagram.

This can be seen more clearly by looking at the cumulative numbers of stars in narrow strips parallel to the sequences. In Fig. 5.8, the numbers of AGB stars (defined as those with $W_{\rm JK} < 11.3$) in narrow strips of width 0.025 in $\log(P)$ are plotted against $\log(P_{W_{\rm JK}=12})$. Before the sequence D stars are moved, there is a dip in the number of stars in the strips lying between sequences B and C′ (see the black lines in the top panel of Fig. 5.8).

Furthermore, the pulsation amplitude of stars in this region increases smoothly with P (middle panel of Fig. 5.8) suggesting that a single pulsation mode is involved.

After moving the sequence D stars, the whole region on and between sequences B and C′ is populated as if it is a single sequence (green lines in the top panel), once

again suggesting that a single mode is involved. Interestingly, the average amplitude of stars between sequences B and C′ is reduced by adding in the 40% of sequence D stars that have a secondary or tertiary period there.

We conclude that the gap between sequences B and C′ is actually a selection effect: the stars in this gap develop a sequence D oscillation that is of larger amplitude than the sequence B-C′ oscillation and hence, in plots using the observed primary period of variability, these stars appear on sequence D rather than between sequences B and C′.

We do not know why the sequence D oscillation occurs. It could be due to a resonance between 1O mode pulsation and the oscillation associated with sequence D which drains energy from the 1O mode to the LSP oscillation of sequence D, but it could equally be a totally independent mode that just happens to have a large amplitude at this stage of evolution.

5.4 A New Interpretation of the PL sequences of LPVs

We have modelled a synthetic stellar population representative of red giant stars currently in the LMC, and we have assigned to each star a dominant period based on the growth rate of radial pulsation modes.

We find good agreement between the theoretical PL sequences formed by the third and second overtone modes when they are dominant and the observed sequences A′ and A, respectively. However, the theoretical first overtone sequence spreads across both observed sequences B and C′, suggesting that these two sequences may in fact coincide with the same radial pulsation mode.

The theoretical fundamental mode sequence obtained with this modelling agrees with sequence C at RGB luminosities but at AGB luminosities it has periods that are longer than those of sequence C which contains the large amplitude Mira variables and which almost certainly does correspond to radial fundamental mode pulsation (Wood, 2015).

The analysis of observed amplitudes reveals the presence of four distinct period-luminosity-amplitude relations, that we identify with the four lowest radial orders of pulsation. The amplitude distributions compare well with the distributions of theoretical growth rates of overtone modes, validating the use of the latter as proxies for amplitudes.

However, as with the PL sequences, the fundamental mode amplitude distribution shows a poor agreement with observations, especially at bright magnitudes.

If we examine where the theoretical fundamental periods fall regardless of growth rates, we find that they cover the region from the lower part of sequence B to the entire sequence C. This is exactly the region covered by observed stars having modes associated with the observed PAL relation that we identify as fundamental mode pulsation.

This suggests that while the the growth rates of the fundamental mode in the models may be unreliable and underestimated at high luminosities, the periods are generally correct.

Using an empirical examination of observations of multimode LPVs in the LMC, we have found the following. Sequence C consists of radial fundamental mode pulsators which are approaching the end of their AGB evolution, so that the fundamental mode has become unstable.

Sequences B and C′ consist of first overtone mode radial pulsators, with some fundamental mode pulsators on the lower luminosity end of both sequences. These funda-

mental mode pulsators are more massive than the first overtone mode pulsators on the same sequence at the same luminosity.

The gap between sequences B and C′ is caused by the development of a large amplitude oscillation associated with sequence D although the nature of this oscillation is unknown.

Sequence A consists of second overtone mode radial pulsators and sequence A′ consists of third overtone mode radial pulsators. Some nonradial modes with angular degree $\ell = 1$ and $\ell = 2$ have also been detected on sequences A and B, and possibly A′.

Our two approaches produce quite consistent results regarding the assignment of modes to the observed PL sequences. However, since the pulsation-population synthesis models do not include the mysterious sequence D variability, they are not able to split the first overtone pulsation sequence into the two observed sequences.

Allowing both sequence B and sequence C′ to correspond to first overtone pulsation means that the studies of Mosser et al. (2013) and Wood (2015) can be brought into alignment: Mosser et al. (2013) can now assign the fundamental mode to sequence C while Wood (2015) can now move the mode assigned to sequences A′, A and B down by one radial order to give the same mode assignment as Mosser et al. (2013). The major remaining problem with the study of LPVs is the lack of an understanding of sequence D variability.

Chapter 6

Conclusions and Future Perspectives

We presented a new grid of linear, non-adiabatic pulsation models, including periods and growth rates for five radial modes, from the fundamental to the fourth overtone.

The grid represents a significant improvement, and long-awaited update, with respect to previously published pulsation models.

It covers a wide range of the space of stellar parameters in terms of luminosity, effective temperature, total mass and core mass, and chemical composition, thus being able to account for the variety of properties of TP-AGB stars.

The grid includes the first set of C-rich pulsation models to be made publicly available for the community. This important result has been achieved by including carbon variations, with respect to the reference metal mixture, for each metallicity of the grid, and by computing opacity data consistently with the chemical mixture of each model.

We developed tools to combine the grid of models with a stellar population synthesis tool, in order to simulate the pulsation properties of a population of luminous red giant variables.

We applied this procedure to a synthetic stellar population representative of the long-period variables in the LMC.

Models passed the test of a comparison with observations: theoretical periods are in good agreement with observations for all pulsation modes, although fundamental mode periods tend to be overestimated () Moreover, the growth rates predicted for overtone modes are entirely compatible with observed amplitudes.

The approach based on the combination of pulsation models and population synthesis allowed us to obtain a global picture of the observed period-luminosity sequences of LPVs in the LMC, and to provide an unambiguous identification of the pulsation modes responsible for different sequences.

We performed an empirical analysis of the observational data, entirely supporting our theoretical results.

The new interpretation we presented is able to solve the disagreement between previous interpretations, and to shed some light on the open issue of long secondary periods in luminous red giant variables.

Models are going to be made public in a forthcoming work (Trabucchi et al., in prep.) together with a detailed analysis of their relevant properties.

We aim to apply the same method used to study the LMC to globular clusters and resolved stellar populations in other galaxies. This will provide additional constraints

for the goal of the STARKEY project, *i.e.*, to reach a solid calibration of the TP-AGB evolutionary phase.

Moreover, periods and growth rates from pulsation models will be implemented in a flexible way into isochrones and evolutionary tracks that will also be made available to the community.

Some issues remain unsolved, and will be part of future studies.

To begin with, the subject of a proper modelling of the excitation of the fundamental mode has to be addressed.

In fact, based on a comparison with observations, the excitation rates predicted by models for the fundamental mode appears to be underestimated, although periods are generally correct, and reproduce the global trend of observations.

Another major task to be addressed in the future is the expansion of the grid of pulsation models to include a wider range of metallicities as well as variations of oxygen and possibly other elements.

Finally, a systematic investigation is required to determine the conditions under which linear periods provide an appropriate description of variability in real stars. In fact, linear models are known to have the tendency to underestimate the periods of the largest-amplitude variables. This task should thus involve the computation of non-linear models, parallel to those in the grid here presented, in order to provide non-linear corrections to the periods as a function of global stellar parameters.

Appendices

Appendix A

Interpolation in the Grid of Pulsation Models

A.1 The Interpolation Scheme

The main difficulty in designing an appropriate interpolation scheme for the grid of pulsation models comes from the fact that the grid is not rectangular. In other words, the number of nodes, their values and the boundaries of a given parameter of the grid are not always the same, but depend on the combination of the other parameters.

A simple example is the core mass. We constructed the grid so that, for each combination of the other parameters, two different values are available for the core mass. Those two values represent the approximate upper and lower limits to core mass at a given luminosity, for the TP-AGB phase. Therefore, the values of the core mass nodes depend on the input luminosity.

Another critical quantity is the effective temperature. It is an output parameter (the actual input being the mixing length parameter), therefore its value is not known a priori for a combination of the other parameters.

The chemical composition requires special care. In terms of input parameters to the interpolation tool, it is defined by metallicity (Z), hydrogen mass fraction (X) and carbon-to-oxygen ratio (C/O).

However, the actual chemical parameters defining the grid (see section 4.8 and table 4.4) are the reference metallicity ($Z_{\rm ref}$) hydrogen mass fraction, and the C/O variation factor:

$$f_{\rm C/O} = \log\left[\frac{C}{O}\right] - \log\left[\left(\frac{C}{O}\right)_{\odot}\right] . \tag{A.1}$$

To retrieve models to be used for the interpolation, it is required to know the corresponding values of $Z_{\rm ref}$, X, and $f_{\rm C/O}$.

To do so, $f_{\rm C/O}$ is recovered from C/O using Eq. A.1. while reference metallicity is recovered using the expression

$$Z_{\rm ref} = \frac{Z}{1 - (X_{\rm C}/Z)_{\odot}\left[({\rm C/O})\,/\,({\rm C/O})_{\odot} - 1\right]} , \tag{A.2}$$

derived from Eq. 4.49 under the assumption that C/O varies only as a consequence of changes in the abundance of carbon, while the oxygen abundance is scaled-solar. The

following values are used to describe the scaled-solar metal mixture:

$$(\mathrm{C/O})_{\odot} = 0.54954\,, \tag{A.3}$$

$$(X_{\mathrm{C}}/Z)_{\odot} = 0.1819942\,, \tag{A.4}$$

as from Caffau et al. (2011).

The interpolation procedure can be summarised as follows. The user calls the interpolation tool from command line, and specifies as arguments the name of the input file and the positions of the columns corresponding to the input parameters.

The main loop of the interpolation procedure corresponds to reading the input file line by line. Each row is parsed to find the relevant global stellar parameter according to the column indices provided by the user, and derived quantities (Z_{ref}, $f_{\mathrm{C/O}}$) are computed.

For each stellar quantity corresponding to a grid parameter, the grid has to be scanned for suitable interpolation nodes, *i.e.*, having values that bracket the input one.

This is straightforward for Z_{ref}, X, $f_{\mathrm{C/O}}$ and M, as those parameters have fixed and regular nodes, but not for the effective temperature.

For each combination of other parameters, there are exactly two choices of core mass, both of which are necessary to interpolate. It is thus unnecessary to scan the grid in core mass.

Interpolation nodes of effective temperature are not known a priori, but the choice will ultimately be limited to three values, since models were computed for three different values of the mixing length parameter α_{MLT}.

A this point, the code has identified two nodes for each one of the parameters Z_{ref}, X, $f_{\mathrm{C/O}}$, M, and M_{c}, plus the three α_{MLT} nodes. The possible combinations of those nodes correspond to $2 \times 2 \times 2 \times 2 \times 2 \times 3 = 96$ different files, each one containing a luminosity sequence (see section 4.4.1).

Each file is scanned for two luminosity values bracketing the input one. Then, each other parameter is interpolated linearly in luminosity at the input value.

The resulting parameters are thus linearly interpolated at the required value over (in this order) core mass, total mass, hydrogen mass fraction, C/O, metallicity.

At this point, three datasets remain corresponding to stellar parameters and pulsation parameters for three different values of α_{MLT}, *i.e.*, of effective temperatures, now known.

The two sets with effective temperature bracketing the input ones are used to interpolate in T_{eff}.

Whenever the input value is larger (smaller) than any interpolation node, the two largest (smallest) interpolation nodes are used to extrapolate.

The new data is formatted and appended to the original line of the input file, and written onto an output file which name is the same as the input one, but to which the string "`_interpolated`" is appended.

A.2 Remarks on the Application to non-TP-AGB Models

In principle, the grid of pulsation models presented here is only appropriate for the TP-AGB evolutionary phase. Indeed, it relies on the key assumption that the core region can be neglected when modelling pulsation dynamics.

Such an assumption is not necessarily appropriate to other evolutionary phases, namely for the RGB and E-AGB phases.

During E-AGB evolution the core is not yet as fully decoupled from the envelope as is during TP-AGB, thus, in principle, it should be taken into account when computing pulsation models for this evolutionary phase. However, Montalbán et al. (2017) have shown that such an assumption likely holds for E-AGB as well by checking its validity on dipole modes in $1.5\,M_\odot$ AGB models.

It is well known, on the other hand, that during RGB evolution the stellar core does interact with the envelope, as gravity modes that propagate in the innermost region may couple with pressure modes propagating in the envelope. The resulting mixed modes have intrinsically different properties than pure p-modes, that require appropriate modelling. RGB stars have an oscillatory behaviour quite different than AGB stars, as they exhibit solar-like oscillations with complex spectra characterised by many, closely spaced, small amplitude modes, both radial and non-radial.

However, luminous RGB stars have oscillation properties more similar to those of long-period variables on the AGB, thus it may be reasonable to use the models presented here to infer pulsation properties of bright enough RGB models.

Our analysis shows that the dependence of pulsation parameters ($P_{\rm ad}$, P and GR) upon the core mass is very close to linear, and is also rather weak. This suggest that extrapolating towards values different than those expected for TP-AGB evolution, *i.e.*, to RGB and E-AGB values, should give reliable enough results.

We tested this expectation for RGB models by comparison observed periods of RGB stars in the LMC from the OGLE-3 database (see section 5).

The comparison relies on the OGLE evolutionary classification base on a combination of photometric and variability data (Soszyński et al., 2004).

The comparison gives in general reasonable agreement for the distribution of dominant modes (with the relevant exception of the fundamental mode), suggesting that both periods and growth rates are appropriate enough to describe LPVs on the RGB (the brightest ones, approaching the tip of the RGB). This is at least true when the bulk of the stars is considered, although it should be tested in detail.

As for E-AGB, although periods are probably good, growth rates may be significantly off as they may depend upon a not-fully-decoupled energy source.

Similarly, TP-AGBs experiencing HBB are not appropriately described by our models from a theoretical point of view, and should be tested against observations.

Bibliography

Aerts, C., Christensen-Dalsgaard, J., and Kurtz, D. W. (2010). *Asteroseismology*. Springer: Astron. Astrophys. Libr.

Alcock, C., Allsman, R. A., Axelrod, T. S., Bennett, D. P., Cook, K. H., Park, H. S., Marshall, S. L., Stubbs, C. W., Griest, K., Perlmutter, S., Sutherland, W., Freeman, K. C., Peterson, B. A., Quinn, P. J., and Rodgers, A. W. (1993). The MACHO Project - a Search for the Dark Matter in the Milky-Way. In Soifer, B. T., editor, *Sky Surveys. Protostars to Protogalaxies*, volume 43 of *Astronomical Society of the Pacific Conference Series*, page 291.

Alcock, C., Axelrod, T. S., Bennett, D. P., Cook, K. H., Park, H. S., Griest, K., Perlmutter, S., Stubbs, C. W., Freeman, K. C., and Peterson, B. A. (1992). The search for massive compact halo objects with a (semi) robotic telescope. In Filippenko, A. V., editor, *Robotic Telescopes in the 1990s*, volume 34 of *Astronomical Society of the Pacific Conference Series*, pages 193–202.

Arnett, D., Meakin, C., and Young, P. A. (2010). Convection Theory and Sub-Photospheric Stratification. *ApJ*, 710:1619–1626.

Arnett, W. D. (1969). A Possible Model of Supernovae: Detonation of ^{12}C. *Ap&SS*, 5:180–212.

Baker, N. and Kippenhahn, R. (1965). The Pulsations of Models of Delta Cephei Stars. II. *ApJ*, 142:868.

Balmforth, N. J., Gough, D. O., and Merryfield, W. J. (1990). Pulsations of model Mira variables. In Mennessier, M. O. and Omont, A., editors, *From Miras to Planetary Nebulae: Which Path for Stellar Evolution?*, pages 85–87.

Bányai, E., Kiss, L. L., Bedding, T. R., Bellamy, B., Benkő, J. M., Bódi, A., Callingham, J. R., Compton, D., Csányi, I., Derekas, A., Dorval, J., Huber, D., Shrier, O., Simon, A. E., Stello, D., Szabó, G. M., Szabó, R., and Szatmáry, K. (2013). Variability of M giant stars based on Kepler photometry: general characteristics. *MNRAS*, 436:1576–1587.

Bedding, T. R. and Zijlstra, A. A. (1998). HIPPARCOS Period-Luminosity Relations for Mira and Semiregular variables. *ApJ*, 506:L47–L50.

Bloecker, T. (1995). Stellar evolution of low and intermediate-mass stars. I. Mass loss on the AGB and its consequences for stellar evolution. *A&A*, 297:727.

Böhm-Vitense, E. (1958). Über die Wasserstoffkonvektionszone in Sternen verschiedener Effektivtemperaturen und Leuchtkräfte. Mit 5 Textabbildungen. *ZAp*, 46:108.

Boothroyd, A. I. and Sackmann, I.-J. (1988). Low-Mass Stars. II. The Core Mass–Luminosity Relations for Low-Mass Stars. *ApJ*, 328:641.

Bressan, A., Marigo, P., Girardi, L., Salasnich, B., Dal Cero, C., Rubele, S., and Nanni, A. (2012). PARSEC: stellar tracks and isochrones with the PAdova and TRieste Stellar Evolution Code. *MNRAS*, 427:127–145.

Caffau, E., Ludwig, H.-G., Steffen, M., Freytag, B., and Bonifacio, P. (2011). Solar Chemical Abundances Determined with a CO5BOLD 3D Model Atmosphere. *Sol. Phys.*, 268:255–269.

Canuto, V. (1970). Electrical Conductivity and Conductive Opacity of a Relativistic Electron Gas. *ApJ*, 159:641.

Catchpole, R. M., Robertson, B. S. C., Lloyd-Evans, T. H. H., Feast, M. W., Glass, I. S., and Carter, B. S. (1979). JHKL Infrared Photometry of Mira Variables and of Other Late-Type Stars. *South African Astronomical Observatory Circular*, 1:61.

Catelan, M. and Smith, H. A. (2015). *Pulsating Stars*. Wiley-VCH.

Chaplin, W. J. and Miglio, A. (2013). Asteroseismology of Solar-Type and Red-Giant Stars. *ARA&A*, 51:353–392.

Christensen-Dalsgaard, J., Arentoft, T., Brown, T. M., Gilliland, R. L., Kjeldsen, H., Borucki, W. J., and Koch, D. (2009). The Kepler mission. *Communications in Asteroseismology*, 158:328.

Christensen-Dalsgaard, J., Kjeldsen, H., and Mattei, J. A. (2001). Solar-like Oscillations of Semiregular Variables. *ApJ*, 562:L141–L144.

Clayton, M. L. and Feast, M. W. (1969). Absolute magnitudes of Mira variables from statistical parallaxes. *MNRAS*, 146:411.

Cox, J. P. (1980). *Theory of stellar pulsation*. Princeton University Press.

Cox, J. P. and Giuli, R. T. (1968). *Principles of stellar structure* . Gordon and Breach, New York.

Cristallo, S., Piersanti, L., Straniero, O., Gallino, R., Domínguez, I., Abia, C., Di Rico, G., Quintini, M., and Bisterzo, S. (2011). Evolution, Nucleosynthesis, and Yields of Low-mass Asymptotic Giant Branch Stars at Different Metallicities. II. The FRUITY Database. *ApJS*, 197:17.

Dennis, T. R. (1971). Thermal Stability of the Helium-Burning Shell in Stars of 15 Solar Masses. *ApJ*, 167:311.

Dziembowski, W. A. and Soszyński, I. (2010). Acoustic oscillations in stars near the tip of the red giant branch. *A&A*, 524:A88.

Eggen, O. J. (1975a). Observations of Large-Amplitude Red Variables. *ApJS*, 29:77.

Eggen, O. J. (1975b). The classification of intrinsic variables. V. The large-amplitude variables. *ApJ*, 195:661–678.

Eggen, O. J. (1977). The classification of intrinsic variables. VII - The medium-amplitude red variables. *ApJ*, 213:767–786.

Feast, M., Whitelock, P., and Menzies, J. (2002). Globular clusters and the Mira period-luminosity relation. *MNRAS*, 329:L7–L12.

Feast, M. W. (1984). The period-luminosity relation for Mira variables and the distance of the Large Magellanic Cloud. *MNRAS*, 211:51P–55P.

Feast, M. W. (1986). Variables, the galactic bulge and IRAS. In Israel, F. P., editor, *Light on Dark Matter*, volume 124 of *Astrophysics and Space Science Library*, pages 339–348.

Feast, M. W., Glass, I. S., Whitelock, P. A., and Catchpole, R. M. (1989). A period-luminosity-colour relation for Mira variables. *MNRAS*, 241:375–392.

Fox, M. W. and Wood, P. R. (1982). Theoretical growth rates, periods, and pulsation constants for long-period variables. *ApJ*, 259:198–212.

Gaposchkin, C. P. (1954). *Variable stars and galactic structure.*

Gerasimovic, B. P. (1928). The Absolute Magnitudes of Long Period Variable Stars. *Proceedings of the National Academy of Science*, 14:963–968.

Girardi, L., Groenewegen, M. A. T., Hatziminaoglou, E., and da Costa, L. (2005). Star counts in the Galaxy. Simulating from very deep to very shallow photometric surveys with the TRILEGAL code. *A&A*, 436:895–915.

Glass, I. S., Catchpole, R. M., Feast, M. W., Whitelock, P. A., and Reid, I. N. (1987). The period-luminosity relationship for Mira-like variables in the LMC. In Kwok, S. and Pottasch, S. R., editors, *Late Stages of Stellar Evolution*, volume 132 of *Astrophysics and Space Science Library*, pages 51–54.

Glass, I. S. and Evans, T. L. (1981). A period-luminosity relation for Mira variables in the Large Magellanic Cloud. *Nature*, 291:303.

Glass, I. S. and Feast, M. W. (1982a). Infrared photometry of Mira variables in the Baade windows and the distance to the Galactic Centre. *MNRAS*, 198:199–214.

Glass, I. S. and Feast, M. W. (1982b). Infrared Photometry of Mira Variables in the Large Magellanic Cloud and the Pulsational Properties of Miras. *MNRAS*, 199:245.

Gough, D. O. (1967). Convection in Pulsating Stars: Time-Dependent Mixing-Length Theory in the One-Zone Model. *AJ*, 72:799.

Grevesse, N., Asplund, M., and Sauval, A. J. (2007). The Solar Chemical Composition. *Space Sci. Rev.*, 130:105–114.

Groenewegen, M. A. T. and de Jong, T. (1994). Synthetic AGB evolution. 3: The influence of different mass-loss laws. *A&A*, 283:463–468.

Gyllenberg, W. (1929). Studies on the proper motions of long-period variable stars. *Meddelanden fran Lunds Astronomiska Observatorium Serie II*, 53:3–20.

Gyllenberg, W. (1930). The period-luminosity curve of long-period variables. *Meddelanden fran Lunds Astronomiska Observatorium Serie II*, 54:3–18.

Habing, H. J. and Olofsson, H., editors (2004). *Asymptotic Giant Branch Stars*. Springer: Astron. Astrophys. Libr.

Hansen, C. J., Kawaler, S. D., and Trimble, V. (2004). *Stellar interiors : physical principles, structure, and evolution*. Springer-Verlag.

Herwig, F. (2000). The evolution of AGB stars with convective overshoot. *A&A*, 360:952–968.

Herwig, F. (2005). Evolution of Asymptotic Giant Branch Stars. *ARA&A*, 43:435–479.

Houdek, G. and Dupret, M.-A. (2015). Interaction Between Convection and Pulsation. *Living Reviews in Solar Physics*, 12:8.

Huang, C., Riess, A., Hoffmann, S., Klein, C., Bloom, J., Yuan, W., Jones, D., Macri, L., Whitelock, P., Casertano, S., and Anderson, R. I. (2018). A Near Infrared Period-Luminosity Relation for Miras in NGC 4258. In *American Astronomical Society Meeting Abstracts*, volume 231 of *American Astronomical Society Meeting Abstracts*, page 420.07.

Hubbard, W. B. and Lampe, M. (1969). Thermal Conduction by Electrons in Stellar Matter. *ApJS*, 18:297.

Hughes, S. M. G. and Wood, P. R. (1990). Long-period variables in the Large Magellanic Cloud. II - Infrared photometry, spectral classification, AGB evolution, and spatial distribution. *AJ*, 99:784–816.

Ireland, M. J., Scholz, M., and Wood, P. R. (2008). Dynamical opacity-sampling models of Mira variables - I. Modelling description and analysis of approximations. *MNRAS*, 391:1994–2002.

Ita, Y., Tanabé, T., Matsunaga, N., Nakajima, Y., Nagashima, C., Nagayama, T., Kato, D., Kurita, M., Nagata, T., Sato, S., Tamura, M., Nakaya, H., and Nakada, Y. (2002). Pulsation at the tip of the first giant branch? *MNRAS*, 337:L31–L34.

Ita, Y., Tanabé, T., Matsunaga, N., Nakajima, Y., Nagashima, C., Nagayama, T., Kato, D., Kurita, M., Nagata, T., Sato, S., Tamura, M., Nakaya, H., and Nakada, Y. (2004a). Variable stars in the Magellanic Clouds - II. The data and infrared properties. *MNRAS*, 353:705–712.

Ita, Y., Tanabé, T., Matsunaga, N., Nakajima, Y., Nagashima, C., Nagayama, T., Kato, D., Kurita, M., Nagata, T., Sato, S., Tamura, M., Nakaya, H., and Nakada, Y. (2004b). Variable stars in the Magellanic Clouds: results from OGLE and SIRIUS. *MNRAS*, 347:720–728.

Izzard, R. G., Dray, L. M., Karakas, A. I., Lugaro, M., and Tout, C. A. (2006). Population nucleosynthesis in single and binary stars. I. Model. *A&A*, 460:565–572.

Izzard, R. G., Tout, C. A., Karakas, A. I., and Pols, O. R. (2004). A new synthetic model for asymptotic giant branch stars. *MNRAS*, 350:407–426.

Karakas, A. I., Lattanzio, J. C., and Pols, O. R. (2002). Parameterising the Third Dredge-up in Asymptotic Giant Branch Stars. *PASA*, 19:515–526.

Keller, S. C. and Wood, P. R. (2006). Bump Cepheids in the Magellanic Clouds: Metallicities, the Distances to the LMC and SMC, and the Pulsation-Evolution Mass Discrepancy. *ApJ*, 642:834–841.

Kippenhahn, R., Weigert, A., and Weiss, A. (2012). *Stellar Structure and Evolution*. Springer: Astron. Astrophys. Libr.

Kiss, L. L. and Bedding, T. R. (2003). Red variables in the OGLE-II data base - I. Pulsations and period-luminosity relations below the tip of the red giant branch of the Large Magellanic Cloud. *MNRAS*, 343:L79–L83.

Lebzelter, T., Schultheis, M., and Melchior, A. L. (2002). AGAPEROS: Searching for variable stars in the LMC Bar. II. Temporal and near-IR analysis of Long-Period Variables. *A&A*, 393:573–583.

Lebzelter, T. and Wood, P. R. (2005). Long period variables in 47 Tuc: direct evidence for lost mass. *A&A*, 441:1117–1127.

Lebzelter, T. and Wood, P. R. (2007). The AGB stars of the intermediate-age LMC cluster NGC 1846. Variability and age determination. *A&A*, 475:643–650.

Lebzelter, T. and Wood, P. R. (2011). Long period variables and mass loss in the globular clusters NGC 362 and NGC 2808. *A&A*, 529:A137.

Lebzelter, T. and Wood, P. R. (2016). The long-period variables in ω Centauri. *A&A*, 585:A111.

Macri, L. M., Ngeow, C.-C., Kanbur, S. M., Mahzooni, S., and Smitka, M. T. (2015). Large Magellanic Cloud Near-Infrared Synoptic Survey. I. Cepheid Variables and the Calibration of the Leavitt Law. *AJ*, 149:117.

Marigo, P. (2002). Asymptotic Giant Branch evolution at varying surface C/O ratio: effects of changes in molecular opacities. *A&A*, 387:507–519.

Marigo, P. and Aringer, B. (2009). Low-temperature gas opacity. ÆSOPUS: a versatile and quick computational tool. *A&A*, 508:1539–1569.

Marigo, P., Bressan, A., Nanni, A., Girardi, L., and Pumo, M. L. (2013). Evolution of thermally pulsing asymptotic giant branch stars - I. The COLIBRI code. *MNRAS*, 434:488–526.

Marigo, P. and Girardi, L. (2007). Evolution of asymptotic giant branch stars. I. Updated synthetic TP-AGB models and their basic calibration. *A&A*, 469:239–263.

Marigo, P., Girardi, L., Bressan, A., Groenewegen, M. A. T., Silva, L., and Granato, G. L. (2008). Evolution of asymptotic giant branch stars. II. Optical to far-infrared isochrones with improved TP-AGB models. *A&A*, 482:883–905.

Marigo, P., Girardi, L., Bressan, A., Rosenfield, P., Aringer, B., Chen, Y., Dussin, M., Nanni, A., Pastorelli, G., Rodrigues, T. S., Trabucchi, M., Bladh, S., Dalcanton, J., Groenewegen, M. A. T., Montalbán, J., and Wood, P. R. (2017). A New Generation of PARSEC-COLIBRI Stellar Isochrones Including the TP-AGB Phase. *ApJ*, 835:77.

Matsunaga, N., Menzies, J. W., Feast, M. W., Whitelock, P. A., Onozato, H., Barway, S., and Aydi, E. (2017). Discovery of carbon-rich Miras in the Galactic bulge. *MNRAS*, 469:4949–4956.

Menzies, J. W. and Whitelock, P. A. (1985). A period-luminosity relation for Mira variables in globular clusters and its impact on the distance scale. *MNRAS*, 212:783–797.

Montalbán, J., Trabucchi, M., Marigo, P., Wood, P. R., and Pastorelli, G. (2017). Non-radial modes in AGB stars. In *European Physical Journal Web of Conferences*, volume 152 of *European Physical Journal Web of Conferences*, page 06008.

Mosser, B., Dziembowski, W. A., Belkacem, K., Goupil, M. J., Michel, E., Samadi, R., Soszyński, I., Vrard, M., Elsworth, Y., Hekker, S., and Mathur, S. (2013). Period-luminosity relations in evolved red giants explained by solar-like oscillations. *A&A*, 559:A137.

Munteanu, A., Bono, G., José, J., García-Berro, E., and Stellingwerf, R. F. (2005). Limit-Cycle Behavior in One-Zone Convective Models. *ApJ*, 627:454–463.

Olivier, E. A. and Wood, P. R. (2005). Non-linear pulsation models of red giants. *MNRAS*, 362:1396–1412.

Ostlie, D. A. and Cox, A. N. (1986). A linear survey of the Mira variable star instability region of the Hertzsprung-Russell diagram. *ApJ*, 311:864–872.

Paczyński, B. (1970). Evolution of Single Stars. I. Stellar Evolution from Main Sequence to White Dwarf or Carbon Ignition. *Acta Astron.*, 20:47.

Pagel, B. E. J. and Tautvaišienė, G. (1999). Chemical Evolution of the Magellanic Clouds. *Ap&SS*, 265:461–468.

Pettit, E. and Nicholson, S. B. (1933). Measurements of the Radiation from Variable Stars. *ApJ*, 78:320.

Planck Collaboration, Ade, P. A. R., Aghanim, N., Arnaud, M., Ashdown, M., Aumont, J., Baccigalupi, C., Banday, A. J., Barreiro, R. B., Bartlett, J. G., and et al. (2016). Planck 2015 results. XIII. Cosmological parameters. *A&A*, 594:A13.

Reid, M. J. and Goldston, J. E. (2002). How Mira Variables Change Visual Light by a Thousandfold. *ApJ*, 568:931–938.

Riebel, D., Boyer, M. L., Srinivasan, S., Whitelock, P., Meixner, M., Babler, B., Feast, M., Groenewegen, M. A. T., Ita, Y., Meade, M., Shiao, B., and Whitney, B. (2015). SAGE-Var: An Infrared Survey of Variability in the Magellanic Clouds. *ApJ*, 807:1.

Riess, A. G., Macri, L. M., Hoffmann, S. L., Scolnic, D., Casertano, S., Filippenko, A. V., Tucker, B. E., Reid, M. J., Jones, D. O., Silverman, J. M., Chornock, R., Challis, P., Yuan, W., Brown, P. J., and Foley, R. J. (2016). A 2.4% Determination of the Local Value of the Hubble Constant. *ApJ*, 826:56.

Robertson, B. S. C. and Feast, M. W. (1981). The bolometric, infrared and visual absolute magnitudes of Mira variables. *MNRAS*, 196:111–120.

Saio, H., Baker, N. H., and Gautschy, A. (1998). On the properties of strange modes. *MNRAS*, 294:622.

Saio, H., Wood, P. R., Takayama, M., and Ita, Y. (2015). Oscillatory convective modes in red giants: a possible explanation of the long secondary periods. *MNRAS*, 452:3863–3868.

Samus', N. N., Kazarovets, E. V., Durlevich, O. V., Kireeva, N. N., and Pastukhova, E. N. (2017). General catalogue of variable stars: Version GCVS 5.1. *Astronomy Reports*, 61:80–88.

Schöier, F. L. and Olofsson, H. (2001). Models of circumstellar molecular radio line emission. Mass loss rates for a sample of bright carbon stars. *A&A*, 368:969–993.

Seaton, M. J. (2005). Opacity Project data on CD for mean opacities and radiative accelerations. *MNRAS*, 362:L1–L3.

Skrutskie, M. F., Cutri, R. M., Stiening, R., Weinberg, M. D., Schneider, S., Carpenter, J. M., Beichman, C., Capps, R., Chester, T., Elias, J., Huchra, J., Liebert, J., Lonsdale, C., Monet, D. G., Price, S., Seitzer, P., Jarrett, T., Kirkpatrick, J. D., Gizis, J. E., Howard, E., Evans, T., Fowler, J., Fullmer, L., Hurt, R., Light, R., Kopan, E. L., Marsh, K. A., McCallon, H. L., Tam, R., Van Dyk, S., and Wheelock, S. (2006). The Two Micron All Sky Survey (2MASS). *AJ*, 131:1163–1183.

Smak, J. (1964). Photometry and Spectrophotometry of Long-Period Variables. *ApJS*, 9:141.

Soszyński, I. (2007). Long Secondary Periods and Binarity in Red Giant Stars. *ApJ*, 660:1486–1491.

Soszyński, I., Dziembowski, W. A., Udalski, A., Kubiak, M., Szymański, M. K., Pietrzyński, G., Wyrzykowski, L., Szewczyk, O., and Ulaczyk, K. (2007). The Optical Gravitational Lensing Experiment. Period–Luminosity Relations of Variable Red Giant Stars. *Acta Astron.*, 57:201–225.

Soszyński, I., Udalski, A., Kubiak, M., Szymański, M., Pietrzyński, G., Zebruń, K., Szewczyk, O., and Wyrzykowski, L. (2004). The Optical Gravitational Lensing Experiment. Small Amplitude Variable Red Giants in the Magellanic Clouds. *Acta Astron.*, 54:129–152.

Soszynski, I., Udalski, A., Kubiak, M., Szymanski, M. K., Pietrzynski, G., Zebrun, K., Szewczyk, O., Wyrzykowski, L., and Ulaczyk, K. (2005). The Optical Gravitational Lensing Experiment. Miras and Semiregular Variables in the Large Magellanic Cloud. *Acta Astron.*, 55:331–348.

Soszyński, I., Udalski, A., Szymański, M. K., Kubiak, M., Pietrzyński, G., Wyrzykowski, Ł., Szewczyk, O., Ulaczyk, K., and Poleski, R. (2009). The Optical Gravitational Lensing Experiment. The OGLE-III Catalog of Variable Stars. IV. Long-Period Variables in the Large Magellanic Cloud. *Acta Astron.*, 59:239–253.

Soszyński, I. and Wood, P. R. (2013). Semiregular Variables with Periods Lying between the Period-Luminosity Sequences C', C, and D. *ApJ*, 763:103.

Stancliffe, R. J., Izzard, R. G., and Tout, C. A. (2005). Third dredge-up in low-mass stars: solving the Large Magellanic Cloud carbon star mystery. *MNRAS*, 356:L1–L5.

Stancliffe, R. J., Tout, C. A., and Pols, O. R. (2004). Deep dredge-up in intermediate-mass thermally pulsing asymptotic giant branch stars. *MNRAS*, 352:984–992.

Stellingwerf, R. F. (1975). Modal stability of RR Lyrae stars. *ApJ*, 195:441–466.

Stello, D., Compton, D. L., Bedding, T. R., Christensen-Dalsgaard, J., Kiss, L. L., Kjeldsen, H., Bellamy, B., García, R. A., and Mathur, S. (2014). Non-radial Oscillations in M-giant Semi-regular Variables: Stellar Models and Kepler Observations. *ApJ*, 788:L10.

Straniero, O., Chieffi, A., Limongi, M., Busso, M., Gallino, R., and Arlandini, C. (1997). Evolution and Nucleosynthesis in Low-Mass Asymptotic Giant Branch Stars. I. Formation of Population I Carbon Stars. *ApJ*, 478:332–339.

Straniero, O., Gallino, R., and Cristallo, S. (2006). s process in low-mass asymptotic giant branch stars. *Nuclear Physics A*, 777:311–339.

Takayama, M., Saio, H., and Ita, Y. (2013). On the pulsation modes of OGLE small amplitude red giant variables in the LMC. *MNRAS*, 431:3189–3195.

Trabucchi, M., Wood, P. R., Montalbán, J., Marigo, P., Pastorelli, G., and Girardi, L. (2017). A New Interpretation of the Period-Luminosity Sequences of Long-period Variables. *ApJ*, 847:139.

Tuthill, P. G., Haniff, C. A., Baldwin, J. E., and Feast, M. W. (1994). No Fundamental-Mode Pulsation in R-Leonis. *MNRAS*, 266:745.

Udalski, A., Szymański, M., Kaluzny, J., Kubiak, M., and Mateo, M. (1992). The Optical Gravitational Lensing Experiment. *Acta Astron.*, 42:253–284.

Udalski, A., Szymański, M. K., Soszyński, I., and Poleski, R. (2008). The Optical Gravitational Lensing Experiment. Final Reductions of the OGLE-III Data. *Acta Astron.*, 58:69–87.

Vassiliadis, E. and Wood, P. R. (1993). Evolution of low- and intermediate-mass stars to the end of the asymptotic giant branch with mass loss. *ApJ*, 413:641–657.

Wagenhuber, J. and Groenewegen, M. A. T. (1998). New input data for synthetic AGB evolution. *A&A*, 340:183–195.

Weiss, A. and Ferguson, J. W. (2009). New asymptotic giant branch models for a range of metallicities. *A&A*, 508:1343–1358.

Whitelock, P. A. (2013). Asymptotic giant branch variables as extragalactic distance indicators. In de Grijs, R., editor, *Advancing the Physics of Cosmic Distances*, volume 289 of *IAU Symposium*, pages 209–216.

Whitelock, P. A. and Feast, M. W. (2014). Gaia, Variable Stars and the Distance Scale. In *EAS Publications Series*, volume 67 of *EAS Publications Series*, pages 263–269.

Whitelock, P. A., Feast, M. W., van Loon, J. T., and Zijlstra, A. A. (2003). Obscured asymptotic giant branch variables in the Large Magellanic Cloud and the period-luminosity relation. *MNRAS*, 342:86–104.

Wilson, R. E. and Merrill, P. W. (1942). Mean Absolute Magnitudes and Space Motions of the Long-Period Variable Stars. *ApJ*, 95:248.

Winters, J. M., Le Bertre, T., Jeong, K. S., Nyman, L.-Å., and Epchtein, N. (2003). Mass-loss from dusty, low outflow-velocity AGB stars. I. Wind structure and mass-loss rates. *A&A*, 409:715–735.

Wood, P. and Arnett, D. (2011). Testing a Modified Mixing-Length Theory: Comparison to the Pulsation of AGB Stars. In Kerschbaum, F., Lebzelter, T., and Wing, R. F., editors, *Why Galaxies Care about AGB Stars II: Shining Examples and Common Inhabitants*, volume 445 of *Astronomical Society of the Pacific Conference Series*, page 183.

Wood, P. R. (2000). Variable Red Giants in the LMC: Pulsating Stars and Binaries? *PASA*, 17:18–21.

Wood, P. R. (2015). The pulsation modes, masses and evolution of luminous red giants. *MNRAS*, 448:3829–3843.

Wood, P. R., Alcock, C., Allsman, R. A., Alves, D., Axelrod, T. S., Becker, A. C., Bennett, D. P., Cook, K. H., Drake, A. J., Freeman, K. C., Griest, K., King, L. J., Lehner, M. J., Marshall, S. L., Minniti, D., Peterson, B. A., Pratt, M. R., Quinn, P. J., Stubbs, C. W., Sutherland, W., Tomaney, A., Vandehei, T., and Welch, D. L. (1999). MACHO observations of LMC red giants: Mira and semi-regular pulsators, and contact and semi-detached binaries. In Le Bertre, T., Lebre, A., and Waelkens, C., editors, *Asymptotic Giant Branch Stars*, volume 191 of *IAU Symposium*, page 151.

Wood, P. R., Bessell, M. S., and Fox, M. W. (1983a). Long-period variables in the Magellanic Clouds - Supergiants, AGB stars, supernova precursors, planetary nebula precursors, and enrichment of the interstellar medium. *ApJ*, 272:99–115.

Wood, P. R., Bessell, M. S., and Fox, M. W. (1983b). Long-period variables in the Magellanic Clouds - Supergiants, AGB stars, supernova precursors, planetary nebula precursors, and enrichment of the interstellar medium. *ApJ*, 272:99–115.

Wood, P. R. and Olivier, E. A. (2014). Strange pulsation modes in luminous red giants. *MNRAS*, 440:2576–2580.

Wood, P. R., Olivier, E. A., and Kawaler, S. D. (2004). Long Secondary Periods in Pulsating Asymptotic Giant Branch Stars: An Investigation of their Origin. *ApJ*, 604:800–816.

Wood, P. R. and Sebo, K. M. (1996). On the pulsation mode of Mira variables: evidence from the Large Magellanic Cloud. *MNRAS*, 282:958–964.

Wood, P. R. and Zarro, D. M. (1981). Helium-shell flashing in low-mass stars and period changes in mira variables. *ApJ*, 247:247–256.

Wray, J. J., Eyer, L., and Paczyński, B. (2004). OGLE small-amplitude variables in the Galactic bar. *MNRAS*, 349:1059–1068.

Xiong, D. R., Deng, L., and Cheng, Q. L. (1998). Turbulent Convection and Pulsational Stability of Variable Stars. I. Oscillations of Long-Period Variables. *ApJ*, 499:355–366.

Xiong, D.-R. and Deng, L.-C. (2013). Solar-like and Mira-like oscillations of stars – A uniform excitation mechanism. *Research in Astronomy and Astrophysics*, 13:1269–1294.

Yuan, W., Macri, L. M., He, S., Huang, J. Z., Kanbur, S. M., and Ngeow, C.-C. (2017). Large Magellanic Cloud Near-infrared Synoptic Survey. V. Period-Luminosity Relations of Miras. *AJ*, 154:149.